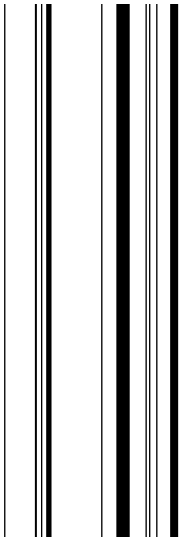

universiteit hasselt

2014 | Faculty of Sciences

DOCTORAL DISSERTATION

Synthesis and characterization of multifunctional tin based compounds

Doctoral dissertation is submitted to obtain the degrees of
- Doctor of Science: Chemistry at Hasselt University
- Doctor of Science at Vilnius University

Andrius Stanulis

Promoters: Prof. Dr Marlies Van Bael | Hasselt University
Prof. Habil. Dr Aivaras Kareiva | Vilnius University
Copromoters: Prof. Dr An Hardy | Hasselt University
Prof. Aldona Beganskiene | Vilnius University

D/2014/2451/26

The dissertation was carried out in Hasselt University and Vilnius University in the period 2008-2012.

Promoters:

Prof. Dr. Marlies Van Bael

(Hasselt University, Physical Sciences, Chemistry 03P)

Prof. Dr. An Hardy

(Hasselt University, Physical Sciences, Chemistry 03P)

Prof. Habil. Dr. Aivaras Kareiva

(Vilnius University, Physical Sciences, Chemistry 03P)

Contents

Abbreviations

AFM	Atomic Force Microscopy
ALD	Atomic Layer Deposition
BLM	Brick Layer Model
CA	Citric Acid
CIE	Commission Internationale de l'Eclairage
CN	Coordination Number
CT	Charge Transfer
DFT	Density Functional Theory
DSSC	Dye-Sensitized Solar Cell
DTG	Differential Thermogravimetry
ED	Electric Dipole
EDTA	Ethylenediaminetetraacetic Acid
EN	Electronegativity
EQ	Electric Quadrupole
FED	Field Emission Display
FTIR	Fourier Transform Infrared Spectroscopy
G-C	Gel to Crystallite Conversion
HL	Host Lattice
HT-XRD	High Temperature X-ray Diffraction
ICP-AES	Inductively Coupled Plasma Atomic Emission Spectroscopy
IS	Impedance Spectroscopy
LE	Luminous Efficacy

LED	Light Emitting Diode
LLP	Long Lasting Phosphorescence
MD	Magnetic Dipole
n-GCM	Nano-grain Composite Model
NIR	Near Infrared
PDP	Plasma Display Panel
PL	Photoluminescence
RMS	Root Mean Square
SEM	Scanning Electron Microscopy
SOFC	Solid Oxide Fuel Cell
SSR	Solid State Reaction
STE	Self Trapped Exciton
TCO	Transparent Conducting Oxide
TG-DSC	Thermogravimetry and Differential Scanning Calorimetry
TQ	Thermal Quenching
UV/VIS	Ultraviolet/Visible
XRD	X-ray Diffraction

Chapter 1. Introduction

Tin dioxide is an oxygen deficient n-type semiconducting material with a wide band gap of 3.6 eV. Doped and undoped SnO_2 films have been extensively investigated for many applications, such as transparent conducting oxide (TCO), oxidation catalyst, and solid state gas sensing material [1-4]. Tin dioxide belongs to the family of oxide materials that combine a low electrical resistance with a high optical transparency in the visible range of the electromagnetic spectrum. These properties are sought in a number of applications; notably as electrode materials in solar cells, light emitting diodes, flat panel displays, and other optoelectronic devices. The key for understanding many aspects of SnO_2 surface properties is the dual valency number of Sn. This dual valency facilitates a reversible transformation of the surface composition from stoichiometric surfaces with Sn^{4+} surface cations into a reduced surface with Sn^{2+} surface cations depending on the oxygen chemical potential of the system [5].

Under normal conditions in air a layer of the adsorbed oxygen molecules is formed at the surface of tin dioxide. The surface electrons can be transferred to these molecules if the lowest lying unoccupied molecular orbitals of the adsorbate complex lie below the Fermi level (acceptor levels). The transfer of electrons from SnO_2 to oxygen leads to the creation of a depletion layer near the surface of a crystal, the concentration of electrons in which is less than in bulk. The net charge at the surface generates an electrostatic field, which causes a bending of the energy bands in the SnO_2. A negative surface charge bends the bands upward, i.e. pushes the Fermi level into the band gap of the SnO_2, effectively reducing the charge carrier concentration and resulting in an electron depletion zone. In other words, this is an electron trapping process at the surface, which leads to an increase

in the electrical resistance (or decrease in conductivity) of the surface layer. When a reducing gas, e.g. CO (or H_2, H_2S, NH_3 etc.), reacts with the adsorbed oxygen to form CO_2, the concentration of oxygen in layer is decreased. The electrons released in this reaction are injected into the conduction band of the SnO_2, which results in a decrease in the electrical resistance (or increase in conductivity) of materials with n-type conductivity. According to barrier model, reaction of adsorbed oxygen species with reducing gases decreases the potential barrier heights, resulting in a significant decrease in resistance [6].

SnO_2 has also been intensively studied as an anode material for lithium ion batteries due to its large theoretical capacity (782 mAh g^{-1}), which is more than twice the theoretical capacity of currently used graphite (372 mAh g^{-1}) [7].

SnO_2 thin films have been prepared by various techniques, such as chemical vapour deposition [8], r.f. magnetic sputtering [9], spray pyrolysis [10], sol–gel processing [11, 12], and atomic layer deposition (ALD) [13]. Every coating technique has its specific advantages and disadvantages. However, published results generally show that it is difficult to control the particles size in the films, to avoid residual tensions in the crystalline lattice, and that surface properties suffer from interferences of counter-ions such as Cl^- and NO_3^- [14]. The sol–gel process is a convenient method because of its simplicity, homogeneity at the solution stage, high reactivity of starting materials, easy composition control, capability for uniform large-area coatings and low cost [15, 16]. The preparation of SnO_2 thin films via sol-gel directly using $SnCl_2$ or $SnCl_4$ as a starting material has been reported [17-19]. The high amount of remaining chloride anions in the synthesized oxide was reported to have several detrimental effects: they can introduce

random n-type doping in the film, modify sensitivity of sensors, promote agglomeration of particles and lead to higher sintering temperatures. Besides, the solution containing stannous ions needed to be kept in acidic condition (pH ~ 1–2) to avoid $Sn(OH)_2$ formation and precipitation [20, 21]. ALD reactions have potential disadvantages of using halogenated Sn precursors such as corrosive damage to growing films and deposition equipment [13]. Moreover, this type of deposition process is slow and quite expensive.

Perovskite-type alkaline earth metal meta-stannates with the general formula of $MSnO_3$ (M = Ca, Sr and Ba) have received increasing attention due to their wide applications in ceramic dielectric bodies [22, 23], gas sensors [24-26], anode materials for lithium ion batteries [27-31] and photocatalysts [32-38]. Thangadurai *et al*. [39] and Misra *et al.* [40] reported that Fe substituted $SrSnO_3$ compounds exhibit both ionic and electronic conductivity and may be important material to be employed in solid oxide fuel cells (SOFC) application. Photovoltaic performance of $SrSnO_3$ nanoparticles utilized as electrode materials in dye-sensitized solar cells (DSSCs) was demonstrated as well [41].

During the last decade, various methods have been used to prepare stannates, including high-temperature solid state [42, 43], sol-gel [44], hydrothermal [45-47], sol-gel combustion [48, 49], polymeric precursor [50, 51], lyothermal [52], wet chemical [53, 54], chemical precipitation [55, 56] and reverse micelle [57]. All these methods are focused on the synthesis of certain individual compound. Among mentioned above synthesis methods, aqueous sol–gel processing route is most convenient method because of its simplicity, good mixing of starting materials, relatively low reaction temperature and easy control of chemical composition of the end product

[58-60]. Azad *et al*. [44] for preparation of $CaSnO_3$, $SrSnO_3$ and $BaSnO_3$ suggested sol-gel method preferably using metal ethoxides as starting materials. However, it is well known that non-aqueous sol-gel processing is quite expensive synthesis route [61].

The divalent (Sn^{2+}) or tetravalent (Sn^{4+}) tin chloride is another tin source commonly used in the sol-gel processing. According to the literature, at low temperatures it is rather difficult to eliminate chloride ions from the end product. At higher temperatures (>900 ºC) their elimination occurs according to Eq. 1.1 leading to the reduction of tin Eq. 1.2.

$$2Cl^- \rightarrow Cl_2\uparrow + 2e^- \qquad \text{(Eq. 1.1)}$$

$$Sn^{4+} + 2e^- \rightarrow Sn^{2+} \qquad \text{(Eq. 1.2)}$$

The reduction of tin makes the crystallization of perovskite more difficult. Due to this process, tin oxide is observed as a secondary phase in the synthesis product [50].

The development of flat panel displays, such as field emission displays (FEDs), plasma display panels (PDPs) and thin film electro-luminescent devices (TFEL) has always been accompanied by improvements in the used phosphors. Many efforts have been made to discover novel host materials as well as activators with high performance for phosphor applications [62, 63].

From a practical point of view, oxide phosphors are more attractive than the traditional sulfide or halide phosphors due to their resistance to moisture. During last decade, alkaline earth ortho-stannates (M_2SnO_4 where M = Ca, Sr and Ba) have been drawing more and more attention as host matrix for new phosphors because of their stable crystalline structure and high physical and chemical stability [64]. Incorporation of optically active lanthanide ions into the stannate host matrix resulted in phosphors

possessing photoluminescence (PL) [65-67] and long lasting phosphorescence (LLP) [68-70] properties.

LLP phosphors emitting in blue [71] and green [72] spectral region almost meet the requirements for practical applications and are commercially available. However afterglow properties of orange to red LLP phosphors are still far away from the desired target properties (high brightness, high efficiency, saturated color). Therefore, there is still a strong need for the development of novel host materials for LLP phosphor emitting at longer (orange to red) wavelengths [73].

In general, the properties of LLP phosphors can be adjusted by using a host-mixing method to change the original constituents of the lattice or introducing different co-dopants [74]. Therefore, it is necessary to systematically investigate each host material individually to learn more about the mechanisms governing the photoluminescence phenomenon.

The main aim of this work was to synthesize and investigate different multifunctional tin based compounds. The additional aim was better understand the sol-gel processing route to these multifunctional tin based compounds. Moreover, the key motivation of this study was investigation of the nature and properties of the alkaline earth metal stannates doped with Sm^{3+}, Eu^{3+} or Pr^{3+} ions searching of novel suitable inorganic hosts for successful lanthanide incorporation. For this reason there were formulated tasks as follows:

- To elaborate a simple, inexpensive and environmentally benign ‘chimie douce’ synthetic approach based on the gel to crystallite conversion (G-C) method for the preparation of strontium stannate $SrSnO_3$, strontium titanate

$SrTiO_3$, and mixed strontium stannates-titanates $SrSn_{1-x}Ti_xO_3$ (x = 0.05–0.5 mol %).

- To suggest a novel synthetic approach for the preparation of uniform SnO_2 films, derived from highly pure solutions containing no interfering counter-ions in neutral medium using innocuous H_2O as a solvent. To characterize deeply the citrato peroxo Sn(IV) precursor gel as well.
- To propose a novel and versatile synthetic approach for the preparation of alkaline earth metal (Ca, Sr and Ba) stannates via aqueous sol-gel (combustion) method.
- To investigate photoluminescence properties of Sm^{3+}, Eu^{3+} or Pr^{3+} doped earth metal stannate phosphors prepared by high temperature solid-state reaction method.
- To study nanostructured ceramics of $BaSnO_3$ and Ba_2SnO_4 by means of impedance spectroscopy and compare these materials.

Chapter 2. Synthesis routes

2.1. Solid State Reaction (SSR)

Solid state reaction is the most widely used method for the preparation of polycrystalline solids from a mixture of solid starting materials (usually powders). This method provides us with a large range of selection of starting materials such as, oxides, carbonates, oxalates, etc. Solids do not react together at room temperature and it is necessary to heat them to much higher temperatures, often up to 1000 – 1500 °C for the reaction to occur at an appreciable rate [75]. The solid state reaction is diffusion limited process, thus high temperature provides the necessary energy for the reaction to occur. Products yielded from solid state reactions are usually thermodynamically stable compounds. It means that both thermodynamic and kinetic factors are important in solid state reactions.

There are three main factors that influence the rate of reaction between solids [75]:

- The area of contact between the reacting solids;
- The rate of nucleation of the product phase;
- The rates of diffusion of ions through the various phases (especially product phase);

The reaction rate can be improved by using fine powders, since number of interfaces increases with decreasing particle size. Pelletizing the mixture of starting powders will reduce the inter-particle void space and increase reaction rate.

It should be mentioned that despite the simplicity of the solid state reaction route, it has certain disadvantages:

- May give compositionally inhomogeneous products;
- May not get desired microstructure;
- Evaporation of a reactant due to high temperature (e.g. alkali oxides, Tl_2O, PbO, Bi_2O_3, HgO).

2.2. Sol-gel Synthesis Route

Sol-gel process involves the evolution of inorganic networks through the formation of a colloidal suspension (sol) and gelation of the sol to form three-dimensional, continuous network in a liquid phase (gel).

A sol is a stable dispersion of the solid particles (~ 0.1-1 μm) in a liquid. The dispersed phase is so small that gravitational forces are negligible and interactions are dominated by short-range forces, such as Van-der-Waals attraction and surface charge [61]. Driven only by the Brownian motion the dispersed phase homogeneously distributed over the solvent.

The formation of gel occurs when homogeneous dispersion present in the initial sol rigidifies. The transition from sol to gel is called gelation; this process prevents the development of inhomogeneities within the material. The point in time when sol abruptly changes from a viscous liquid state to a solid state is called the gel point. The time required for a gel to form after mixing starting materials together to make the gel is called the gel time [76].

Sol-gel synthesis is utilized to fabricate advanced materials in a wide variety of forms: ultrafine or spherical shaped powders, thin film coatings,

fibers, porous or dense materials, and extremely porous aerogel materials [77].

The main advantages of sol-gel method with respect to the solid state reaction route are:

- An increased chemical homogeneity and good control over stoichiometry;
- Small and uniform particle size, the inter-diffusion distances are short so the reactivity is high, the sintering temperature and time may be reduced;
- The reduced chance of introduction of impurities, do not have to be repeatedly grounded;
- The flexibility of the method, at any time through the whole process, a plurality of parameters can be adapted in order to obtain an optimal result;

2.2.1. Water Based Sol-gel Route

2.2.1.1. Hydrolysis

In water based sol-gel route the metal salts dissolved in water are solvated by water molecules according to:

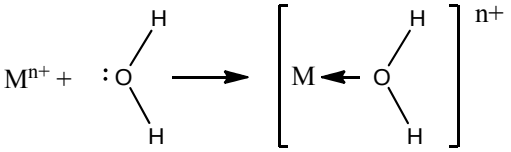

(Eq. 2.1)

Hydrolysis is the deprotonation of a solvated transition metal cation, where charge transfer occurs from the filled bonding orbital of the water

molecule to the empty d orbitals of the transition metal. As a result, the partial charge on the hydrogen increases, making water molecule more acidic. Depending on the number of protons, lost by water molecules surrounding the metal in first solvation shell, the aquo ligand molecule is either transformed into hydroxo ligand OH^-, if only one proton leaves, or into an oxo ligand, O^{2-}, if two protons detaches.

$$[M\text{-}OH_2]^{n+} + H_2O \leftrightarrow [M\text{-}OH]^{(n-1)+} + H_3O^+ \qquad \text{(Eq. 2.2)}$$

$$[M\text{-}OH]^{(n-1)+} + H_2O \leftrightarrow [M{=}O]^{(n-2)+} + H_3O^+ \qquad \text{(Eq. 2.3)}$$

The formation of these three types of ligand can be summed up in the qualitative way using "charge-pH" diagram as shown in *Figure 2.1*. The diagram shows that the hydrolysis of low-valent cations ($z < +4$) give rise to aquohydroxo and/or hydroxo complexes over the complete pH scale, whereas high-valent cations ($z > +5$) yields oxo-hydroxo and/or oxo complexes over the same range of pH.

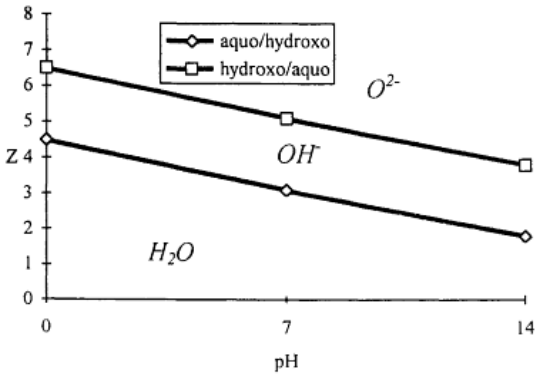

Figure 2.1 *Charge versus pH diagram (adopted from [78]).*

2.2.1.2. Condensation

Depending on the coordination of the metal ion the condensation in aqueous sol-gel system can occur by nucleophilic substitution or addition reaction.

(i) Olation: is a condensation process in which a hydroxy bridge (-OH-) is formed via nucleophilic substitution mechanism:

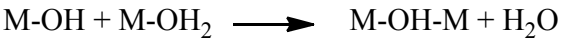

(Eq. 2.4)

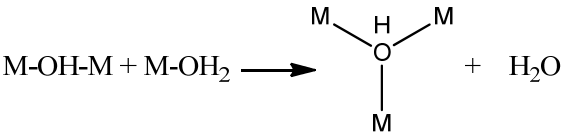

(Eq. 2.5)

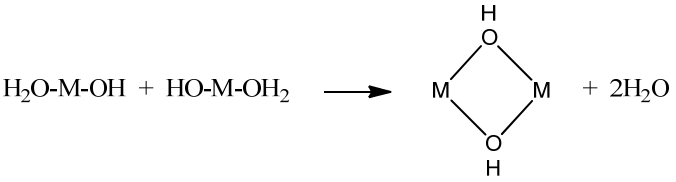

(Eq. 2.6)

(ii) Oxolation: is a condensation process in which an oxo bridge (-O-) is formed by nucleophilic addition:

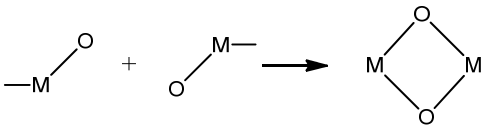

(Eq. 2.7)

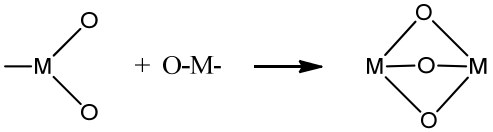

(Eq. 2.8)

The condensation reaction usually occurs at much slower rate than the deprotonation or hydrolysis reaction. For that reason, metal oxides or hydroxides may precipitate during evaporation of solvent before gelation can take place. Therefore, it is important to limit the rate of hydrolysis and promote the condensation reaction.

The use of suitable chelating anions can avoid this problem. The organic coordinating ligands are able to reduce the concentration of free metals in the solution, so that number of solvated water molecules in coordination sphere decreases, slowing hydrolysis process.

Ligands are used in sol-gel route because of their complexing, chelating and bridge forming capability. They are classified as mono-, bi- (acetates) and polydentate ligands (citrates, ethylendiamintetra-acetic acid (EDTA)).

2.3. Sol-gel Combustion Synthesis Route

The sol–gel combustion technique is a unique combination of the chemical sol–gel process and the combustion process. This method involves exothermic and self-sustaining thermally-induced anionic redox reaction of xerogel, which is obtained from aqueous solution containing desired metal salts and a suitable organic fuel [79].

The nitrate salts are favored as precursors because they provide both the metal ions to form the metal oxide and the oxidizer. If the appropriate nitrate is unavailable, ammonium nitrate can be added to the precursor mixture. Therefore, this versatile synthesis route should be applicable to any metal oxide imaginable [80].

The most popular complexing agents are urea, glycine and citric acid. They also serve as reductant being oxidized by nitrate ions, therefore working as a fuel. Good complexant should react non-violently and produce nontoxic gases.

The sol–gel combustion technique exploits the advantages of good chemical homogeneity (mixing at molecular level), easy stoichiometry control, low processing temperature and time. Moreover, powders can be crystallized directly from the xerogel due to the heat generated from the exothermic reaction. Rapid evaluation of a large volume of gases, accompanying by a great mass loss during the xerogel combustion process, limits the occurrence of agglomeration and leads to the formation of fine particles with narrow size distribution [81].

Chapter 3. Fundamental of the Activator Ions

This chapter will briefly introduce the reader with unique properties of lanthanide ions (Sm^{3+}, Eu^{3+}, and Pr^{3+}) used as activators in the host materials described within the thesis.

3.1. Lanthanide Luminescence

The lanthanide series comprise fifteen elements with atomic numbers from 57 (lanthanum, no f-electrons) to 71 (lutetium, 14 f-electrons) and take special place at the bottom of the periodic table [82]. The name lanthanide comes from the Greek word "λανθανειν" which means "to lie hidden". This name arises from the fact that lanthanum was discovered hidden as an impurity in cerium oxide. The series of elements is characterized by the presence of partly filled 4f orbitals, which are well shielded from the environment by the filled $5s^2$ and $5p^6$ outer orbitals [83]. These outer orbitals participate in chemical bonding and interact with neighboring ions. That explains the similarity to each other in relation to their chemical properties, for that reason, it took more than a century to efficiently separate and discover all of them [84]. The most common oxidation state for lanthanide ions is trivalent, however divalent and tetravalent states may also occur in some ions (Eu^{2+}, Sm^{2+}, Yb^{2+}, Ce^{4+} and Tb^{4+}).

The shielded character of 4f shell is also responsible for interesting magnetic and optical properties, with many of them showing very sharp atomic-like emission lines. These lines originate from intraconfigurational $[Xe]4f^n \rightarrow [Xe]4f^n$ transition and have been intensively studied since the beginning of the 20^{th} century. The intensive research led to the invention of fluorescent tubes, white light LEDs, color television, plasma display panels (PDPs), optical fibers, up-conversion phosphors, solid state lasers [85-89].

Besides the intraconfigurational f-f transitions, also interconfigurational $[Xe]4f^n \rightarrow [Xe]4f^{n-1}d^1$ (f-d) and charge transfer (CT) transitions can be observed in lanthanide ions. These transitions are parity allowed and result in a broad absorption band in excitation spectra.

3.2. Russell – Saunders Spectroscopic Terms

In order to describe the electronic states of atoms or ions the spectroscopic terms were developed. For the characterization of the electronic transitions in an ion, the knowledge of the total orbital angular momentum number – ***L***, and total spin – ***S*** is required. The total spin (***S***) of the electronic state can be written as a vector sum of the spin angular momenta of the individual electrons [90]:

$$\vec{S} = \vec{s_1} + \vec{s_2} + \cdots \qquad \text{(Eq. 3.1)}$$

where ***s*** is the spin of the individual electron and equals either +½ or -½. Similarly, the total orbital angular momentum (***L***) is the vector sum of the individual orbital momenta of the electrons:

$$\vec{L} = \vec{l_1} + \vec{l_2} + \cdots \qquad \text{(Eq. 3.2)}$$

where ***l*** is the orbital angular momentum of the individual electron. In spectroscopic notation the first few symbols of ***L*** are:

L =	**0**	**1**	**2**	**3**	**4**	**5**	**6**	**7**
notation	**S**	**P**	**D**	**F**	**G**	**H**	**I**	**K**

and later they are continued alphabetically. By coupling ***S*** and ***L*** the total angular momentum (***J***) is obtained. If the ***S*** and ***L*** values are known, the term symbol of the state can be written and ***J*** values calculated:

$$^{2S+1}L_J \qquad \text{(Eq. 3.3)}$$

The number ***2S+1*** defines the spin multiplicity of the term. ***J*** can be expressed as a vector sum of ***S*** and ***L***:

$$\vec{J} = \vec{L} + \vec{S} \qquad \text{(Eq. 3.4)}$$

and *J* can take the integer values:

$$|L - S| \leq J \leq |L + S| \qquad \text{(Eq. 3.5)}$$

By knowing the amount of electrons (***n***) in the 4f orbital one can calculate the number (***N***) of possible electronic configurations that the lanthanide ion can acquire:

$$N = \frac{14!}{n!\,(14-n)!} \qquad 0 \leq n \leq 14 \qquad \text{(Eq. 3.6)}$$

The number ***N*** for all Ln^{3+} ions is given in the

*Table **3.1***:

Table 3.1 *The number of possible electronic configurations of trivalent lanthanide ions [91].*

Ln^{3+}	**La^{3+}/ Lu^{3+}**	**Ce^{3+}/ Yb^{3+}**	**Pr^{3+}/ Tm^{3+}**	**Nd^{3+}/ Er^{3+}**	**Pm^{3+}/ Ho^{3+}**	**Sm^{3+}/ Dy^{3+}**	**Eu^{3+}/ Tb^{3+}**	**Gd^{3+}**
n	0/14	1/13	2/12	3/11	4/10	5/9	6/8	7
N	1	14	91	364	1001	2002	3003	3432

The ground state term of the ion is found by applying Hund's rule: it has to possess the highest spin multiplicity and the highest total orbital angular momentum. The ***J*** value for the ground state term is calculated as follows:

- if $n \leq 6$, then $J = |L - S|$
- if $n = 7$, then $J = S$
- if $n \geq 8$, then $J = L+S$.

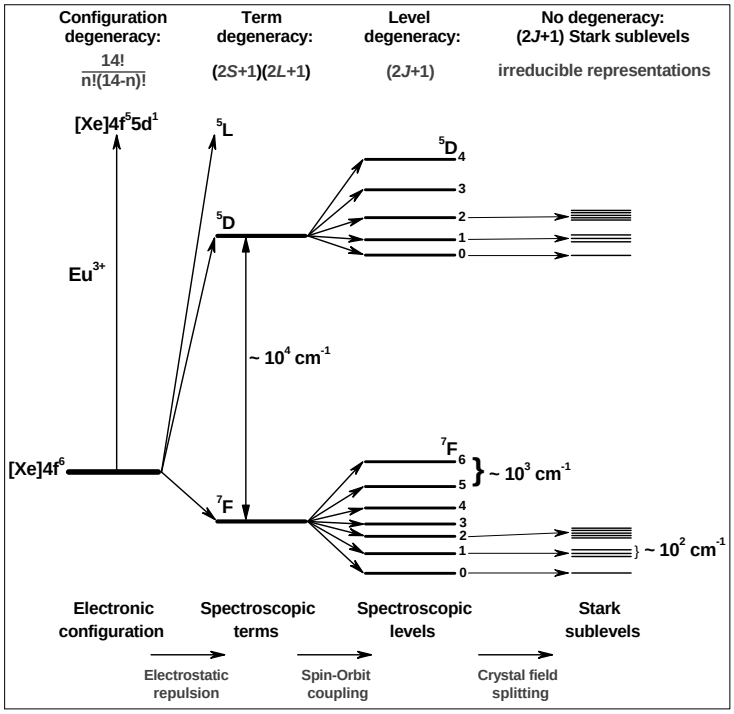

Figure 3.1 *Splitting of the energy levels of the [Xe]4f^6 configuration (Eu^{3+}) (adopted from [91, 92]).*

The energies of the terms are determined by a combination of the interelectronic repulsion, spin-orbit coupling and, in a coordination environment, the ligand field [92]. These interactions that split up the levels of the [Xe]4f^n configuration are explained in *Figure 3.1*, where Eu^{3+} ion was taken as an example.

The first perturbation is caused by the electron repulsion (Coulomb interaction) within 4f orbitals resulting in the terms with the energy separation in the order of 10^4 cm^{-1}. The spectroscopic terms split further into several ***J*** levels, due to spin–orbit coupling (the second perturbation). The number of the ***J*** levels can be calculated employing Eq. 3.5. The spin–orbit coupling leads to ***J*** levels separated by the energy in the order of 10^3 cm^{-1}. The obtained ***J*** levels can split further to so-called Stark sublevels

due to ligand field effect from the coordination polyhedron around the lanthanide ion. The splitting of the Stark sublevels is in the order of 10^2 cm^{-1}. The maximum multiplicity of the ***J*** levels is (***2J + 1***) and depends on the site symmetry of the lanthanide ion. Therefore, the lanthanide ions possessing $[Xe]4f^n \rightarrow [Xe]4f^n$ transitions can be used as probes for clarifying the site symmetries. Moreover, if the ion is affected by the external magnetic field, the spectral lines also split due to Zeeman splitting. All of the mentioned interactions (except Zeeman splitting) are depicted in *Figure 3.1* for better visualization.

3.3. Selection Rules for Intraconfigurational f-f Transitions

Electronic transitions of lanthanide ions occur through the interaction of their electrons with the electric or magnetic component of the electromagnetic radiation. However, not every possible transition is observed in atomic spectra. The 4f transitions of trivalent lanthanides are situated in the NIR, VIS and UV parts of the spectrum.

The 4f-4f transitions are forbidden by the Laporte (parity) selection rule, which means that transition cannot occur between the same shells ($\Delta L \neq 0$). In other words, the sum of angular momenta of electrons in the initial and final states must change by an odd integer, i.e. the initial and final states must be of opposite parity (**P**) [93].

$$P = (-1)^{\Sigma i} \qquad \text{(Eq. 3.7)}$$

The parity selection rule originates from the fact that absorption of the light through electric dipole transition requires a change of electric dipole in the transition state between ground state and excited state [90]. The parity selection rule forbids electric dipole (ED) transition between states with the

same parity and applies to electronic transitions within the d-shell, within the f-shell, and between the d and s shells. Since electric dipole transitions are forbidden only magnetic dipole (MD) transitions can occur [94]. Magnetic dipole transitions are generally weaker than ED transitions by a factor of 10^5 [95]. However, in non-centrosymmetric environment, the electric dipole f-f transitions become weakly allowed by mixing of opposite parity wave functions (primarily 5d) into the 4f wave functions. Thus, the parity forbidden intraconfigurational f-f transition gain some intensity from the parity allowed 4f-5d transitions [96].

The spin selection rule forbids electronic transitions between levels with different spin states ($\Delta S \neq 0$). The spin selection rule arises from the fact, that light (electromagnetic radiation) does not affect the spin of an electron. The other selection rules that apply to ***S***, ***L***, and ***J*** quantum numbers are summarized in *Table 3.2*.

Table 3.2 *Selection rules for f-f transitions between spectroscopic levels [91].*

Transition	**Parity**	ΔS	ΔL	ΔJ[a]
ED	Opposite	0	≤ 6 ($\Delta l = \pm 1$)	≤ 6 (2, 4, 6 if J or $J' = 0$)
MD	Same	0	0	0, ±1
EQ	Same	0	0, ±1, ±2	0, ±1, ±2

[a] $J = 0 \leftrightarrow J' = 0$ transitions are always forbidden.

ED – electric dipole; MD – magnetic dipole; EQ – electric quadrupole.

3.4. Interconfigurational $4f^n$-$4f^{n-1}5d$ and charge transfer transitions

The interconfigurational $[Xe]4f^n \leftrightarrow [Xe]4f^{n-1}5d$ transitions can be observed in divalent lanthanides, which show relatively low electron affinity (Eu^{2+}, Yb^{2+}, Sm^{2+} and Tm^{2+}) and in trivalent lanthanides, which have relatively high stability in tetravalent state (Ce^{3+}, Nd^{3+}, Tb^{3+} and Pr^{3+}). These transitions are parity allowed and therefore more intense than intraconfigurational f-f transitions. The $4f^n \leftrightarrow 4f^{n-1}5d$ transitions are usually located in the (vacuum)ultraviolet spectral region. The 5d orbitals of lanthanide ions are more spatially extended than 4f orbitals. These 5d orbitals participate in the chemical bonding and are greatly influenced by the local surroundings (host lattice). The positions of 5d energy levels depend on several factors: nephelauxetic effect (also known as covalency), crystal field splitting and Stokes' shift [97].

- The term nephelauxetic means "electron cloud expanding" and can be explained considering the covalency between two atoms. For materials like rock salt (NaCl) the difference in electronegativity (EN) is large and the electrons will reside on either Na^+ or Cl^- ions resulting in ionic bonding. For a decreasing EN difference in the bonding between two atoms, the covalency increases. In the case of lanthanide compounds, the 5d electron becomes more delocalized over the ligands with increasing covalency [98]. Therefore, an increase in the covalency reduces the energy difference between the 4f ground state and the $4f^{n-1}5d$ excited state. As a consequence, the lowest excited $4f^{n-1}5d$ state shifts towards lower energy.
- When the lanthanide ion is not in a spherical symmetric environment, but e.g. in an ordered crystalline environment, crystal field splitting will occur which causes a splitting of the 5d energy levels. The way they split up is determined by the number of ligands, their charge, their distance, and the

coordination geometry. For instance, when lanthanide ions occupy a site with low coordination number (e. g. octahedron) the distances between the central ion and the ligands are small and the crystal field splitting is large. For higher coordination number, the interionic distances increase, weakening the crystal field strength [99]. Furthermore, nitrides (N^{3-}) have a higher formal charge and will generate stronger crystal field than oxides (O^{2-}) or fluorides (F^{-}). The stronger crystal field will result in a lowering of the lowest emitting d-level and shift the d-f emission to longer wavelengths.

- The Stokes shift is the energy difference between the excitation and the emission maximum and determined by lattice relaxation effect.

The influence of the three above explained factors on the $4f^n \leftrightarrow 4f^{n-1}5d$ transitions is schematically presented in *Figure 3.2*.

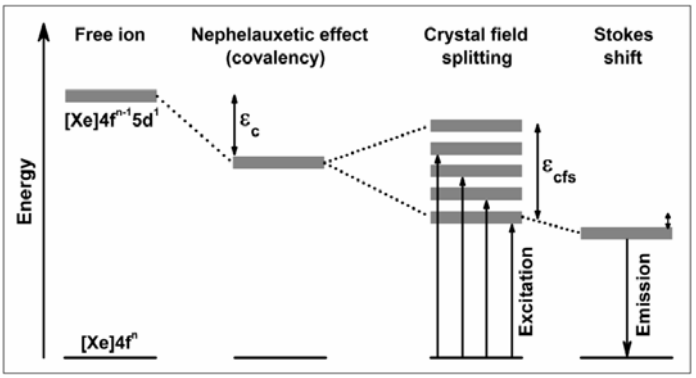

Figure 3.2 *The influence of covalency, crystal field splitting and Stokes shift on the position of 5d energy levels.*

The second type of allowed optical transitions are charge transfer transitions (CT), which can be considered as $[Xe]4f^n \rightarrow [Xe]4f^{n+1}L^{-1}$, where L is a ligand. Generally, the CT transitions are common for lanthanide ions that can be reduced (Eu^{3+}, Sm^{3+} and Yb^{3+}), and $[Xe]4f^n \leftrightarrow [Xe]4f^{n-1}5d$ transitions for ions that can be oxidized (Ce^{3+}, Pr^{3+} and Tb^{3+}) [97].

Chapter 4. Properties of the Host Materials

4.1. Crystal Structures of $MSnO_3$ (M = Ca, Sr, Ba)

Compounds belonging to the perovskite type have in general the formula ABO_3 where the sum of the cation valencies is 6. $BaSnO_3$ crystallizes in an ideal cubic crystal lattice with the space group *Pm3m* (221) [100]. This structure consists of a corner-sharing SnO_6 octahedral framework with the barium ions filling the cubo-octahedral cavities (CN = 12) in the structure, as shown in *Figure 4.1c*. An additional four barium atoms surround each oxygen in a plane perpendicular to the Sn-O-Sn bond, but the Sn–O distances (2.055 Å) are much shorter than the Ba–O distances (2.905Å) [101].

When Ba^{2+} is replaced by Ca^{2+} or Sr^{2+}, then two main types of deformation are possible, and may occur separately or together [102]. Firstly, the unit cell shape is changing, by altering either the relative lengths of the cell-edges or the axial angle. Secondly, if the atomic parameters of some or all of the atoms are slightly altered, then slight displacement in any direction involves a lowering of the symmetry, and in general also a doubling of at least one cell edge. Conversely, a doubled cell edge implies atomic parameters different from those of the ideal structure.

The crystal structures of $CaSnO_3$ and $SrSnO_3$ were first solved by Vegas et al. in 1986 [103] and are shown in *Figure 4.1a* and *b*, respectively. In $CaSnO_3$ and $SrSnO_3$ compounds the local octahedral environment about Sn^{4+} is maintained, and the corner-sharing octahedral connectivity of the perovskite structure is also preserved, but the octahedral tilting lead to significant changes in the environment about the A-site cation (Ca or Sr) as well as oxygen. $CaSnO_3$ and $SrSnO_3$ are both distorted from ideal cubic into

orthorhombic structure with *Pnma* symmetry by an octahedral tilting distortion, which is driven by a mismatch in the fit of the alkaline earth cation to the cubo-octahedral cavity in the corner-sharing octahedral network due to the smaller ionic radius of Sr^{2+} or Ca^{2+}than Ba^{2+}. The average Sn–O distance and the octahedral configuration about tin are relatively insensitive to substitutions on the A-site. However, the Sn–O–Sn bond becomes increasingly distorted from linear with decreasing size of the A-site cation. Such a distortion in the nonlinear Sn–O–Sn bond would be expected to have a great influence on the migration of charge carriers and delocalization of excited energy and thus on photophysical and photocatalytic properties of stannates [101, 104].

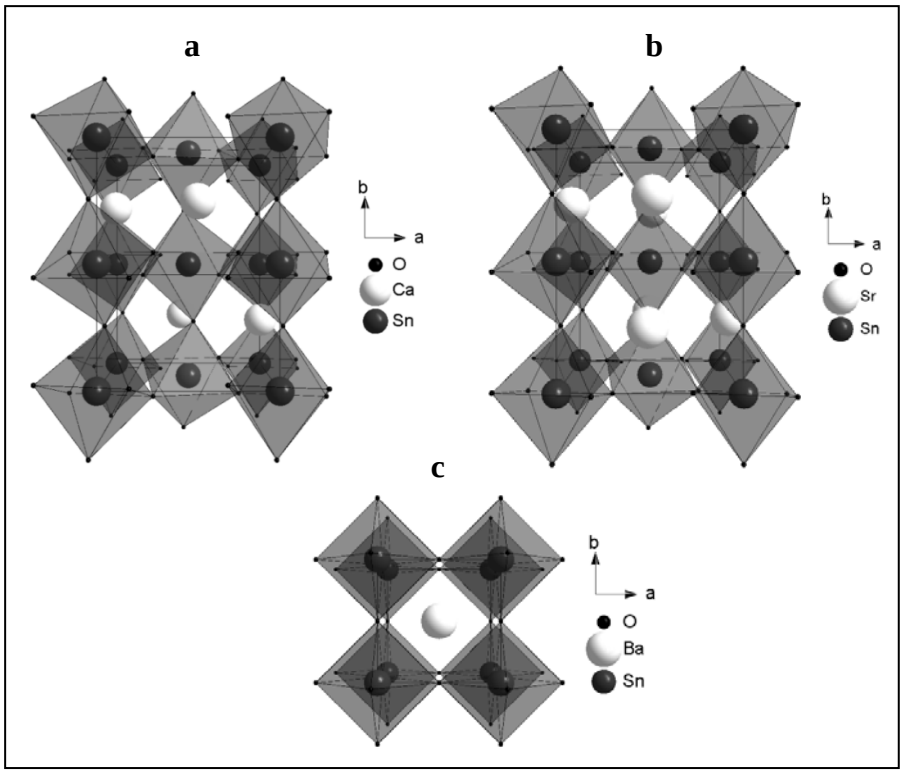

Figure 4.1 *Crystal structure of (a) $CaSnO_3$, (b) $SrSnO_3$ and (c) $BaSnO_3$ along the c-axis.*

4.2. Crystal Structures of M_2SnO_4 (M = Ca, Sr, Ba)

The refinement of the crystal structure revealed that Ca_2SnO_4 belongs to the Sr_2PbO_4-type structure with an orthorhombic unit cell and space group Pbam (#55). In this structure type, the Ca atoms occupy a 4h site (x, y, 1/2) and are coordinated by seven oxygen atoms. The Sn atoms occupying a 2a site (0, 0, 0) are coordinated by six oxygen atoms [105, 106]. On the other hand, Sr_2SnO_4 and Ba_2SnO_4 adopt layered structures derived from the K_2NiF_4 structure type. Ba_2SnO_4 crystallizes in the undistorted tetragonal space group *I4/mmm* (#139). In the undistorted K_2NiF_4 structure, the larger cations are surrounded by nine anions. This coordination number is, however, reduced to seven in Sr_2SnO_4 due to the titling of the SnO_6 octahedrons and leads to an orthorhombic distortion of the K_2NiF_4 structure at room temperature [42, 107]. In both structure types, SnO_6 octahedra are connected in low-dimensional form; SnO_6 octahedra are linked by sharing edges with each other and forming one-dimensional chains in Ca_2SnO_4 and two-dimensional perovskite-like layers in Sr_2SnO_4 and Ba_2SnO_4 [66], as shown in *Figure 4.2*. In this kind of low-dimensional structure, it is easy to implant other ions into the host lattice and create traps located at suitable depths that can store the excitation energy and emit light upon re-activation at room temperature [108, 109]. Considering the ionic radii it can be assumed that Sm^{3+}ions (1.10 Å→ CN = 6; 1.16 Å→ CN = 7 and 1.27 Å→ CN = 9) have a tendency to replace closer in size Ca^{2+} (1.2 Å→ CN = 7) and Sr^{2+} (1.35 Å→ CN = 7) ions, rather than occupy Sn^{4+} sites (0.83 Å→ CN = 6)[110]. However, in Ba_2SnO_4 structure Ba^{2+} is coordinated by nine oxygen ions (1.61 Å→ CN = 9). We assume that Sm^{3+} ions will occupy closer in size Sn^{4+} octahedral site in Ba_2SnO_4 structure according to the Vegard's law [64].

Moreover, a closer look at the Ba_2SnO_4 structure (*Figure 4.3a*), shows that it consists of an intergrowth of perovskite-like blocks of composition $BaSnO_3$ and fragments of BaO (NaCl type).

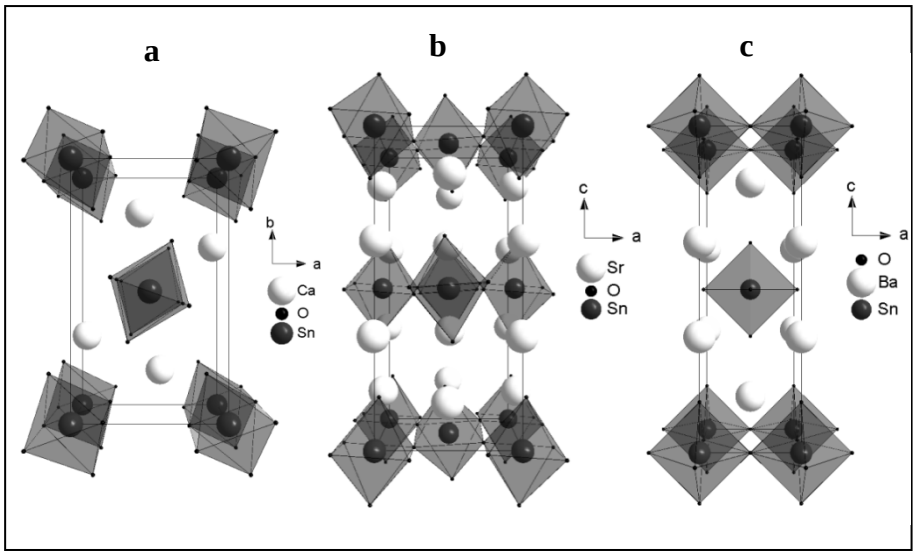

Figure 4.2 *Crystal structure of (a) Ca_2SnO_4 along the c-axis, (b) Sr_2SnO_4 along the b-axis and (c) Ba_2SnO_4 along b-axis.*

Both blocks composing the structure are drawn in *Figure 4.3b* and *c*, whereas the BaO fragment is outlined in the unit cell of the rock salt BaO structure in *Figure 4.3c*. The other component of the structure, the $BaSnO_3$ blocks, are formed by slightly distorted cubes of Ba ions (4.14 x 4.14 x 3.88 Å), centered by the Sn^{4+} ions. The topology and distances of the basic units BaO and $BaSnO_3$ remain unaltered in the more complex compounds [111].

Wang et al. [112] demonstrated on the basis of atomistic semi-empirical simulations and density functional theory (DFT) calculations for the $BaSnO_3$ structure that trivalent dopants, Sc, In, and Y have relatively favorable solution energies at the Sn site. For cations larger than Sm^{3+}, some

partial substitution on Ba-site cannot be discarded. The substitution of Sm^{3+} ion for M^{2+} is non-equivalent substitution and can be expressed as follows [113]:

$$Sm_M \leftrightarrow Sm_M^{\cdot} + e' \qquad \text{(Eq. 4.1)}$$

To fulfill the charge neutrality requirements an excess of positive charge in the lattice must be compensated. There are two possible pathways of charge compensation: electronic and vacancy compensation.

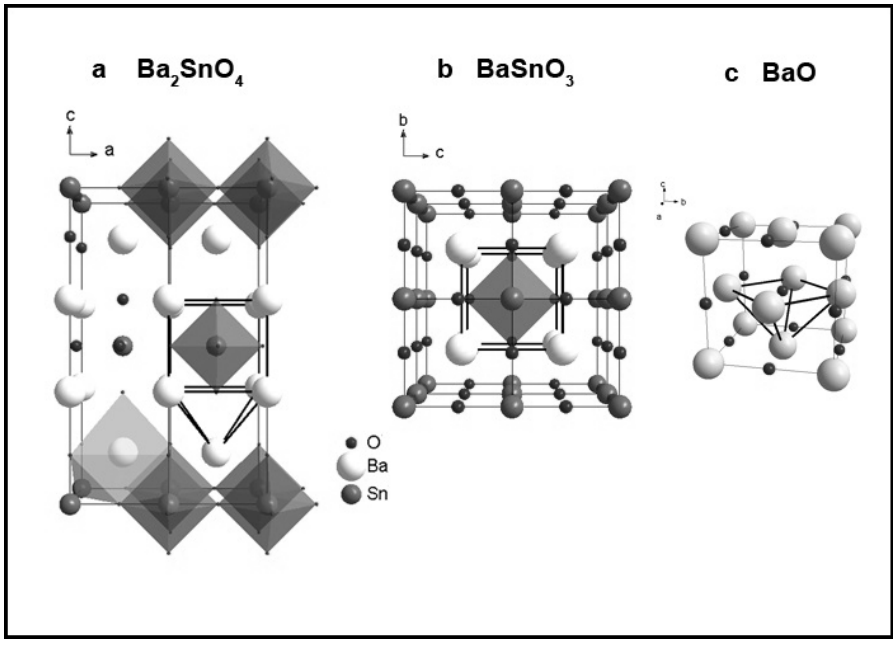

Figure 4.3 *Crystal structure of (a) Ba_2SnO_4, (b) $BaSnO_3$ and (c) the unit cell of the rock salt type BaO structure.*

In the first case, there is a possibility that some of the Sn^{4+} ions capture electrons liberated in *Eq. 4.1* and change their valence state to Sn^{3+} and/or Sn^{2+} resulting in the formation of structure defects with localized charge carriers (electrons) and can act as hole trapping centers. The other possible pathway of charge compensation is that two Sm^{3+} ions replace three M^{2+}

ions, which create two $Sm_M^{\cdot}$ positive defects and one $V_M^{''}$ (vacancy) negative defect [69, 113]:

$$2Sm^{3+} + 3M^{2+} \rightarrow 2Sm_M^{\cdot} + V_M^{''} \qquad \text{(Eq. 4.2)}$$

where $Sm_M^{\cdot}$ and $V_M^{''}$ act as the electron and hole trap sites, respectively. In the present case, trivalent Sm^{3+} ions not only play the role of activator, but also serve as aliovalent auxiliary dopant to create defects.

The literature observation clearly suggests to elaborate a novel synthetic approach for the preparation of uniform SnO_2 films which will be derived from highly pure solutions containing no interfering counter-ions in neutral medium using innocuous H_2O as a solvent. Also, a novel and versatile synthetic approach for the preparation of alkaline earth metal (Ca, Sr and Ba) stannates via aqueous sol-gel (combustion) method is very much desired. The lanthanide-doped alkaline earth metal stannates possibly would act as novel and efficient phosphors. Thus, the photoluminescence properties of Sm^{3+}, Eu^{3+} or Pr^{3+} doped different stannates ($MSnO_3$ and M_2SnO_4; M- alkaline earth metal) will be investigated. Initially, a simple, inexpensive and environmentally benign 'chimie douce' synthetic approach based on the gel to crystallite conversion (G-C) method will be tested by preparing strontium stannate $SrSnO_3$, strontium titanate $SrTiO_3$, and mixed strontium stannates-titanates $SrSn_{1-x}Ti_xO_3$ (x = 0.05–0.5 mol %).

Chapter 5. Experimental

5.1. Synthesis

5.1.1. Low Temperature Synthesis of Stannate-Titanate Ceramics via Gel to Crystallite Conversion Method

$SrTiO_3$, $SrSnO_3$ and $SrSn_{1-x}Ti_xO_3$ (x = 0.05–0.5 mol%) were prepared by gel to crystallite (G-C) conversion method [114]. For the synthesis of $SrTiO_3$, $TiOCl_2 \cdot (HCl)_x$, $Sr(OH)_2 \cdot 8H_2O$ and aqueous ammonia solution were used as starting materials. The gel of hydrated titania $TiO_2 \cdot xH_2O$ ($80<x<120$) was prepared by addition of ammonium hydroxide at approximately 40 ºC to a solution of titanium oxychloride up to pH = 8. The gels were washed free of chloride and ammonium ions. The gel was suspended in 0.5 M $Sr(OH)_2$ solution in a flask fitted with a water-cooled reflux condenser. Air in the vessel was displaced by argon and fresh entry of atmospheric CO_2 was prevented by the use of an alkali guard-tube. The Ti/Sr molar ratio was varied from 0.95 to 1.05. The mixture was stirred under reflux conditions at 70-100 ºC for 1-4 h with constant stirring. The remaining solid phase was filtered, washed free of $Sr(OH)_2$ ions and air dried. Recovered solids were calcined at the desired temperature up to 1100 ºC. The $SrSnO_3$ was synthesized using analogous procedure, only tin (IV) chloride was used instead of titanium oxychloride. In the case of $SrSn_{1-x}Ti_xO_3$ compounds the stoichiometric amounts of tin and titanium were selected in the G-C processing.

5.1.2. Synthesis of Citrato Peroxo Sn(IV) Precursor

The aqueous citrato peroxo Sn(IV) precursor was synthesized by following procedure. Firstly, tin(II) oxalate was dispersed with a minimal amount of distilled water by stirring in a beaker at room temperature.

Secondly, 35% hydrogen peroxide was added to the suspension up to a 1:12 Sn(IV):H_2O_2 molar ratio. The beaker was heated on a hot plate at 80°C and the mixture was stirred for 30 min until a clear and transparent solution is obtained.

Citric acid (CA) was then added to the above solution in the desired CA to Sn(IV) molar ratio. The obtained mixture was heated while stirring for 1 h at 80 ºC in a beaker closed with a watch glass. The resulting acidic solution was neutralized while keeping the beaker in an ice water bath by the addition of concentrated ammonia up to pH ~ 7-8. A simplified synthesis scheme is presented in *Figure 5.1*. Amorphous, hygroscopic gels of the citrato peroxo Sn(IV) precursor solutions were obtained by drying a few drops of the aqueous precursor solutions in a Petri dish at 100 °C in an air-flushed furnace for at least 2 days.

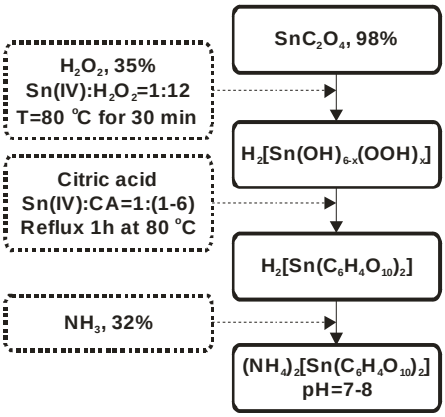

Figure 5.1 *Aqueous citrato peroxo Sn(IV) precursor synthesis scheme.*

The formula of the citrato peroxo Sn(IV) complex was proposed based on the results reported by Bichara et al., who have studied Sn(IV) complex formed after anodic dissolution of a tin surface through its passive oxide film in citric-citrate aqueous solution buffer pH = 3. Based on ab-initio

calculations theoretical structure for the studied $[Sn(C_6H_4O_7)_2]^{2-}$ complex is depicted in *Figure 5.2*.

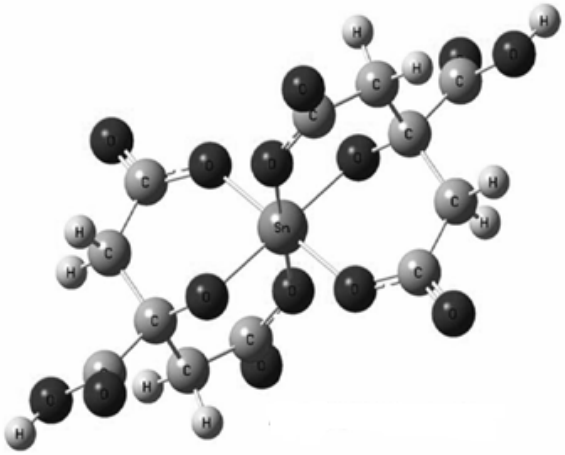

Figure 5.2 *Theoretical structure of* $[Sn(C_6H_4O_7)_2]^{2-}$ *complex (adopted from [115]).*

In our experiment, after addition of citric acid to the intermediate species of stannic acid, it reacts with excess of hydrogen peroxide and/or takes active oxygen from hydroperoxo stannate species, to give peroxy acid. Assuming that all three carboxyl groups of citric are replaced by peroxy groups, we propose that formula for the citrato peroxo Sn(IV) complex is $H_2[Sn(C_6H_4O_{10})_2]$. During final stage of neutralization with ammonia the following complex is formed $(NH_4)_2[Sn(C_6H_4O_{10})_2]$ (*Figure 5.3*).

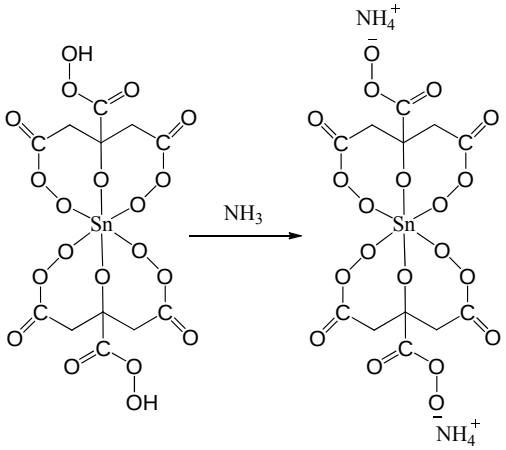

$H_2[Sn(C_6H_4O_{10})_2]$ $(NH_4)_2[Sn(C_6H_4O_{10})_2]$

Figure 5.3 *The structure of citrato peroxo Sn(IV) complex at pH=7-8.*

5.1.3. Sol-gel (Combustion) Synthesis of Alkaline Earth Metal Stannate Powders

For the preparation of alkaline earth metal (Ca, Sr and Ba) precursor solution corresponding metal hydroxides or acetates were used. Alkaline earth metal precursor solution was obtained by dissolving hydroxide or acetate in an aqueous solution of 3 M citric acid (M:CA=1:6) constantly stirring at room temperature to avoid the formation of carbonates. After complete dissolution the concentrated ammonia was used to adjust pH to ~7 [116].

It was found that neutral conditions are suitable for the preparation of stable strontium and barium precursor solutions. However, calcium ions precipitate during neutralization step with ammonia and, consequently, prefer acidic media. For that reason, sol-gel synthesis procedure was modified by using calcium nitrate tetrahydrate as starting salt, without addition of ammonia and reducing the total metal ion to citric acid ratio (1:3).

The alkaline earth metal and citrato peroxo Sn (IV) precursors were mixed in the stoichiometric ratios 1:1 and 2:1 according to the finally aimed powders with nominal chemical composition of $MSnO_3$ and M_2SnO_4, respectively. The bimetallic precursors were homogenized by constantly stirring at 80 °C for 1 h. The Sr-Sn-O (Sr-Sn) and Ba-Sn-O (Ba-Sn) containing precursor solutions with pH ~ 7 were heated in an open beaker in ambient conditions at ~150 °C to promote dehydration that leads to the formation of white foams gradually turning into brown-black gels. Amorphous and highly hygroscopic Sr-Sn and Ba-Sn precursor gels were dried in the oven at 150 °C for 2 days. The Ca-Sn-O (Ca-Sn) containing precursor solution was concentrated by slow evaporation at ~120 °C under constant stirring. During last stages of gelation, self-propagating gel combustion process started and was accompanied with evolution of gases. This reaction is highly exothermic because two strong oxidizing agents (peroxide and nitrate) are present in the system together with 'organic fuel' (citrate). The resulting voluminous fluffy yellowish products were dried in the oven at 150 °C over night. Dried gels were ground in an agate mortar and calcined for 5 h at 500 °C (1 °C/min) in air. After an intermediate grinding the powders were additionally sintered for 5 h at 800 °C or 1000 °C (5 ºC/min) in air. A simplified synthesis schemes used for the sol-gel preparation of alkaline earth metal (Ca, Sr and Ba) meta- and ortho-stannates are presented in *Figure 5.4*.

5.1.4. Synthesis of $M_2SnO_4:Sm^{3+}$ (M = Ca, Sr and Ba)

Samarium-doped calcium, strontium and barium ortho-stannate powder samples were prepared by conventional high temperature solid-state reaction method. For this purpose, stoichiometric amounts of raw materials ($CaCO_3$, $SrCO_3$, $BaCO_3$, SnO_2 and Sm_2O_3) were thoroughly ground in an agate

mortar (acetone was used as medium) and then annealed at 1400 °C for 10 h in air (heating rate 5 °C/min). Three series of samples, with Sm^{3+} concentrations ranging from 0.1 to 4 mol % of M^{2+} ions in M_2SnO_4, were prepared.

5.1.5. Synthesis of $M_2SnO_4:Eu^{3+}$ (M = Ca, Sr and Ba)

Europium-doped calcium, strontium and barium ortho-stannate phosphor powders were prepared by conventional high temperature solid-state reaction. The stoichiometric amounts of high purity raw materials ($CaCO_3$, $SrCO_3$, $BaCO_3$, SnO_2 and Eu_2O_3) were thoroughly mixed in the agate mortar using acetone as grinding media. The mixture of starting materials were dried, transferred to the alumina crucibles and annealed at 1400 °C for 10 h in air. Three series of samples, with Eu^{3+} concentrations ranging from 0.1 to 16 mol % of M^{2+} ions in M_2SnO_4, were prepared.

5.1.6. Synthesis of $CaSnO_3:Pr^{3+}$, $SrSnO_3:Pr^{3+}$ and $Ca_2SnO_4:Pr^{3+}$

Praseodymium-doped meta- and ortho-stannate powder samples were synthesized by traditional solid state method. The stoichiometric amounts of high purity raw materials ($CaCO_3$, $SrCO_3$, SnO_2 and $Pr_2(C_2O_4)_3 \cdot 10H_2O$) were thoroughly mixed in the agate mortar using acetone as grinding media. The mixture of starting materials were dried, transferred to the alumina crucibles and annealed at 1200 °C and 1400 °C for 10 h in air in order to obtain single phase meta- and ortho-stannate samples, respectively. A series of phosphors with dopant concentration ranging from 0.1 to 4 mol % of Ca^{2+} and Sr^{2+}ions were prepared. The undoped $SrSnO_3$ host material was obtained in the same way just without addition of Pr^{3+} source.

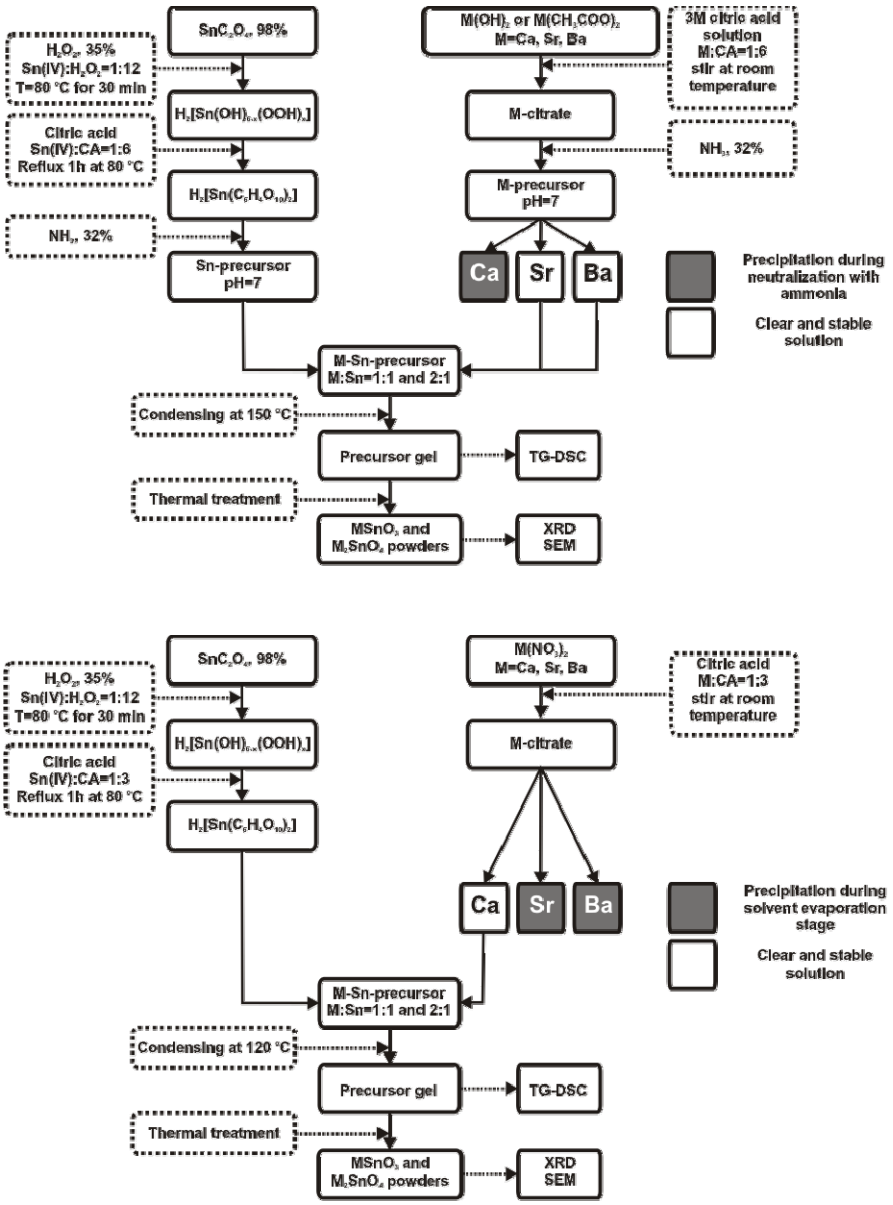

Figure 5.4 *Schematic diagrams of sol-gel (combustion) synthesis of alkaline earth metal stannates.*

5.2. Chemicals

The starting materials were $TiOCl_2 \cdot (HCl)_x$ (Sigma-Aldrich, Ti~15%; HCl 38-42%), $Sr(OH)_2 \cdot 8H_2O$ (95%, Sigma Aldrich), ammonia (NH_3, Merck, 32% in H_2O, extra pure), $SnCl_4 \cdot 5H_2O$ (≥98%, Sigma-Aldrich), SnC_2O_4 (98%, Alfa Aesar), H_2O_2, (35 wt.% in H_2O, Acros Organics), citric acid $C_6H_8O_7$ (≥99,5%, Sigma-Aldrich), $Ca(OH)_2$ (≥95.0%, Sigma-Aldrich), $Sr(OH)_2 \cdot 8H_2O$ (99%, Alfa Aesar), $Ba(OH)_2 \cdot 8H_2O$ (≥98%, Sigma-Aldrich), $Ca(CH_3COO)_2 \cdot H_2O$ (≥99.0%, Sigma-Aldrich), $Sr(CH_3COO)_2$ (≥98%, Sigma-Aldrich), $Ba(CH_3COO)_2$ (≥99%, Sigma-Aldrich), $Ca(NO_3)_2 \cdot 4H_2O$ (99%, Alfa Aesar), $CaCO_3$ (≥99%, Sigma Aldrich), $SrCO_3$ (≥99.9%, Aldrich). $BaCO_3$ (99%, Alfa Aesar), SnO_2 (≥99%, Merck), Sm_2O_3 (99.9%, Alfa Aesar), Eu_2O_3 (99.99% Treibacher), $Pr_2(C_2O_4)_3 \cdot 10H_2O$ ((≥99%, Merck).

5.3. Materials Characterization

5.3.1. Powder X-ray Diffraction

Powder X-ray diffraction data were collected in the range of $10 \leq 2\theta \leq 80°$ using Ni-filtered Cu Kα radiation on Rigaku MiniFlex II diffractometer working in Bragg-Brentano (θ/2θ) geometry. The step width and integration time was 0.02° and 1 s, respectively. Phase purity of the obtained films was studied on a Bruker D8 discoverer diffractometer equipped with HTK-1200 high temperature chamber (Anton-Paar). XRD patterns were recorded in situ during heating of the sample in static air (10 °C/min).

5.3.2. SEM Analysis

Scanning electron microscopy (SEM) images were recorded using EVO 50 XVP, FE-SEM Zeiss Ultra 55 or FE-SEM Hitachi SU-70 microscopes to collect information about grain size, shape and the degree of powder agglomeration. The surface images of the deposited layers were taken by a FEI Quanta 200FEG SEM scanning electron microscope.

5.3.3. TG-DSC Analysis

The thermal decomposition of the precursor gels was analyzed through thermogravimetric and differential scanning calorimetry (TG-DSC) analysis using Perkin Elmer STA 6000 Simultaneous Thermal Analyzer. Dried samples of about 5–10 mg were put in a corundum pan and heated from 25 to 950 °C at a heating rate of 10 °C/min in a dry flowing air (20 mL/min).

5.3.4. ICP-AES Analysis

The metal ion concentration of the different precursor solutions was determined by means of inductively coupled plasma atomic emission spectroscopy (ICP-AES, Perkin-Elmer Optima 3300 DV). Samples were diluted with 5% HNO_3 (J. T. Baker, 69–70%, Baker Instra-analyzed Reagent) so that the concentrations along calibration curve fall into the 1–10 ppm region.

5.3.5. FTIR Analysis

Fourier Transform Infrared (FTIR) spectra of gels and powders were recorded at room temperature on a Bruker Vertex 70 spectrometer using KBr pellets (4000–400cm^{-1}, 128 scans, resolution 4 cm^{-1}).

5.3.6. Deposition of thin films

Multi layered tin dioxide films were prepared by spin coating technique. Drops of a 0.2 M citrato peroxo Sn(IV) precursor solution (Sn(IV):CA=1:6; pH=7) were placed onto chemically cleaned SPM/APM (sulphuric acid peroxide mixture/ammonia peroxide mixture) [117] SiO_2(1.2 nm)/Si substrates. After coating (30 s, 3000 rpm, 1000 rpm/s), the as deposited wet film was treated on 2 different hot plates (in static air) as follows: 2 min at 250 $^{\circ}$C, 2 min at 400 $^{\circ}$C. The complete cycle is repeated 10 to 20 times prior to a final anneal in the tube furnace at 550 $^{\circ}$C for 1 h in dry air.

5.3.7. UV/VIS Spectroscopic Investigations

Excitation and emission spectra were recorded on the Edinburgh Instruments FSL920 fluorescence spectrometer equipped with 450 W Xe arc lamp, mirror optics for powder samples and a cooled (-20 °C) single-photon photomultiplier (Hamamatsu R2658P). The photoluminescence emission spectra were corrected by a correction file obtained from tungsten incandescent lamp certified by the NPL (National Physics Laboratory, UK) and excitation spectra were corrected by reference detector.

The reflection spectra were recorded on the same model spectrometer equipped with an integration sphere coated with barium sulfate. $BaSO_4$ (99% Sigma-Aldrich) was used as a reflectance standard.

For thermal quenching (TQ) measurements a cryostat ‘‘MicrostatN’’ from the Oxford Instruments has been applied to the above mentioned spectrometer. Liquid nitrogen was used as a cooling agent. Measurements were carried out from 100 to 500 K in 50 K steps.

5.3.8. Lifetime Measurements

Photoluminescence lifetimes were measured with the Edinburgh Instruments FSL920 spectrometer equipped with the μF900 flash lamp and a Hamamatsu extended red sensitivity photomultiplier tube. Data were acquired in a gated single photon counting (MCS) mode.

5.3.9. LE Calculations

The LE, in lumen per watt optical, is a parameter describing how bright the radiation is perceived by the average human eye. It scales with the photopic human eye sensitivity curve $V(\lambda)$ and can be calculated from the emission spectrum $I(\lambda)$ of the sample as [118]:

$$LE\left(lm/W_{opt.}\right) = 683\left(lm/W_{opt.}\right) \times \frac{\int_{360nm}^{830nm} I(\lambda)V(\lambda)d\lambda}{\int_{360nm}^{830nm} I(\lambda)d\lambda} \quad \text{(Eq. 5.1)}$$

5.3.10. $TQ_{1/2}$ Calculations

For the calculation of $TQ_{1/2}$ values (the temperature, at which phosphor loses half its efficiency) the Boltzmann sigmoidal fit of temperature dependent emission integrals was employed. The fit equation is [119].

$$y(x) = A_2 + \frac{A_1 - A_2}{1 + e^{(x-x_0)dx}} \quad \text{(Eq. 5.2)}$$

Where $y(x)$ is normalized emission integral value at given x, the independent variable x is the temperature, A_1 is initial value (left horizontal asymptote), A_2 is the final value (right horizontal asymptote), x_0 is the center (point of inflection, $x_0 = TQ_{1/2}$) of the sigmoid, and dx is the change in x corresponding to the most significant change in $y(x)$ values. Fittings were performed on normalized emission integral data, therefore, the A_1 and A_2 values were set to 1 and 0, respectively.

5.3.11. Dielectric measurements

Dielectric measurements were performed using precision LCR meter HP 4284A in 100 Hz – 1 MHz frequency range during cooling with 1K/min rate for both $BaSnO_3$ and Ba_2SnO_4 samples. In both cases sample was in form of pellet, $BaSnO_3$ and Ba_2SnO_4 were approximately 0.8 mm thick with silver paste used to produce contact area of around 8 mm^2. Temperature ranges were 300 K – 1000 K for both samples.

Chapter 6. Low Temperature Synthesis of Strontium Stannate Titanate Ceramics

6.1. XRD and SEM Analysis

The powder X-ray diffraction (XRD) patterns of $SrTiO_3$ samples prepared at different temperatures are shown in *Figure 6.1* and *Figure 6.2*.

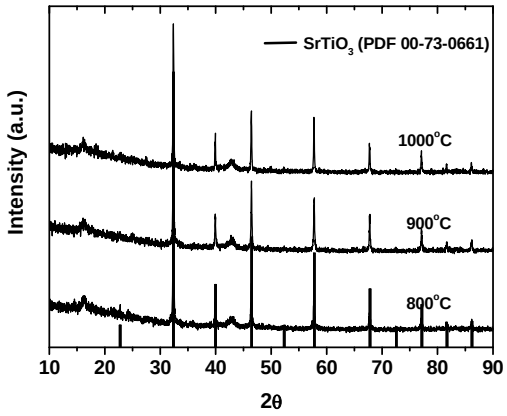

Figure 6.1 *Powder XRD patterns of $SrTiO_3$ samples annealed at different temperatures for 5 h in air.*

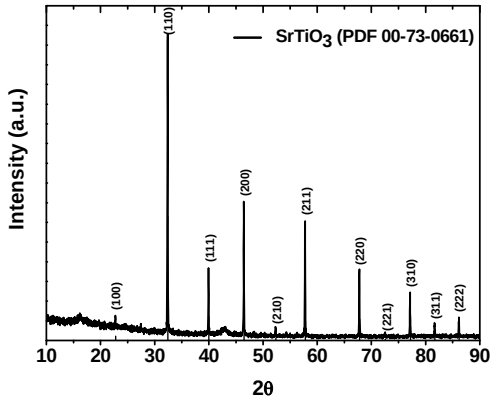

Figure 6.2 *Powder XRD pattern of $SrTiO_3$ annealed at 1100 ºC.*

The XRD patterns of $SrTiO_3$ samples annealed from 800 to 1000 ºC for 5 h in air show the formation of single-phase powders with the cubic perovskite structure. No X-ray reflections arising from byproducts such as rutile (TiO_2) or $SrCO_3$ are observed after annealing the powders at higher temperatures indicating the high purity of synthesis products. According to the literature data, all diffraction lines observed in *Figure 6.1* can be assigned to the $SrTiO_3$ phase (ICSD#00-073-0661). The number of indexed lines = 11. The two unindexed lines observed at around $2\theta \approx 17$ º and $2 \approx 42.5$ º could be attributed to the aluminum sample holder. Moreover, it is evident from XRD data that crystallinity of the samples increases with increasing synthesis temperature. The XRD pattern of $SrTiO_3$ sample annealed at 1100 ºC (*Figure 6.2*) contains very sharp reflections. The most intensive lines are (110) – 100%, (200) – 45%, and (211) – 39%.

It is interesting to note, that the formation of strontium stannate at the same synthetic conditions occurs in a slightly different way. For example, the XRD patterns of $SrSnO_3$ synthesized at 500 ºC and 600 ºC (see *Figure 6.3*) contain additional reflections at $2\theta \approx 25$ º which could be attributed to the $SrCO_3$ impurity phase. However, with increasing the heating temperature up to 700 ºC, these diffraction peaks disappear, possibly, due to the further reaction of $SrCO_3$ with unreacted amorphous SnO_2:

$$SrCO_3 + SnO_2 \rightarrow SrSnO_3 + CO_2\uparrow \qquad \text{(Eq. 6.1)}$$

As seen from *Figure 6.3*, the single-phase perovskite $SrSnO_3$ compound is formed in the temperature range of 700 ºC - 900 ºC using a novel gel to crystallite conversion synthesis method.

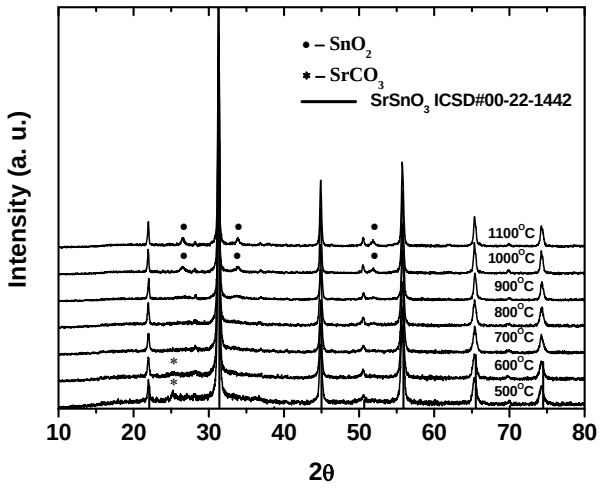

Figure 6.3 *Powder XRD patterns of $SrSnO_3$ samples annealed at different temperatures for 5 h in air.*

According to the literature data, all diffraction lines observed can be assigned to the $SrSnO_3$ phase (ICSD#00-022-1442). The crystallinity of the samples only slightly increases with increasing synthesis temperature. The XRD patterns of $SrSnO_3$ samples annealed at 700 ºC, 800 ºC and 900 ºC already contain very sharp reflections. The most intense lines are (112) – 100%, (312) – 41%, and (220) – 30%. The strontium stannate predominates in the samples synthesized at higher temperatures as well. However, the formation of impurity phases with increasing heating temperature (>900 ºC) in the final materials was again determined. The formation of side SnO_2 phase ($2\theta \approx 26$ º, 34 º and 52 º) is evident from the XRD patterns of $SrSnO_3$ specimens annealed at 1000 ºC and 1100 ºC. Thus, the XRD results clearly showed that monophasic $SrTiO_3$ and $SrSnO_3$ samples have formed in the temperature ranges of 800 ºC - 1000 ºC and 700 ºC - 900 ºC, respectively. Therefore, the lowest temperature (800 ºC) suitable for the formation of both compounds by G-C method has been selected as optimum temperature for the preparation of $SrSn_{1-x}Ti_xO3$ solid solution. *Figure 6.4* shows the

room temperature XRD patterns of ten different $SrSn_{1-x}Ti_xO_3$ (x = 0.05 - 0.5) samples heated at 800 ºC.

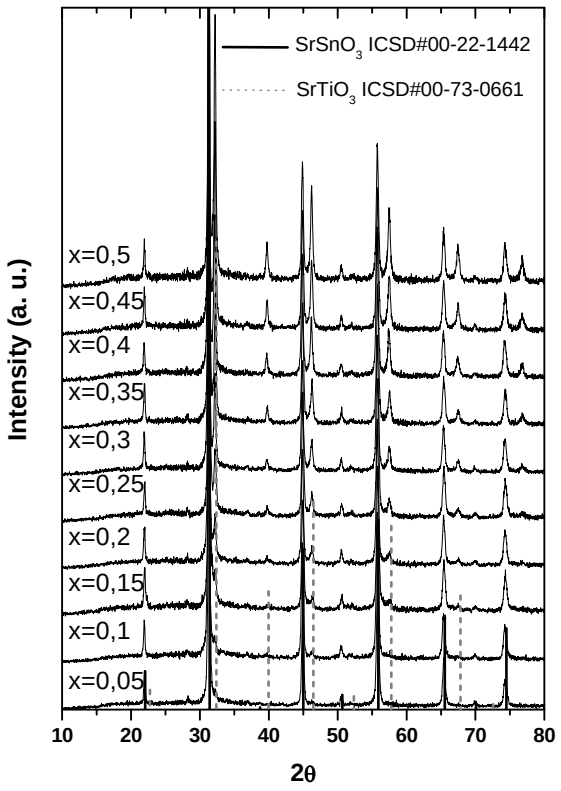

Figure 6.4 *Powder XRD patterns of $SrSn_{1-x}Ti_xO_3$ samples annealed at 800 ºC for 5 h in air.*

Since ionic radii of Ti(IV) and Sn(IV) are rather similar (Sn^{4+} (R = 0.69 Å) and Ti^{4+} (R = 0.61 Å)), we believed that the samples will crystallize into single-phase solid solutions of perovskite structure [120]. However, it seems that the formation of separate phases instead of $SrTiO_3$ - $SrSnO_3$ system occurs [121]. Interestingly, the intensity of characteristic $SrTiO_3$ lines increases with increasing Ti content, however, the intensities of $SrSnO_3$ diffractions remains steady.

The surface morphology features of synthesized $SrTiO_3$, $SrSnO_3$ and $SrSn_{1-x}Ti_xO_3$ samples were estimated using scanning electron microscopy (SEM). The SEM micrographs of $SrTiO_3$ sample synthesized at 800 ºC are shown in *Figure 6.5*. The SEM images indicated that the powder particles consist of agglomerates of 1 – 5 micron in size.

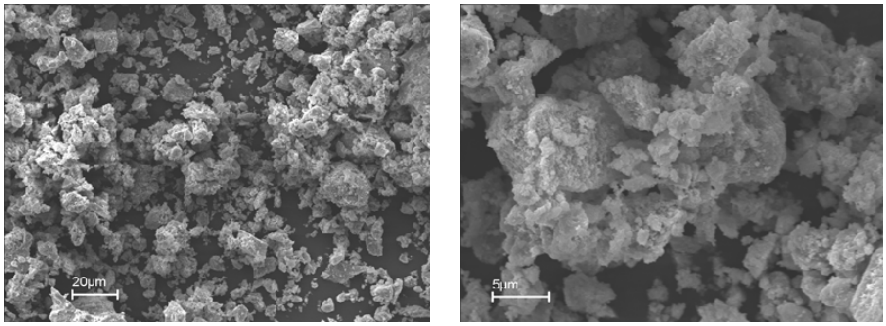

Figure 6.5 *Scanning electron micrographs of $SrTiO_3$ synthesized at 800 ºC.*

However, quite different surface morphology was determined for $SrSnO_3$ samples. The SEM micrographs of $SrSnO_3$ specimens heated at 500, 800 and 1100 ºC are shown in *Figure 6.6, 6.7* and *6.8*, respectively. As seen from *Figure 6.6*, the low temperature synthesis gave nearly rod-stick $SrSnO_3$ particles. However, some $SrSnO_3$ particles are smaller needle-type crystallites. The crystal width and length vary from 500 nm to 3 µm and from 10 to 40 µm, respectively. Moreover, at higher magnification it can apparently be seen, that some rod-type crystals are covered by small spherical particles. These spherical crystallites could be attributed to the impurity $SrCO_3$ phase detected by XRD.

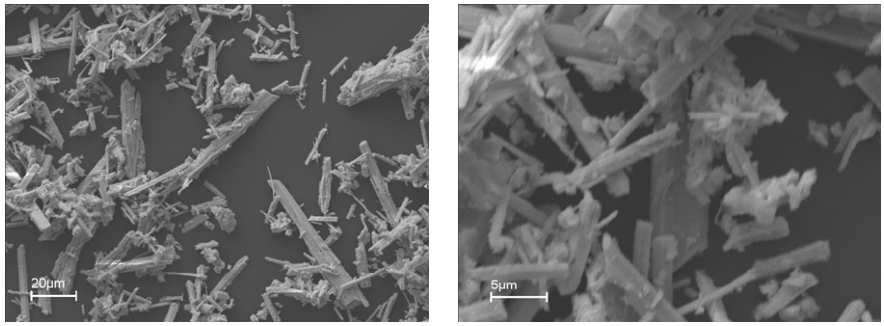

Figure 6.6 *Scanning electron micrographs of $SrSnO_3$ synthesized at 500 ºC.*

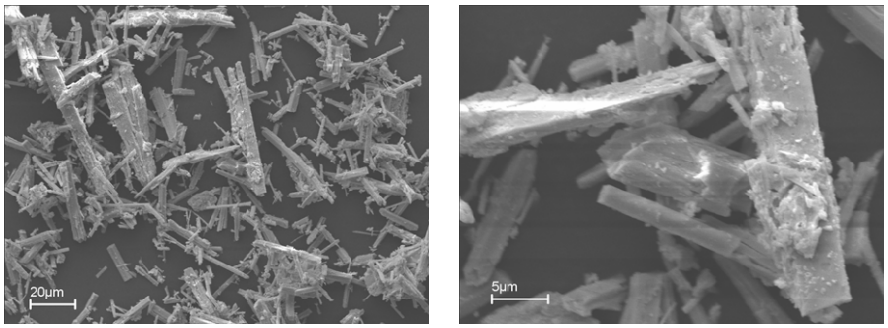

Figure 6.7 *Scanning electron micrographs of $SrSnO_3$ synthesized at 800 ºC.*

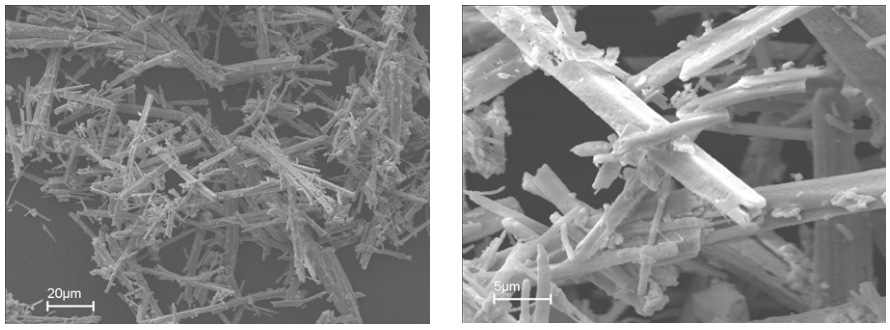

Figure 6.8 *Scanning electron micrographs of $SrSnO_3$ synthesized at 1100 ºC.*

Figure 6.7 presents the SEM micrographs of $SrSnO_3$ powders heated at 800 ºC. The main morphological features of strontium stannate samples prepared at higher temperature remain very similar. The formation of $SrSnO_3$ sticks is clearly seen in both SEM micrographs. On the other hand, no formation of additional spherical particles could be found in these images. These results are in a good agreement the XRD measurements, confirming that monophasic $SrSnO_3$ could be obtained at 800 ºC using gel to crystallite conversion synthetic approach. The annealing of $SrSnO_3$ at 1100 ºC does not change the surface morphology of the mixed-metal oxide (*see Figure 6.8*). The solids are composed of differently orientated rods which have very similar size as prepared at 500 ºC and 800 ºC. Again, some elongated crystallites are covered with small plate-like crystals which could be attributed to impurity SnO_2 phase.

Figure 6.9 shows SEM images of the $SrSn_{1-x}Ti_xO_3$ ceramics (x = 0.15) sintered at 800 ºC for 5 h. As seen, the morphology of $SrSn_{1-x}Ti_xO_3$ is different from those of $SrTiO_3$ and $SrSnO_3$. The material shows a microporous structure and is composed of agglomerated assembles of different fine grains. The reason for this change is the formation of strontium stannate-titanate. For the composition with x = 0.15, it is observed that the grain growth is uniform and the size of the grains is of the order of ~5 μm. However, the small plate-like crystals are also seen in the SEM micrograph presented in *Figure 6.9*. These crystallites could be attributed to separately crystallized negligible amount of strontium titanate.

In conclusion, well grown and homogeneous grain structure [122] can be obtained via proposed novel synthesis method for strontium stannate titanate.

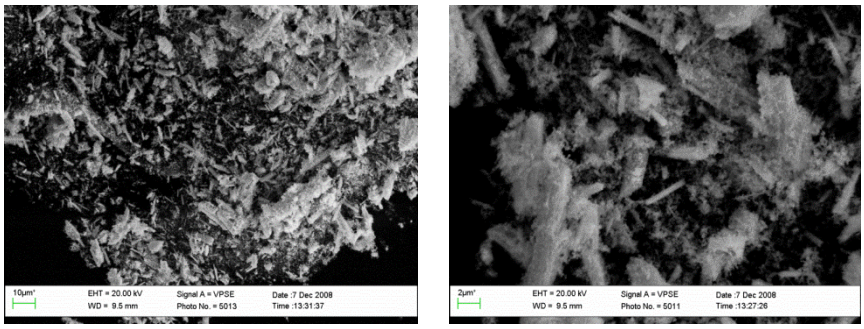

Figure 6.9 *Scanning electron micrographs of* $SrSn_{1-x}Ti_xO_3$ *synthesized at 800 ºC with x = 0.15.*

In conclusion, a simple, inexpensive and environmentally benign 'chimie douce' synthetic approach based on the gel to crystallite conversion (G-C) method have been suggested for the synthesis of strontium stannate $SrSnO_3$ and strontium titanate $SrTiO_3$ powders. However, the G-C synthesis of mixed strontium stannates-titanates $SrSn_{1-x}Ti_xO_3$ (x = 0.05–0.5 mol %) resulted in formation of separate perovskite phases, probably, due to thermodynamic reasons. Interestingly, the morphological features of $SrSnO_3$ and $SrTiO_3$ powders synthesized by the same synthetic procedure were completely different. The proposed synthesis route allows us to prepare monophasic $SrSnO_3$ and $SrTiO_3$ at very mild conditions.

Chapter 7. SnO_2 Thin Films From an Aqueous Citrato Peroxo Sn(IV) Precursor

7.1. TG-DSC, FTIR, HT-XRD, SEM and AFM Analysis

It is known that tin(II) oxalate cannot be dissolved in water, ethanol or organic solvents. In the SnC_2O_4-H_2O system, according to Liu et al. [123], the following chemical equilibrium occurs:

$$SnC_2O_4 \downarrow + n\ H_2O \leftrightarrow (Sn(OH)_n)^{2-n} \downarrow + H_2C_2O_4 + (n-2)\ H^+ \quad \text{(Eq. 7.1)}$$

However, Alcantara *et al.* suggested a procedure to convert SnC_2O_4 into tin dioxide by dissolving tin oxalate powder in 33% hydrogen peroxide at room temperature. The obtained clear solution is smoothly heated under stirring until boiling where parallel to water evaporation a white colloidal product, SnO_2, precipitates [124]. Mailen *et al.* [125] have studied the decomposition reaction of oxalic acid with H_2O_2. The obtained results showed that the decomposition rate of oxalic acid was very slow at temperatures lower than 90 ºC and also depends on the concentration of nitric acid. Previously, Chung *et al.* [126] reported the decomposition kinetics of oxalic acid by hydrogen peroxide in an aqueous solution. It was shown that some H_2O_2 was self-decomposed during the decomposition of oxalic acid and suggested that for the complete decomposition of oxalic acid the molar ratio of hydrogen peroxide to oxalic acid should be more than four. The results on the dissolution of some metallic oxalate precipitates were reported a few years later [127].

Equation 7.2 presents the thermal decomposition of H_2O_2:

$$H_2O_2 \rightarrow H_2O + ½\ O_2 \quad \text{(Eq. 7.2)}$$

Equation 7.3 presents the acid-catalyzed decomposition of H_2O_2:

$$H_2O_2 + H^+ \rightarrow H_2O + ½\ O_2 + H^+ \qquad \text{(Eq. 7.3)}$$

Decomposition of oxalate by hydrogen peroxide could be expressed by (Eq. 7.4):

$$H_2C_2O_4 + H_2O_2 \rightarrow 2CO_2 + 2H_2O \qquad \text{(E1. 7.4)}$$

Finally, the oxidation of Sn(II) by hydrogen peroxide in aqueous solution:

$$H_2O_2 + Sn^{2+} \rightarrow Sn^{4+} + 2OH^- \qquad \text{(Eq. 7.5)}$$

The consumption of hydrogen peroxide according to Eq. 7.5 has not been evaluated by Kim et al. Part of the hydrogen peroxide is used to decompose oxalate, the other for the oxidation of Sn^{2+} to Sn^{4+}.

After reaction of tin(II) oxalate with hydrogen peroxide, α-stannic acid in which hydroxyl groups (OH) are partially replaced with hydroperoxo (OOH) groups was obtained. In a way, hydrogen peroxide acts as a capping agent that prevents full condensation. ^{119}Sn NMR studies have proven that ligand exchange takes place reversibly. The exchange is observable already at 1% hydrogen peroxide, and at ~90% the most dominant dissolved species is $[Sn(OOH)_6]^{2-}$ [128, 129]. Freshly prepared α-stannic acid is soluble in acids and bases. During storage α-stannic acid loses absorbed water and transforms into β-stannic acid which is chemically inert [22]. This is related to a change of active HO-Sn groups with a less active bridging –Sn-O-Sn- bond. For this reason *in-situ* tin-citrate complex formation procedure is applied in this synthesis route to avoid precipitation of unreactive β-stannic acid.

It is crucial to add sufficient hydrogen peroxide in the initial step of processing to fully oxidize Sn(II) according to Eq. 7.5. Otherwise, the formation of the white precipitate occurs at pH~6.5 during neutralization with ammonia, probably due to formation of an unstable Sn(II) complex

with citric acid. In *Table 7.1*, an overview is given of the stability of the citrato peroxo Sn(IV) precursors with different Sn(IV):CA ratios upon pH change after 1 week of storage at room temperature. The major advantage of this route is that oxalate ions are decomposed and removed from solution, making it possible to mix the citrato peroxo Sn(IV) precursor with other metal ions and to avoid precipitation of insoluble oxalates.

Table 7.1 *Stability of different citrato peroxo Sn(IV) precursors.*

Sn(IV):CA ratio	**pH=1-2 No NH_3**	**pH=7 NH_3**	**pH=8 NH_3**
1/1	**S**	**P**	**P**
1/2	**S**	**P**	**P**
1/3	**S**	**S**	**P**
1/4	**S**	**S**	**P**
1/5	**S**	**S**	**P**
1/6	**S**	**S**	**S**

P, precipitation within 1 week; **S**, clear, stable solution for at least 1 week.

TG-DSC data for tin(II) oxalate powders and dried intermediate species of hydrated tin(IV) oxide are shown in *Figure 7.1*. The TG curve of tin(II) oxalate encounters an abrupt weight loss in a narrow temperature region peaked at 369 ºC (*Figure 7.1a*). The intense exothermic peak observed on the DSC curve could be assigned to the decomposition of SnC_2O_4, expressed by following reaction [124]:

$$SnC_2O_4 + Q \rightarrow SnO_2 + 2\ CO \qquad \text{(Eq. 7.6)}$$

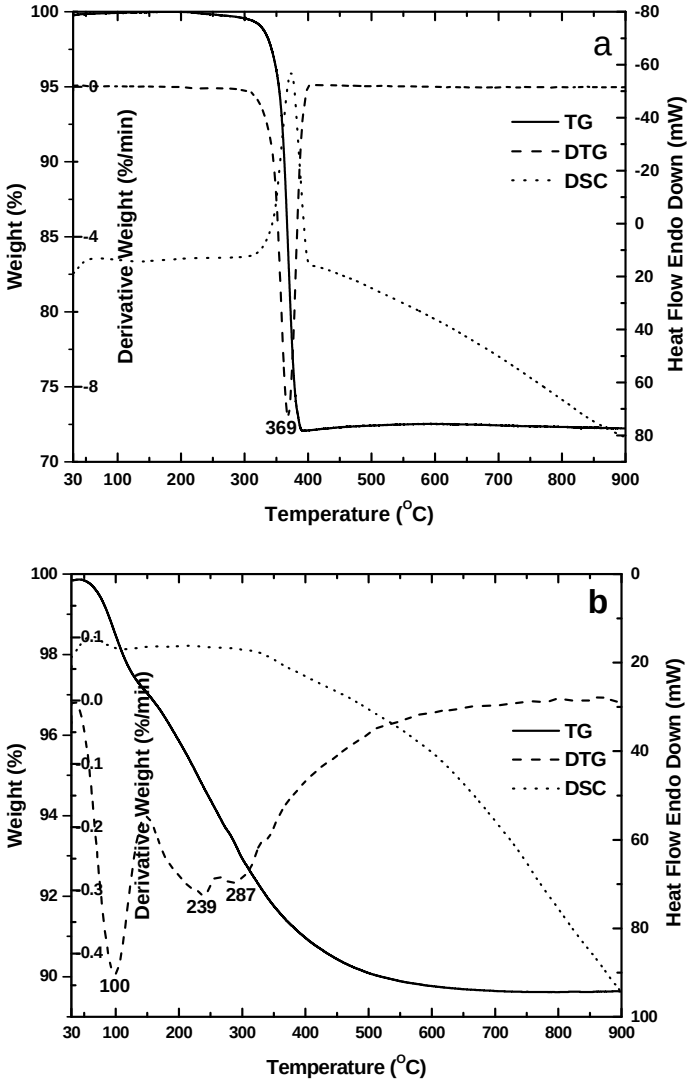

Figure 7.1 *TG/DTG and DSC curves of (a) SnC_2O_4 and (b) $SnO_2 \cdot xH_2O$ in a dry flowing air (20 mL/min).*

Two main weight loss events are observed in hydrated tin(IV) dioxide. Below 150 ºC the dehydration and above this temperature dehydroxylation processes take place (*Figure 7.1b*). During the first stage, the adsorbed water is removed, during the second thermolysis stage, the dehydration of the compound occurs mostly via the polycondensation of terminal ≡Sn–OH

groups [130]. The absence of exothermic peaks corresponding to the decomposition of oxalates in the DSC curve of hydrated tin dioxide sample proves that stannic acid is oxalate-free after the reaction with hydrogen peroxide. The thermal decomposition of the citrato peroxo Sn(IV) precursor gel was carried out in order to display thermal decomposition steps, which is used as a basis for choosing hot plate treatment (*Figure 7.2*). As seen from the DTG profile, the highest decomposition rate is observed at 235 ºC, corresponding to the decomposition of the excess of ammonium citrate [131].

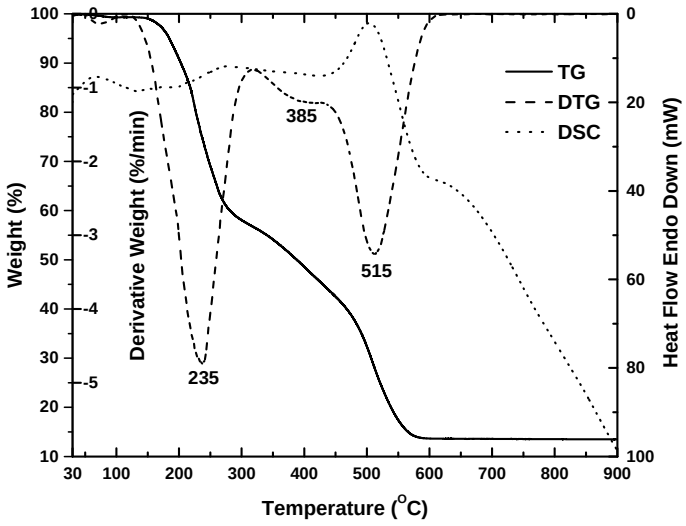

Figure 7.2 *TG/DTG and DSC curves of a citrato peroxo Sn(IV) precursor gel (CA:Sn(IV) 6:1).*

The pyrolysis of the coordination compound occurs at 385 ºC. According to the general decomposition scheme of aqueous citrato peroxo gels, organic rest fractions are decomposed at 515 ºC. These rest fractions are formed from the decomposition of excess ammonium citrate and consist of nitrogen containing organic compounds with a high thermal stability [132]. A larger

amount of organic material in the CA:Sn(IV) 6:1 gel leads to a lower final weight percentage after complete decomposition (13.5%). No more weight losses are observed above 550 ºC, indicating that all organic residues are decomposed at this point. For that reason this temperature was chosen as the final calcination temperature for the films.

The FTIR spectrum of tin oxalate is shown in *Figure 7.3a*. The characteristic absorption bands of C-O stretching could be identified as two doublets at 1596-1674 and 1297-1342 cm^{-1} and can be assigned to the asymmetric and symmetric O=C-O stretching, respectively [133]. A narrow and intense signal at 790 cm^{-1} is typical for O-C=O deformational vibrations. Two peaks observed at 480 and 428 cm^{-1} could be attributable to the ring deformation and Sn-O stretching. These FTIR results are in a good agreement with data published elsewhere [134]. The infrared spectrum of stannic acid (*Figure 7.3b*) shows a strong absorption in the range of 3700–2800 cm^{-1} due to O–H stretching modes of H-bonded hydroxyl groups, ν(OH). In the 1700-1500 cm^{-1} region a strong composite band, which is formed by the superposition of the δ(SnOSn) 1706 cm^{-1} and δ(H_2O) 1637 cm^{-1} band could be observed. Two bands at 1390 cm^{-1} and 1245 cm^{-1} are due to 2ν(OSnO) and terminal δ(SnOH) vibrations, respectively [130]. In the 800-400 cm^{-1} region, a broad and strong absorption band due to the ν(SnO) vibrations in the SnO_6 octahedron is present. The fact that a very strong signal at 790 cm^{-1} is absent in *Figure 7.3b*, earlier assigned to δ(O-C-O) + ν(C-C) vibrations, confirms that stannic acid does not contain any traces of oxalate ions.

Thermal treatment causes a number of changes in the FTIR spectrum of stannic acid. Namely, the wide band in the range of 3700–2800 cm^{-1}

disappears upon heating the sample up to 800 ºC. This observation suggests the evident changes in the structure of hydrated oxide by dehydroxylation. The FTIR spectrum of tin(IV) oxide (*Figure 7.3c*) shows two symmetry allowed Sn-O stretching bands of rutile-type crystalline SnO_2 (D_{4h}, E_u *xy*-plane and A_{2u} *z*-axis modes) located at 618 and 477 cm^{-1}, respectively [124].

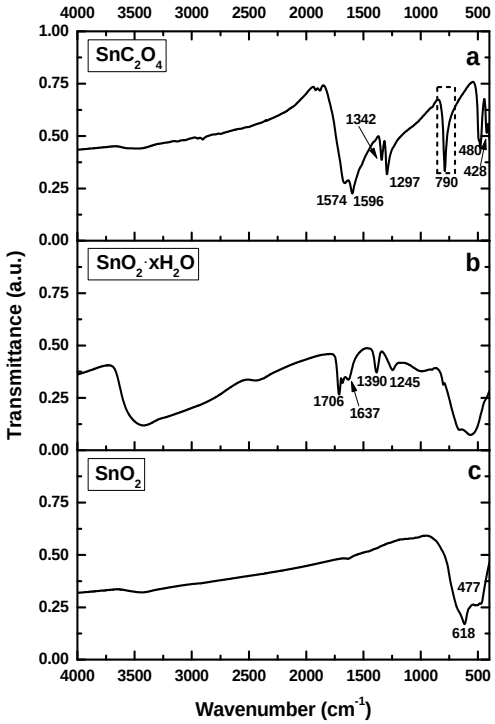

Figure 7.3 *FTIR spectra of (a) tin(II) oxalate; (b) hydrated tin(IV) oxide and (c) tin(IV) oxide.*

All the powder characterization served to understand the synthesis and assure that it is possible to obtain phase pure SnO_2 from this precursor. Based on these insights, the precursor can be regarded as a reliable source for tin oxide film deposition. Indeed, phase formation of spin coated SnO_2 thin films was confirmed by high temperature X-ray diffraction. The XRD

patterns of 1-5 layered films contained only very weak and broad characteristic diffraction peaks. With increase of the film thickness, the intensity and sharpness of diffraction peaks of (1 1 0), (1 0 1), (2 0 0) and (2 1 1) gradually increased. *Figure 7.4* shows the HT-XRD patterns of a 10 layered SnO_2 film annealed at 550 ºC in dry air. As seen from *Figure 7.4*, all diffraction lines of sol-gel derived films correspond to monophasic SnO_2 (cassiterite). *Figure 7.5* shows the HT-XRD patterns of 10 layered SnO_2 films as a function of in-situ measurement. Evidently, the sol-gel derived SnO_2 films are already crystalline after the last hot plate step (400 ºC), but still contain residual organics, as seen from the TGA profile (*Figure 7.2*). Moreover, the intensity of characteristic peaks increases with increasing the temperature from 400 to 1000 ºC.

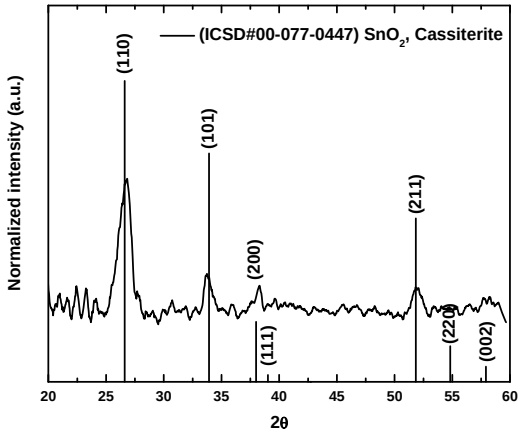

Figure 7.4 *HT-XRD pattern of a 10 layered SnO_2 film annealed at 550 ºC in dry air. Film deposited from citrato peroxo Sn(IV) precursor (pH=7; c(Sn(IV))=0.2 M).*

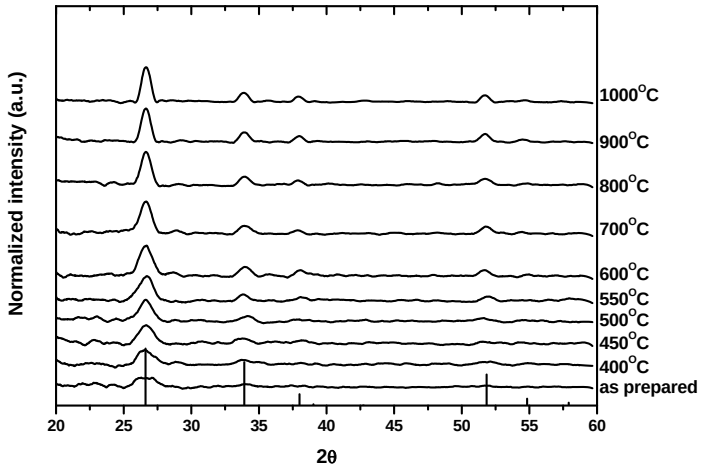

Figure 7.5 *HT-XRD patterns of a 10 layered SnO_2 film derived from citrato peroxo Sn(IV) precursor (pH=7; c(Sn(IV))=0.2 M). Vertical lines belong to the ICSD#00-077-0447 of SnO_2.*

Cross-section SEM images of differently layered SnO_2 thin films derived from the citrato peroxo Sn(IV) precursor are shown in *Figure 7.6*. The SEM micrographs clearly show the formation of a dense film. The desired SnO_2 film thickness can be achieved by applying a certain number of spin coating cycles and/or by varying the starting precursor concentration. The single layer thickness was determined to be in a range of 16 and 17 nm for each deposition step using the 0.2 M precursor solution. A linear relation between the thickness of the SnO_2 films and the number of deposited layers was observed (inset *Figure 7.6*).

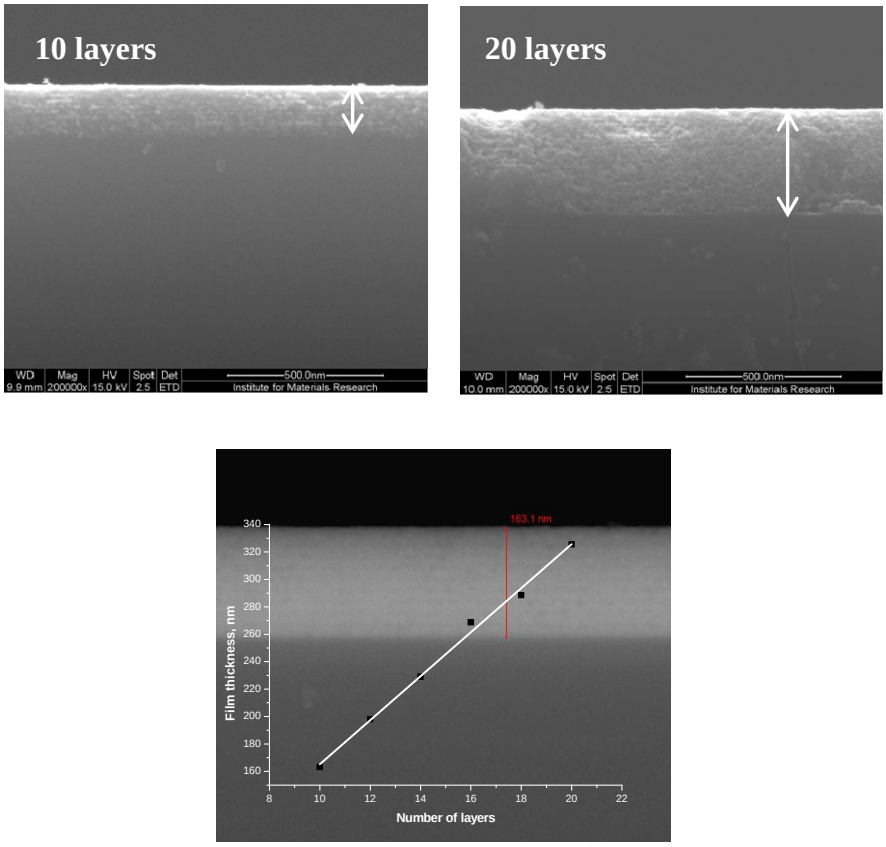

Figure 7.6 *Cross-section SEM images of SnO_2 thin films. Inset: film thickness vs. number of layers.*

Plane view SEM images of the microstructure of the obtained SnO_2 films are shown in *Figure 7.7*. As can be observed, a smooth, uniform and small grained microstructure without porous areas or cracks is obtained. Evidently, the scanning electron micrographs indicate the formation of spherical nanometer size grains (~20-40 nm in size). The crystallites are necked to each other forming highly symmetric ornaments. The particles of SnO_2 formed with very well pronounced agglomeration, indicating a good connectivity between the grains.

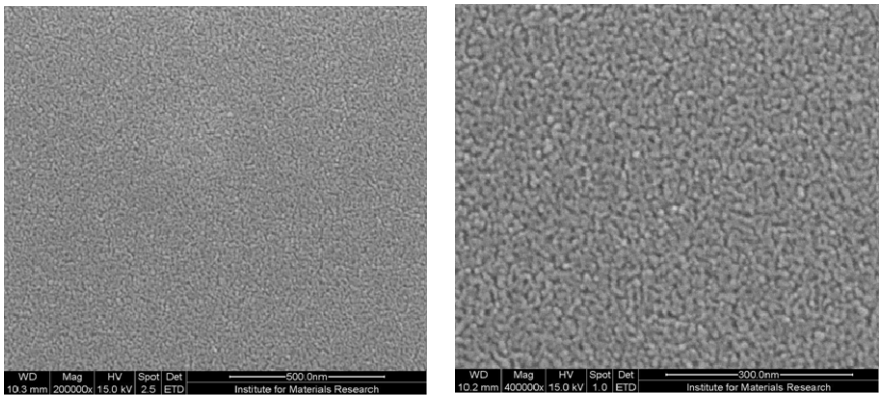

Figure 7.7 *SEM micrographs of a 10 layered SnO_2 film with different magnifications.*

The AFM micrograph of a 10 layered SnO_2 film is shown in *Figure 7.8*. The RMS roughness of the film was found to be around 4.5 nm.

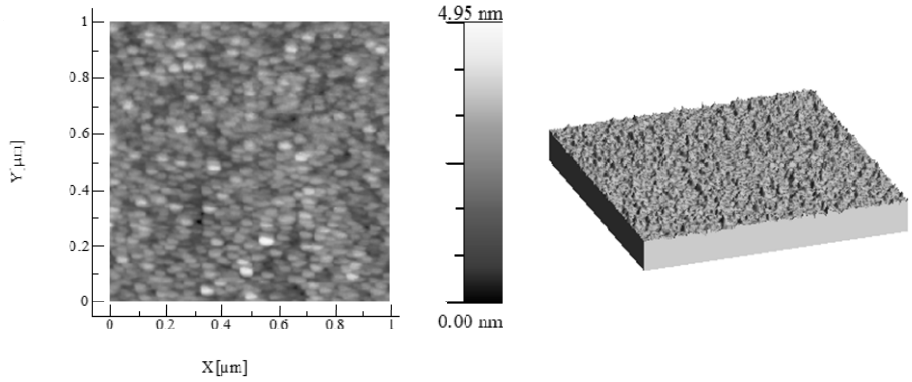

Figure 7.8 *2D and 3D AFM image of a 10 layered SnO_2 film. RMS roughness: 4.5 nm.*

In this chapter, a novel and inexpensive water based synthesis route for the preparation of a chloride-free citrato peroxo Sn(IV) precursor solution

was developed and systematically investigated. The gel precursor was successfully applied for the preparation of cassiterite-type crystalline SnO_2 thin films on a Si/SiO_2 substrate at 400 ºC. The selectivity of SnO_2-based sensors depends very much on the thickness and the porosity of the film. Becker et al. [135] demonstrated that at normal sensor operation temperatures around 400 ºC thin-film (d ~ 50-300 nm) devices mainly respond to oxidising gases such as O_3 and NO_2, whereas thick-film (d ~ 15-80 μm) ones preferably respond to reducing species like CO and CH_4. In compact layers the interaction with gases takes place only at the geometric surface, while in porous layers the volume of the layer is also accessible to the gases and the active surface is higher than in geometric one [136]. The proposed CSD procedure let us to deposit compact layers with controllable thickness of the film.

Chapter 8. Sol-gel (Combustion) Synthesis and Characterization of Different Alkaline Earth Metal (Ca, Sr, Ba) Stannates

8.1. TG-DSC, XRD and SEM Analysis

The thermal behaviour of Ca-Sn, Sr-Sn and Ba-Sn precursor gels was investigated by TG-DSC measurements (*Figure 8.1*). The TG-DSC curves of Sr-Sn (1:1) precursor gel prepared using strontium hydroxide as starting material are shown in *Figure 8.1a*.

The TG curve reveals that the mass loss occurs in four steps. The first weight loss (about 3%) observed in the TG curve from 25 to ~200 °C and peaked at 100 °C in the differential thermogravimetric (DTG) curve is due to the loss of residual water in the precursor gel. The second weight loss (~27%) between 200 and ~285 °C and peaked at around 228 °C can be ascribed to the decomposition of ammonium citrate network. The main weight loss (~30%) is observed in the temperature range of 285-510 °C and can be assigned to the pyrolysis of coordination compounds and organic part of the gels. Finally, weight abruptly decreases in very narrow temperature interval (510-600 °C). This weight loss in the TG curve (28%) is accompanied by the strongest exothermic signal in DSC curve peaked at 553 °C. It is associated with the burnout of rest fractions consisting of thermally stable amides and imides [131]. The total weight loss of the sample according to the TG curve is 88%, while the ceramic yield is 12%. Interestingly, the thermal behaviour of Ba-Sn (1:1, hydroxide based) precursor gel (not included) is similar to the Sr-Sn (1:1, hydroxide based) precursor gel presented in *Figure 8.1a*. These results clearly indicate the same origin of both specimens.

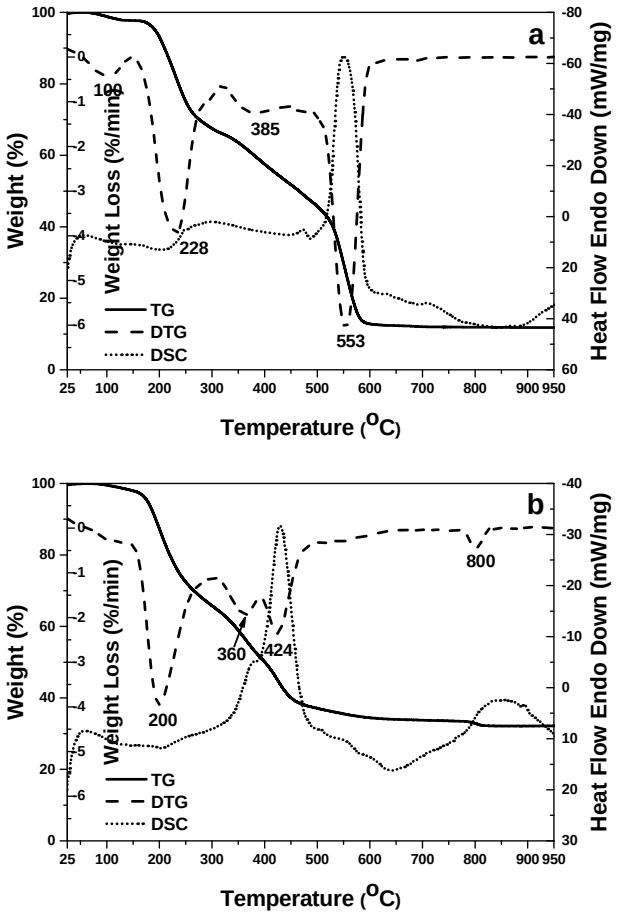

Figure 8.1 *TG-DSC curves of (a) Sr-Sn (1:1, hydroxide based) and (b) Ca-Sn (1:1, nitrate based) precursor gels.*

A different thermal degradation behavior can be observed for Ca-Sn (1:1, nitrate based) precursor gel, obtained after the combustion process. The TG-DSC curves of Ca-Sn (1:1) precursor gel prepared using strontium nitrate as starting material are shown in *Figure 8.1b*. The decomposition of Ca-Sn (1:1, nitrate based) precursor gel again occurs in four stages. The first weight loss (about 3%) observed in the TG curve from 25 to ~200 °C is due to the loss of residual water in the precursor gel. The second weight loss

(~27%) between 200 and ~285 °C and third one between 285 and 450 °C (~35%) are hardly distinguishable. As seen from the DTG profile, the highest decomposition rate is observed at 200 °C corresponding to decomposition of citric acid. The second exothermic weight loss (424 °C) can be associated with the combustion reaction of residual starting citric acid and nitrate ions. In this system the citrate ions act as a fuel (reductant) and nitrate ions act as oxidant. Therefore, the presence of nitrate ions leads to lower decomposition temperatures of citric acid if compared to the system without nitrate ions. This observation is in a good agreement with the results reported by Li *et al.* [137]. The last weight loss of ~2% occurring at 800 °C is attributed to the decomposition of calcium carbonate traces present in the sample. It is obvious that the ceramic yield is higher (32%) in the case of Ca-Sn precursor gel. The observed lower weight loss after complete decomposition of Ca-Sn precursor gel at 900 °C is due the smaller amount of citric acid used in the sol-gel processing and absence of ammonia.

The phase crystallinity and purity of all samples were characterized by means of XRD analysis.

Figure 8.2 shows XRD patterns of sol-gel derived (neutral conditions) strontium and barium meta-stannates ($SrSnO_3$, $BaSnO_3$) and ortho-stannates (Sr_2SnO_4, Ba_2SnO_4). The XRD patterns of strontium meta-stannate and ortho-stannate powders obtained using strontium hydroxide as strontium source in the sol-gel process are presented in *Figure 8.2a-c*. All the peaks in $SrSnO_3$ pattern (*Figure 8.2a*) could be indexed to orthorhombic perovskite structure (ICDD#04-010-2598). The broad reflections in XRD profile of Sr_2SnO_4 powders calcined at 800 °C suggest that crystallization is not complete (*Figure 8.2b*). Moreover X-ray reflections arising from byproducts

such as $SrSnO_3$ or $SrCO_3$ are present in Sr_2SnO_4 sample annealed at 800 °C. The XRD pattern at 1000 °C (*Figure 8.2c*) clearly indicates the formation of single-phase Sr_2SnO_4 (ICDD#04-014-2819) powders with tetragonal K_2NiF_4-type structure.

The XRD pattern of barium meta-stannate sample is illustrated in *Figure 8.2d*. All the diffraction peaks are indexed to the cubic perovskite phase of $BaSnO_3$ (ICDD#04-015-0523). It is interesting to note that barium ortho-stannate sample, prepared under the same synthetic conditions as strontium ortho-stannate, undergoes different phase evolution processes at 800 °C. Two dominant intermediate products of $BaSnO_3$ and $BaCO_3$, with traces of desirable ortho-stannate phase (the most intensive line at $2\theta \approx 29.5°$), can be seen in the XRD pattern of Ba_2SnO_4 specimen annealed at 800 °C (*Figure 8.2e*). However, these intermediate phases are converted to a more stable Ba_2SnO_4 phase at higher temperature. As shown in *Figure 8.2f*, the single phase Ba_2SnO_4 sample (ICSD#00-074-1349) was obtained after heating the Ba-Sn precursor gel at 1000 °C.

The use of strontium and barium acetates as a source of Sr and Ba, respectively, did not affect phase purity and composition of meta-stannate powders, but led to the higher amount of carbonate impurities in ortho-stannate powders, which remained even after thermal treatment at 1000 °C (not included).

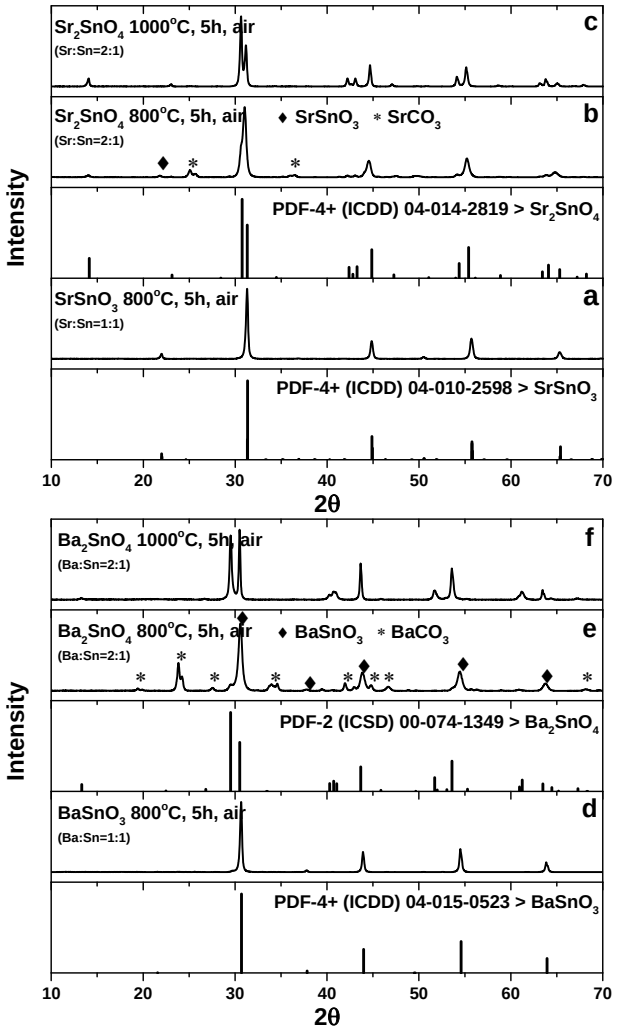

Figure 8.2 *XRD patterns of metal stannates prepared by sol-gel method and annealed at different temperatures: (a) $SrSnO_3$ at 800 °C; (b) Sr_2SnO_4 at 800 °C; (c) Sr_2SnO_4 at 1000 °C; (d) $BaSnO_3$ at 800 °C; (e) Ba_2SnO_4 at 800 °C and (f) Ba_2SnO_4 at 1000 °C, starting from corresponding metal hydroxides.*

The representative XRD patterns of calcium meta- and ortho-stannates synthesized via sol-gel combustion technique (acidic media) are shown in *Figure 8.3*. All peak positions for $CaSnO_3$ compound match very well the

standard XRD data of ICDD#04-015-3326 (*Figure 8.3a*). In the diffraction pattern of Ca_2SnO_4 specimen heated at 800 °C the reflection from the (101) plane is assigned to small portion of orthorombically distorted $CaSnO_3$ phase (*Figure 8.3b*). This minor impurity totally disappeared in the powders calcined at 1000 °C leading to the formation of monophasic Ca_2SnO_4. The strong and sharp reflection peaks observed in *Figure 8.3c* suggest that Ca_2SnO_4 powders are highly crystalline.

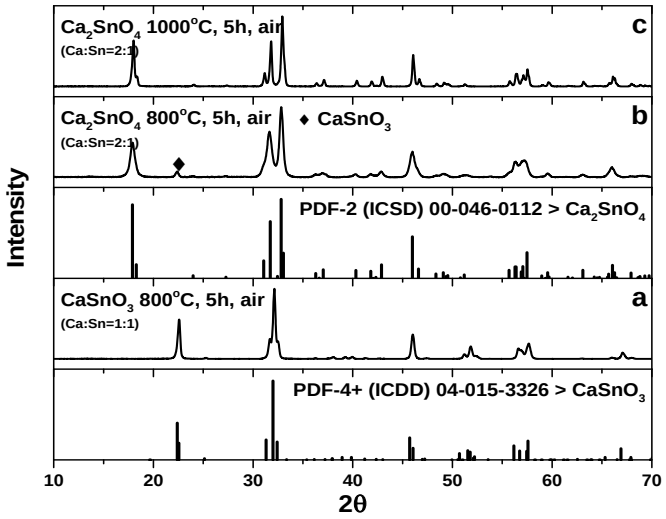

Figure 8.3 *XRD patterns of (a) $CaSnO_3$ and (b, c) Ca_2SnO_4 samples prepared by sol-gel combustion method, starting from calcium nitrate, as a function of annealing temperature.*

When sol-gel combustion process using acidic media was applied for the preparation of strontium and barium stannates white precipitation occurred during evaporation of the solvent. This resulted in the formation of non-homogeneous gels with visible phase segregation. The XRD patterns presented in *Figure 8.4* illustrate clearly that neither meta-stannate nor ortho-stannate single phase strontium and barium compounds were obtained after thermal treatment at 800 °C and 1000 °C, respectively.

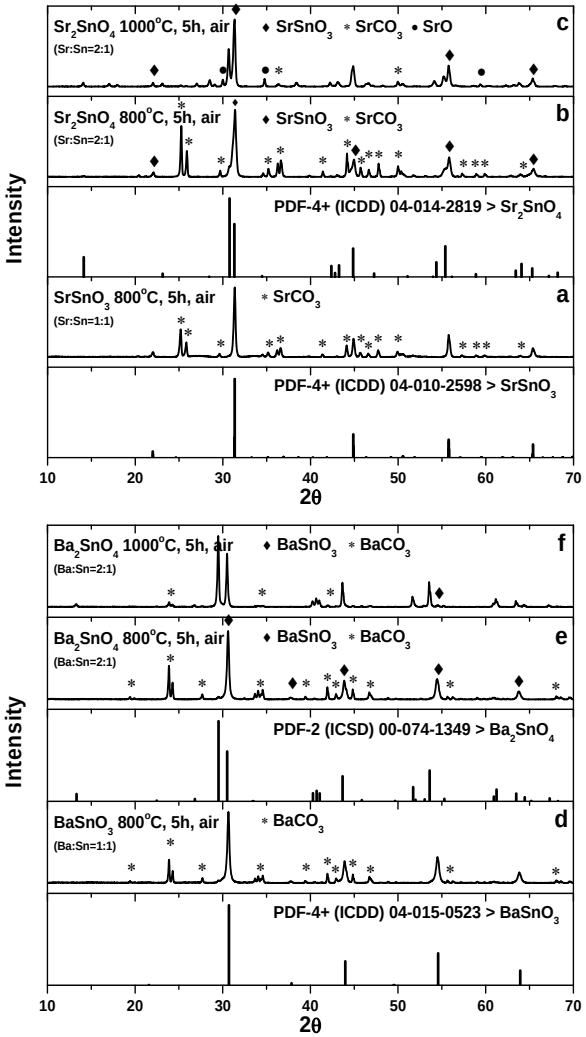

Figure 8.4 *XRD patterns of (a) $SrSnO_3$; (b, c) Sr_2SnO_4; (d) $BaSnO_3$ and (e, f) Ba_2SnO_4 samples prepared by sol-gel combustion method, starting from corresponding metal nitrates, as a function of annealing temperature.*

Based on the obtained XRD results we can conclude that the phase formation mechanism of strontium and barium meta-stannates or ortho-stannates is similar to the traditional solid state reaction synthesis route,

where much higher temperatures are necessary to obtain single phase compound (~1200 °C and ~1400 °C for meta-stannate and ortho-stannate powders, respectively).

The SEM images of different strontium, barium and calcium stannates are shown in *Figure 8.5, 8.6* and *8.7*, respectively. *Figure 8.5a* demonstrates that $SrSnO_3$ powders consist of continuously and parallelly oriented plate-like crystals, while Sr_2SnO_4 powders exhibit extensively necked particles (*Figure 8.5c* and *8.5e*).

The differences in microstructure of strontium ortho-stannate samples annealed at 800 °C and 1000 °C can be observed in the SEM micrographs obtained at higher magnification (*Figure 8.5d* and *8.5f*, respectively). The particles with well-defined crystalline structure can be determined for the Sr_2SnO_4 powders calcined at 1000 °C in comparison to those annealed at 800 °C. Annealing of Sr_2SnO_4 powders at elevated temperature evidently leads to the formation of clear grain boundaries and rod like crystallites within nanometer size range [138]. The Sr_2SnO_4 sample consists of highly agglomerated rod like particles with a mean edge length of ~150 nm, in addition to some spherical aggregations assembled by smaller particulates.

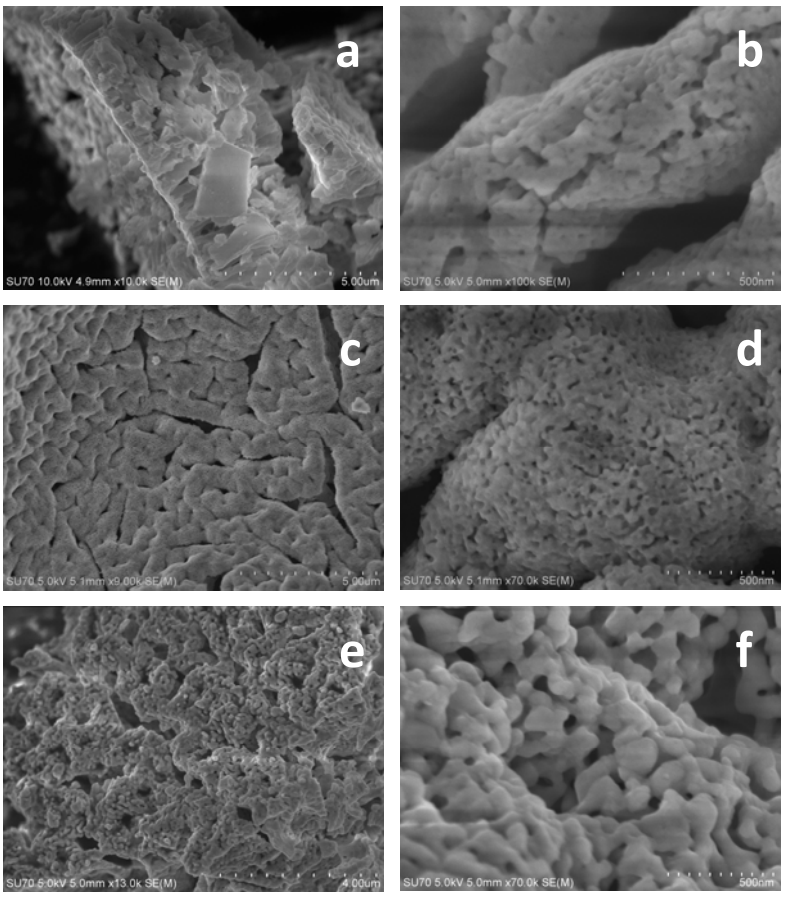

Figure 8.5 *SEM micrographs obtained at different magnifications of (a, b) $SrSnO_3$ powders calcined at 800 °C and Sr_2SnO_4 powders calcined at (c, d) 800 °C and (e, f) 1000 °C for 5 h in air.*

SEM micrographs of $BaSnO_3$ powder show the formation of agglomerates of nano-particles with polyhedral geometry (see *Figure 8.6a, b*). The average grain size was estimated to be ~50 nm. The SEM micrographs shown in *Figure 8.6c, d* clearly demonstrate that undefined shape aggregates covered by small spherical particles are present in Ba_2SnO_4 sample synthesized at 800 °C. These spherical particles could be attributed to the impurity $BaCO_3$ phase detected by XRD analysis. However, the microstructural features of Ba_2SnO_4 powders obtained at

1000 °C have changed considerably. After calcination at higher temperature the coalescence of small elongated rectangular and plate-like crystallites of Ba_2SnO_4 is evident (see *Figure 8.6e, f*).

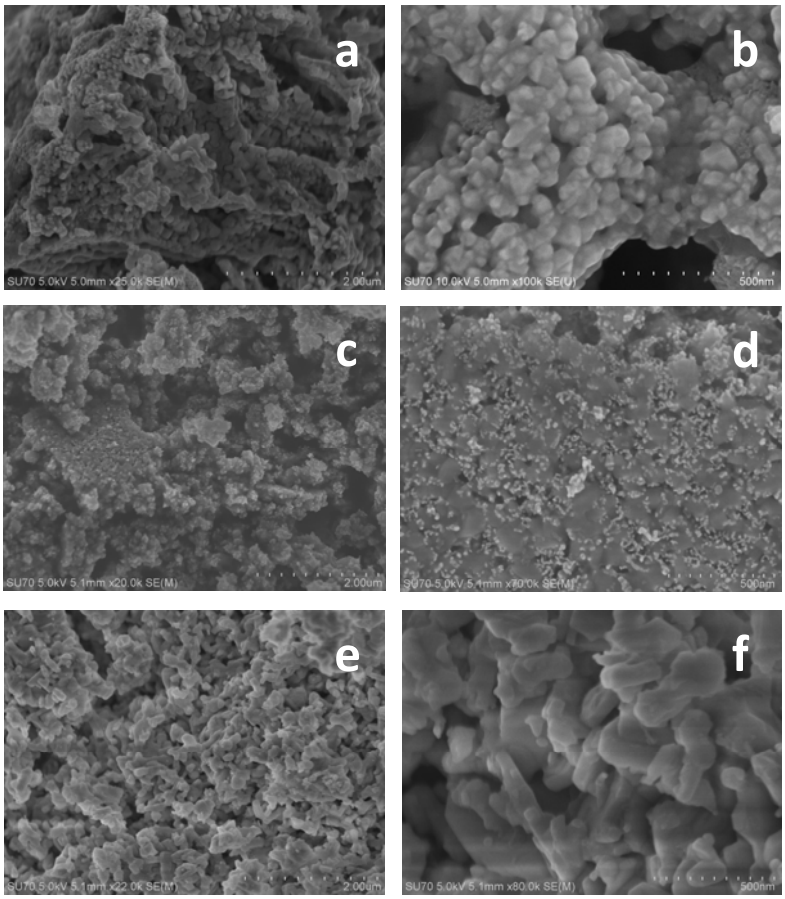

Figure 8.6 *SEM micrographs obtained at different magnifications of (a, b) $BaSnO_3$ powders calcined at 800 °C and Ba_2SnO_4 powders calcined at (c, d) 800 °C and (e, f) 1000 °C for 5 h in air.*

Figure 8.7a, b shows the SEM microstructural images of $CaSnO_3$ powders derived from sol-gel combustion reaction route. As seen, the

microstructure has a high degree of porosity and consists of well-connected spherical grains. The formation of continuous porous network is possibly due to the sudden release of a large amount of gases during combustion process [139].

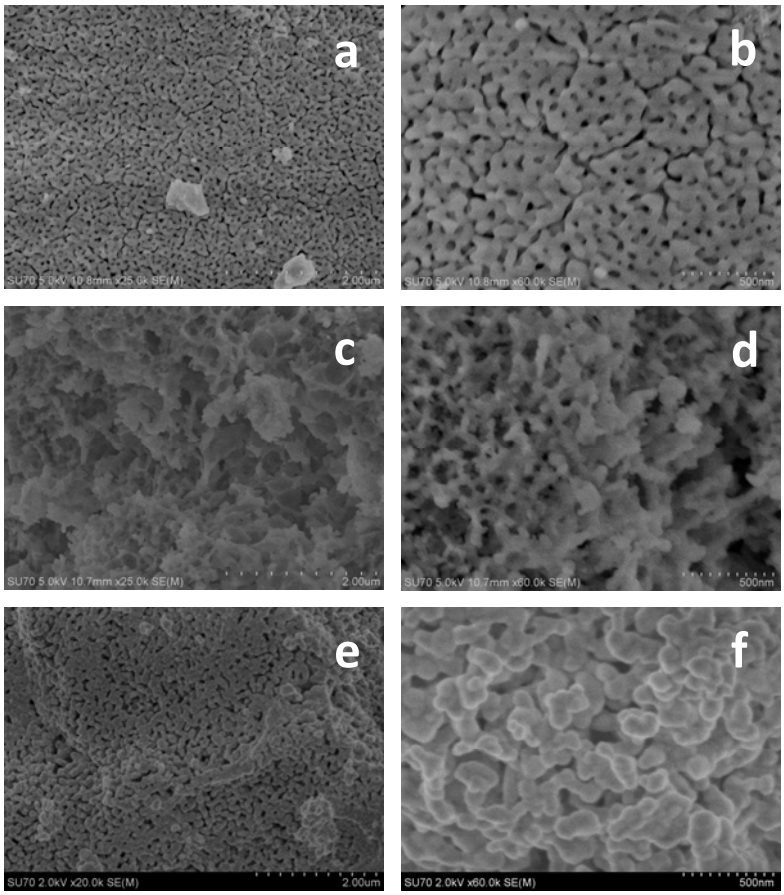

Figure 8.7 *SEM micrographs obtained at different magnifications of (a, b) $CaSnO_3$ powders calcined at 800 °C and Ca_2SnO_4 powders calcined at (c, d) 800 °C and (e, f) 1000 °C for 5 h in air.*

The SEM micrographs presented in *Figure 8.7c, d* demonstrate that undefined shape aggregates have formed also during the synthesis of Ca_2SnO_4 sample at lower temperature (800 °C). The morphology of

Ca_2SnO_4 powders calcined at 1000 °C is shown in *Figure 8.7e, f*. It is evident that grains are nearly spherical and bigger (~50-100 nm) in comparison with $CaSnO_3$.

It is interesting to note, that the SEM micrographs of the synthesized compounds presented in *Figures 8.5-8.7* sufficiently differ from each other revealing that the surface morphology of different calcium, strontium and barium stannates is dependent on the chemical composition. This observation is in a good agreement with previously published results [140].

We have demonstrated, that citrato peroxo Sn(IV) precursor can be successfully applied for the preparation of alkaline earth stannates powders. The thermal treatment revealed that single phase meta-stannates and ortho-stannates can be obtained at 800 °C and 1000 °C, respectively. It was established, that synthesis of strontium and barium stannates requires neutral conditions. However, the successful synthesis of calcium stannates powder should be carried out at acidic conditions. The morphology of synthesized $CaSnO_3$ and Ca_2SnO_4 powders by sol-gel combustion method showed nano-sized and highly porous structures. These morphological features may have potential application as high capacity anode material for Li-ion batteries [141].

Chapter 9. Luminescence of Sm^{3+} in Ca_2SnO_4, Sr_2SnO_4 and Ba_2SnO_4

9.1. XRD Data Analysis

The powder XRD patterns of Ca_2SnO_4:Sm^{3+} samples annealed at 1400 °C for 10 h in air are given in *Figure 9.1*. All the peaks can be indexed to the orthorhombic Ca_2SnO_4 system and are in a good agreement with standard powder XRD data of ICDD#04-008-2918. A minor impurity phase of $CaSnO_3$ is present in all samples as well as in undoped host material. This result is consistent with the previous reports [142, 143].

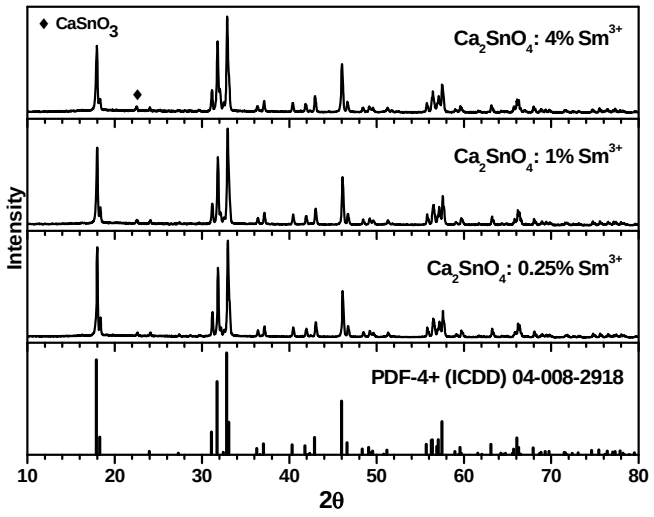

Figure 9.1 *Powder XRD patterns of Ca_2SnO_4:Sm^{3+}.*

Figure 9.2 shows the powder XRD patterns of Sr_2SnO_4:Sm^{3+}. The doping of Sm^{3+} does not make any noticeable changes in the XRD patterns and all the reflection peaks can be assigned to a single phase Sr_2SnO_4 (ICDD#04-010-4448). The absence of impurity phases indicates that the trivalent samarium ions are well incorporated into the crystal lattice.

Powder XRD analysis revealed that single phase $Ba_2SnO_4:Sm^{3+}$ phosphor can be obtained once the samarium content is higher than 2 mol % (*Figure 9.3*). Furthermore, a small amount of $Ba_2SmSnO_{5.5}$ (ICDD#04-002-8282) impurity phase is observed if the dopant concentration exceeds 4 mol %.

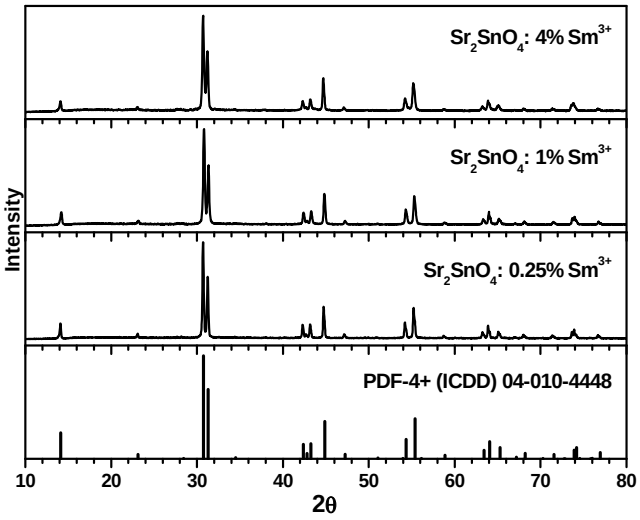

Figure 9.2 *Powder XRD patterns of* $Sr_2SnO_4:Sm^{3+}$.

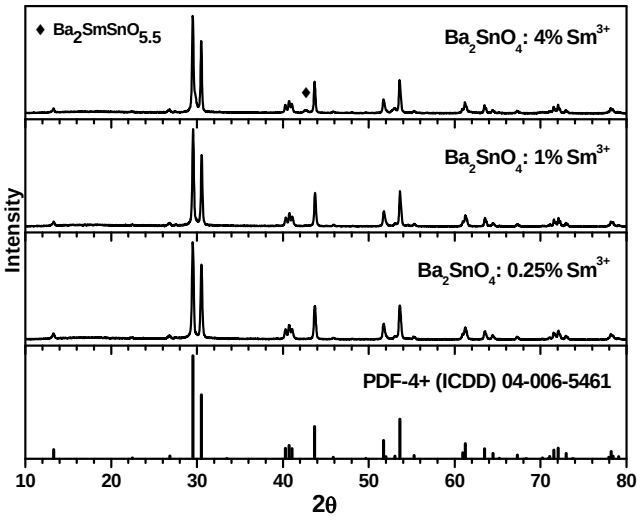

Figure 9.3 *Powder XRD patterns of $Ba_2SnO_4:Sm^{3+}$.*

9.2. Optical Properties

The photoluminescence spectra of Ca_2SnO_4:1% Sm^{3+}, Sr_2SnO_4:1% Sm^{3+}, and Ba_2SnO_4:2% Sm^{3+} are depicted in *Figure 9.4a, b* and *c*, respectively.

The excitation spectrum of Sm^{3+} doped Ca_2SnO_4 sample was recorded by monitoring the emission at 610 nm (*Figure 9.4a*). The strongest excitation band is located at 408 nm ($^6H_{5/2} \rightarrow {}^4L_{13/2}+{}^6P_{3/2}+{}^4F_{7/2}$) and some peaks at 346 nm ($^6P_{7/2}$), 362 nm ($^5D_{3/2}+{}^4F_{9/2}+{}^6P_{5/2}$), 378 nm ($^6P_{7/2}+{}^4K_{13/2}$), 416 nm ($^6P_{5/2}$), 477 nm ($^4I_{9/2}+{}^4M_{15/2}$) are ascribed to the electronic transitions from the ground state to the high energy excited levels of Sm^{3+}.

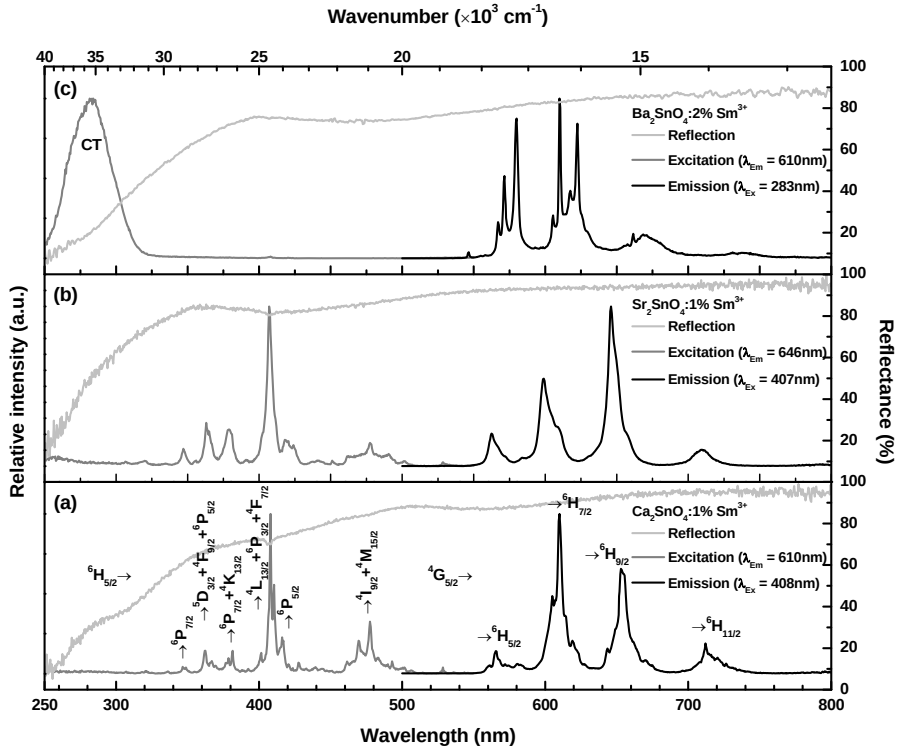

Figure 9.4 *Excitation, emission and reflection spectra of (a) Ca_2SnO_4:1% Sm^{3+} (b) Sr_2SnO_4:1% Sm^{3+} and (c) Ba_2SnO_4:2% Sm^{3+}.*

The strongest emission peaks at 616 nm and 646 nm originate from the well-known intra-4f-shell transitions of Sm^{3+} from the excited state $^4G_{5/2}$ to ground state levels ^6H_J (J=5/2, 7/2, 9/2, 11/2). The given excitation spectra of Sr_2SnO_4:1% Sm^{3+} phosphor (*Figure 9.4b*) is rather similar to Ca_2SnO_4:1% Sm^{3+}. However, the most intensive emission band of Sr_2SnO_4:1% Sm^{3+}phosphor is located at 646 nm and corresponds to the $^4G_{5/2}$ → $^6H_{9/2}$ transition. The excitation spectra of Ba_2SnO_4 sample doped with 2% Sm^{3+} as monitored at 610 nm is depicted in *Figure 9.4c*. The dominating broad band centering at 283 nm can be attributed to the charge transfer (CT) transition from the O^{2-} ligand to the Sm^{3+} and/or Sn^{4+}, whereas direct $4f^5$-$4f^5$

transitions of Sm^{3+} are very weak and barely visible. In accordance to what we say, in calcium and strontium ortho-stannates Sm^{3+} ions are located on the Ca^{2+} and Sr^{2+} sites, respectively. Only in the Ba_2SnO_4 structure Sm^{3+} goes to the Sn^{4+} site, which is much smaller. It means that charge transfer from oxygen to Sm^{3+}/Sn^{4+} is much easier in barium ortho-stannates.

The broadening of PL emission lines (*Figure 9.4a* and *b*) is governed by the Stark effect caused by the crystal field interaction. The 4f orbitals of the Sm^{3+} ion are only partially filled by five electrons ($4f^5$) and the resulting unpaired electrons give twice Kramer degeneration in any crystal-field lower than cubic. The maximum number of Stark sublevels for Sm^{3+} ion with $^{2S+1}L_J$ multiplets is (2J+1)/2 due to the Kramer degeneracy of its odd $4f^5$ electron configuration. The energy level splitting effect is observed clearly in the emission spectra of Ba_2SnO_4:2% Sm^{3+} sample (*Figure 9.4c*). As expected, 3 and 4 sharp spectral lines are observed for J=5/2 and 7/2, respectively [144].

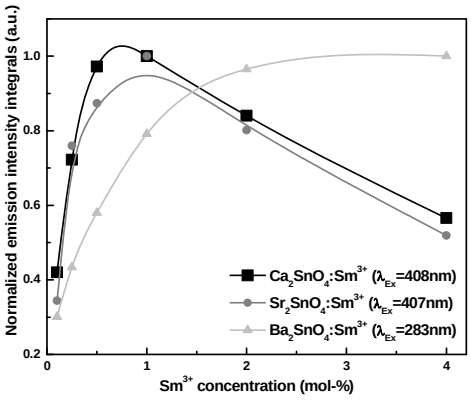

Figure 9.5 *Emission intensity integrals as a function of Sm^{3+} concentration in different alkaline earth stannate phosphors.*

The dependence of the integral of the emission intensity as a function of activator concentration is depicted in *Figure 9.5*. The photoluminescence intensity of $Ca_2SnO_4:Sm^{3+}$(λ_{ex}= 408 nm) and $Sr_2SnO_4:Sm^{3+}$ (λ_{ex}= 407 nm) phosphors increases with the Sm^{3+} content, reaches its maximum at a dopant concentration of about 1 mol-%, and then significantly decreases with a further increase of the Sm^{3+} concentration due to concentration quenching. This phenomenon is frequently observed in rare-earth doped luminescent materials as the dopant level increases and is often ascribed to a non-radiative energy transfer from one activator to the adjacent ones. As the probability of this process is distant dependent it increases with an increase of the activator concentration [145]. In contrast to that, concentration quenching is not observed for $Ba_2SnO_4:Sm^{3+}$ up to a samarium concentration of 4 mol-%. Moreover, the emission integral intensity values for 2 and 4 mol-% Sm-doped Ba_2SnO_4 (λ_{ex}= 283 nm) phosphors are very similar. However, powder XRD analysis revealed that the Ba_2SnO_4 sample doped with 4 mol-% Sm^{3+} is not of single phase (*Figure 9.3*), thus a sample doped by 2 mol-% Sm^{3+} was selected for the further studies.

Figure 9.4a represents normalized integrated values of Ca_2SnO_4:1% Sm^{3+}emission spectra, recorded in 100-500 K temperature range. For the calculations of $TQ_{1/2}$ values (the temperature, at which the luminescent sample loses half of its light output) the Boltzmann sigmoidal fit of the temperature dependent emission integrals was employed. The obtained results revealed that Ca_2SnO_4:1% Sm^{3+} phosphors loses half of its efficiency at around 622 K (349 °C).

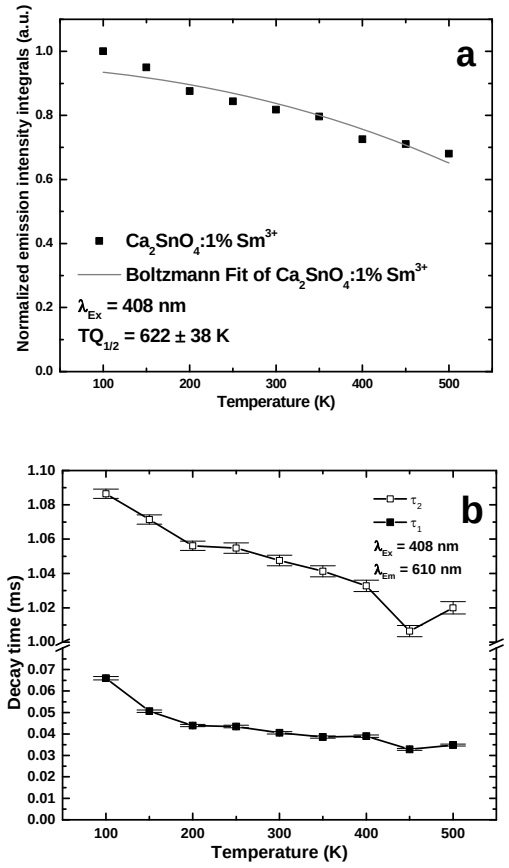

Figure 9.4 *(a) Normalized emission integrals and (b) emission decay values as a function of temperature of the Ca_2SnO_4:1% Sm^{3+} sample.*

All temperature dependent decay curves were fitted by a double exponential decay function (Marquardt–Levenberg algorithm) [145]:

$$I(t) = I_0 + A_1 e^{\left(\frac{t}{\tau_1}\right)} + A_2 e^{\left(\frac{t}{\tau_2}\right)} \qquad \text{(Eq. 9.1)}$$

where I and I_0 are the luminescence intensity at time t and 0, respectively; t is time; A_1 and A_2 are constants; τ_1 and τ_2 are the decay times. The calculated decay constants τ revealed that the decay curve consists of a fast decay process (τ_1) and a subsequent slow decay process with a long tail (τ_2). The

estimated $TQ_{1/2}$ value for Ca_2SnO_4:1% $Sm^{3+}$is 622 K (≈ 349 °C), however, this result was derived from a measurement between 100 and 500 K (*Figure 9.4a*), which means that the uncertainty is rather large. Temperature dependent decay values for Ca_2SnO_4:1% Sm^{3+} are plotted in *Figure 9.4b*. It is evident that both decay constants decrease gradually and correlate well with the temperature dependent emission integrals of Ca_2SnO_4:1% Sm^{3+} specimen. The first exponential term (τ_1) is not from the bulk because it is too fast (0.03 – 0.07 ms). It is most likely due to Sm^{3+} located close to the surface. According to vast literature data it is known that some deviation from single exponential decay could be due to surface nonradiative processes [146-148]. The second (dominating) exponential term (τ_2) values fall into 1.0 – 1.1 ms range.

The photoluminescence thermal quenching behavior of Sr_2SnO_4:1% Sm^{3+} phosphor is depicted in *Figure 9.5a*. The emission integrals only slightly decrease even at temperatures as high as 500 K. Such thermal stability is a desirable property for application in various fields, for instance, in solid state lighting [118]. Unfortunately, the estimation of $TQ_{1/2}$ from temperature dependent emission integrals for Sr_2SnO_4:1% Sm^{3+} phosphor cannot be done because Boltzmann sigmoidal fit curve does not overpass the turning point (half of the value in this case).

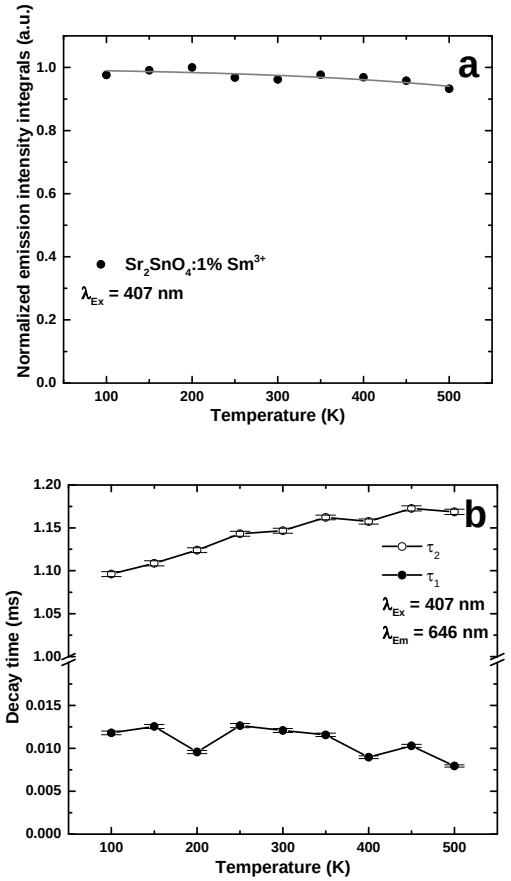

Figure 9.5 *(a) Normalized emission integrals and (b) emission decay values as a function of temperature of the Sr_2SnO_4:1% Sm^{3+} sample.*

The temperature dependent lifetime values for Sm^{3+} emission in Sr_2SnO_4 host are plotted in *Figure 9.5b*. It is interesting to note, that decay time values (τ_2 = 1.1 – 1.17 ms) become longer at higher temperatures, indicating the increase of the internal quantum efficiency of the activator.

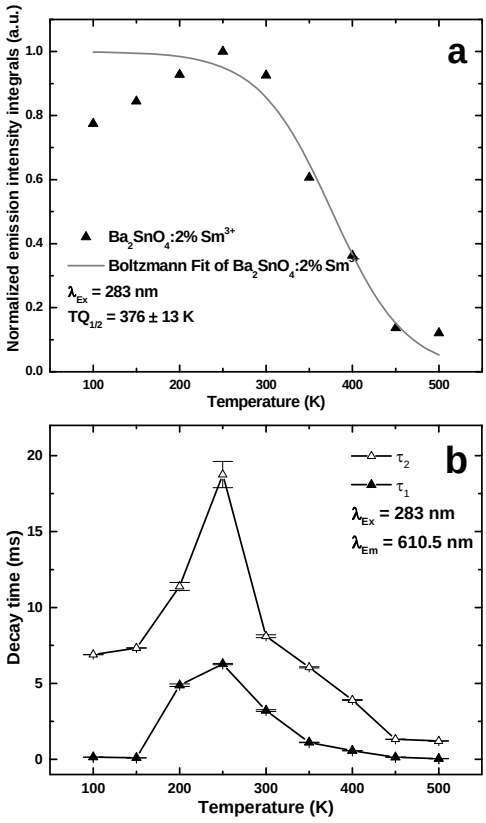

Figure 9.6 *(a) Normalized emission integrals and (b) emission decay values as a function of temperature of the Ba_2SnO_4:2% Sm^{3+} sample.*

Figure 9.6a clearly shows that the integrals of the emission intensity integral increases from 100 to 250 K for Ba_2SnO_4:2% Sm^{3+}sample. The further increase of the sample temperature leads to a decrease in emission intensity and finally nearly all emission vanishes if temperature reaches 500 K. The employed Boltzmann sigmoidal fit revealed that Ba_2SnO_4:2% Sm^{3+} phosphor losses half of its efficiency at around 376 K (≈ 103 °C) if measured from 100 to 500 K. The temperature dependent photoluminescence decay time values of Ba_2SnO_4:2% Sm^{3+}specimen are given in *Figure 9.6b*. The observed trend is very similar to the emission intensity integrals and decay times increase with increasing temperature up

to 250 K. We assume that the peak at 250 K is a sort of glow peak, i.e. the extraordinarily long decay time is caused by the thermal activation of traps. If we excite $Ba_2SnO_4:Sm^{3+}$ at 283 nm and assume that this excitation band is a O^{2-}-Sn^{4+} CT, forming a trapped electron onto the Sn^{4+} site ("Sn^{3+}"), the reactivation of such electron will be temperature dependent and optimal at a temperature, where the thermal energy is as large as the depth of the defect. This theory is also supported by the observation of the long afterglow in the decay curves of $Ba_2SnO_4:Sm^{3+}$, which is completely lacking for the other stannates.

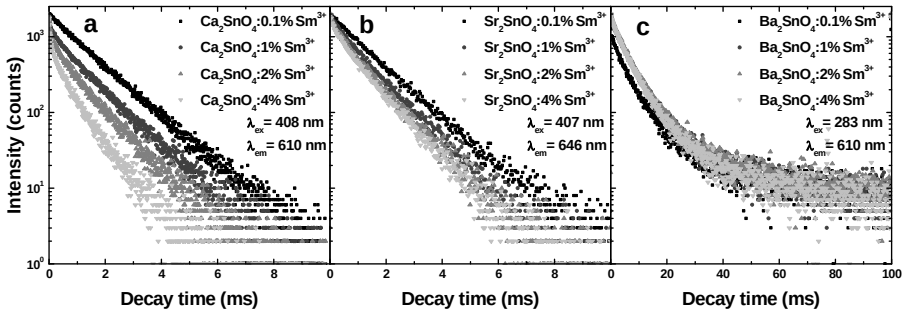

Figure 9.7 *Decay curves of $M_2SnO_4:Sm^{3+}$ as a function of Sm^{3+} concentration.*

Several concentration dependent decay curves of Sm^{3+} doped alkaline earth stannates phosphors are shown in *Figure 9.7*. It is obvious that the derived decay times for $Ca_2SnO_4:Sm^{3+}$ (*Figure 9.7a*) and $Sr_2SnO_4:Sm^{3+}$ (*Figure 9.7b*) become shorter with higher activator concentration. This can be related with an increase of energy transfer between Sm^{3+} ions at the cost of radiative relaxation. However, the decay curves of all $Ba_2SnO_4:Sm^{3+}$ samples are nearly identical (see *Figure 9.7c*), suggesting a similar internal quantum efficiency of Sm^{3+} ions at all concentrations.

Figure 9.8 a, b and c represent the fragments of CIE 1931 chromaticity diagram with color points of $Ca_2SnO_4:Sm^{3+}$, $Sr_2SnO_4:Sm^{3+}$ and

$Ba_2SnO_4:Sm^{3+}$, respectively. The color points are shifted towards lower x values (from red to orange region) according to the sequence Ca → Sr → Ba. This goes hand in hand with calculated LE values which increase following the same trend.

Since the human eye is more sensitive to orange light this leads to higher LE values if the emission shifts to the orange spectral range. Moreover, it is also obvious that color points are located very close to the edge of the CIE 1931 diagram thus indicating the high color saturation.

In this chapter it is discussed how the incorporation of Sm^{3+} into different host material can tune the emission color of resulting phosphor. The thermal quenching studies revealed that $Sr_2SnO_4:Sm^{3+}$ phosphor exhibits highest thermal stability in temperature range from 100 to 500 K. The slowest decay time values were obtained for $Ba_2SnO_4:Sm^{3+}$ phosphor. Moreover, XRD data and PL spectra of $Ba_2SnO_4:Sm^{3+}$ specimen evidently differs from $Ca_2SnO_4:Sm^{3+}$ and $Sr_2SnO_4:Sm^{3+}$ samples. For the first time we demonstrate experimentally that Sm^{3+} ions occupy Ca and Sr sites in the Ca_2SnO_4 and Sr_2SnO_4 ortho-stannate structures. However, the substitution of Sn site occurs in the barium ortho-stannate Ba_2SnO_4 structure.

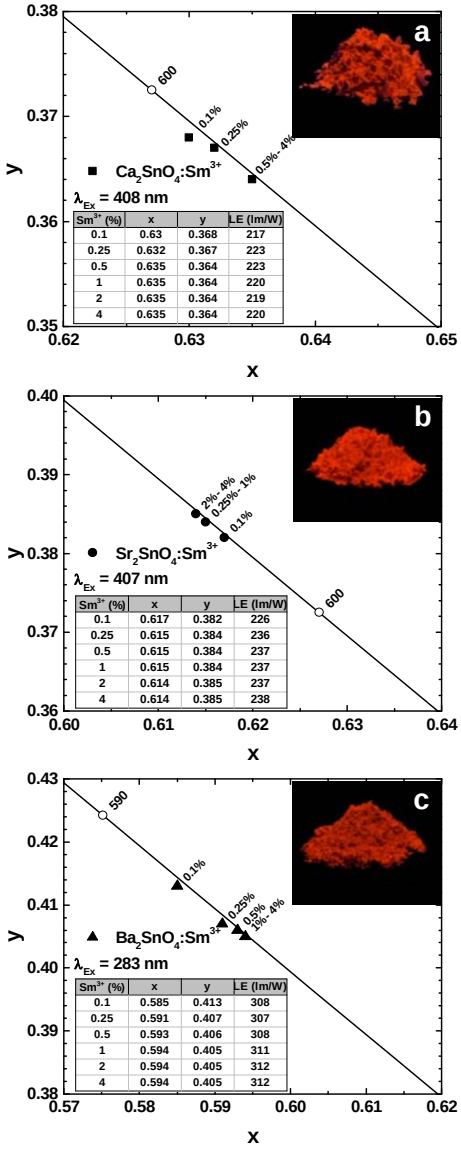

Figure 9.8 *CIE1931 color points of: (a) $Ca_2SnO_4:Sm^{3+}$, (b) $Sr_2SnO_4:Sm^{3+}$, and (c) $Ba_2SnO_4:Sm^{3+}$ for different Sm^{3+} concentrations. Exact color points and LE values for each Sm^{3+} concentration are given in the inset tables. The inset pictures show digital images of the respective compounds excited at 254 nm.*

The morphology of synthesized phosphor powders was examined by taking SEM pictures, which are shown in *Figure 9.9*.

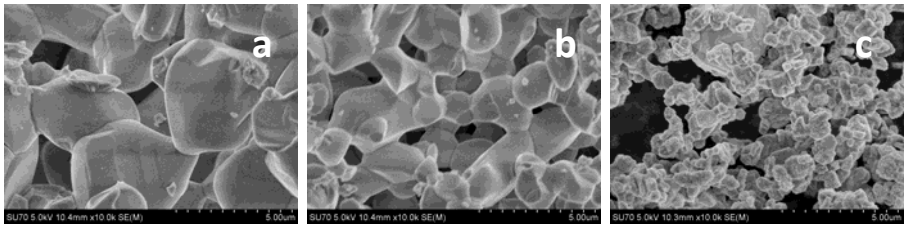

Figure 9.9 *SEM images of: (a) Ca_2SnO_4:1% Sm^{3+}, (b) Sr_2SnO_4:1% Sm^{3+}, and (c) Ba_2SnO_4:2% Sm^{3+} powders sintered at 1400 °C under magnification of 10k.*

It is obvious that Ca_2SnO_4:1% Sm^{3+}sample is composed of slightly agglomerated irregularly shaped particles with a particle size distribution ranging from 2 to 5 μm. Similar morphological features were observed for the Sr_2SnO_4:1% Sm^{3+} sample. The main difference is that smaller particles (0.5–2 μm) have formed in this case. However, these smaller particles tend to form prolongated agglomerates. The size of these "necked to each other" Sr_2SnO_4:1% Sm^{3+} crystalline grains is about of 2-5 μm. Interestingly, the smallest particles (0.25–1 μm) among three host materials were obtained for Ba_2SnO_4:2% Sm^{3+} sample. Obviously, the particle size and shape of Sm^{3+}-doped alkaline earth ortho-stannates are dependent on the type of alkaline earth metal.

Chapter 10. Luminescence of Eu^{3+} in Ca_2SnO_4, Sr_2SnO_4 and Ba_2SnO_4

10.1 XRD Data Analysis

Figure 10.1 presents the XRD patterns of Ca_2SnO_4 powders doped with different content of europium and annealed at 1400 °C for 10 h in air. The peak positions for Ca_2SnO_4:4% Eu^{3+} sample match well with the reference data of Ca_2SnO_4 (ICDD#04-008-2918). The existence of $CaSnO_3$ (ICDD#04-015-3326) minor phase ($2\theta = 22.4$ °) can be observed in all samples, however the intensity of characteristic reflections assigned to the impurity phase start to increase, when Eu^{3+} concentration exceeds 8 mol %.

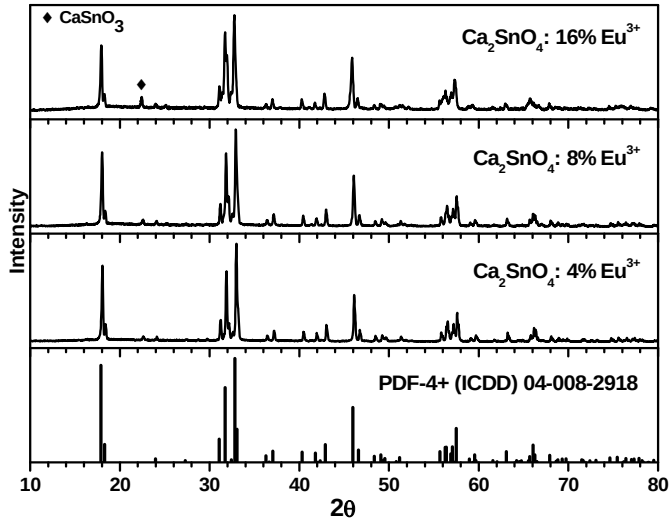

Figure 10.1 *Powder XRD patterns of Ca_2SnO_4:Eu^{3+}.*

The powder XRD patterns of Sr_2SnO_4 as a function of Eu^{3+} concentration are shown in *Figure 10.2*. All the peaks in Sr_2SnO_4:4% Eu^{3+} pattern can be indexed to a single phase Sr_2SnO_4 (ICDD#04-010-4448). The formation of

$Sr_3Sn_2O_7$ (ICDD#00-025-0914) and Eu_2O_3 (ICDD#00-034-0072) secondary phases occurs when dopant concentration reaches 16 mol %.

Figure 10.3 shows the powder XRD patterns of europium doped barium ortho-stannate samples. The XRD analysis reveals that single phase compound can be obtained when dopant concentration is ≤ 2 mol %. Further increase of Eu^{3+} content resulted in the formation of $Ba_2EuSnO_{5.5}$ (ICDD#04-002-8282) as a secondary phase.

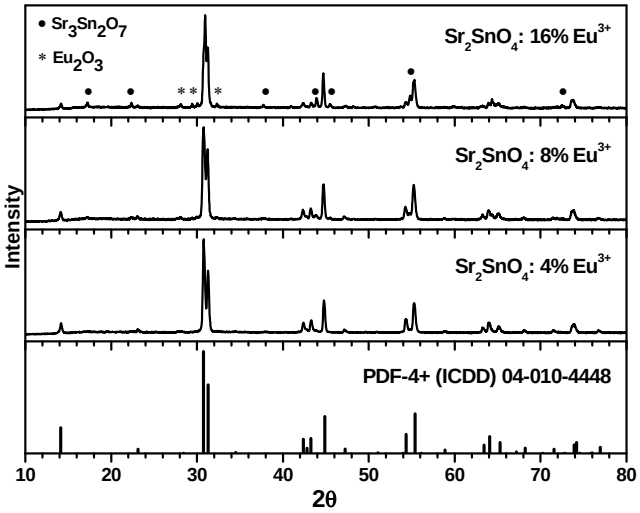

Figure 10.2 *Powder XRD patterns of $Sr_2SnO_4:Eu^{3+}$.*

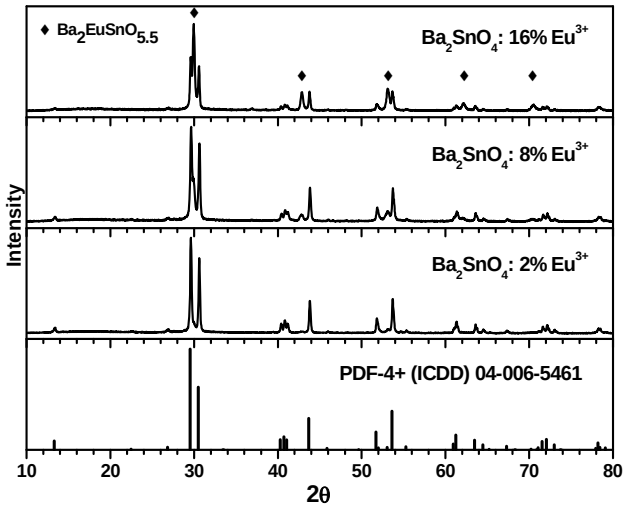

Figure 10.3 *Powder XRD patterns of $Ba_2SnO_4:Eu^{3+}$.*

10.2 Optical Properties

Figure 10.4a, b and *c* show the excitation, emission and diffuse reflectance spectra of Ca_2SnO_4:4% Eu^{3+}, Sr_2SnO_4:4% Eu^{3+} and Ba_2SnO_4:2% Eu^{3+}, respectively. The diffuse reflectance spectra of each compound, recorded in the spectral region from 250 to 800 nm, exhibits a strong broad absorption band in the UV region.

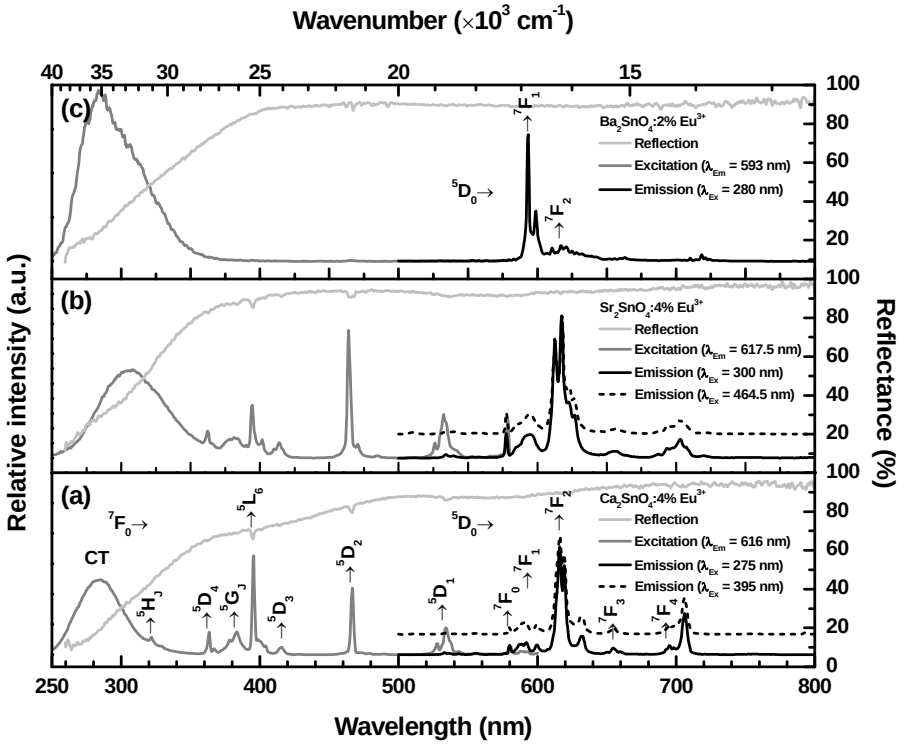

Figure 10.4 *Excitation, emission and reflection spectra of (a) Ca_2SnO_4:4% Eu^{3+} (b) Sr_2SnO_4:4% Eu^{3+} and (c) Ba_2SnO_4:2% Eu^{3+}.*

That corresponds to the transition from the $^7F_0$ ground state to the charge transfer (CT) state due to oxygen to europium interaction. The electrons move from completely filled 2p orbitals of O^{2-} to partially filled $4f^6$ levels of Eu^{3+} [149]. Two weak absorption peaks at 395 and 464.5 nm are assigned to typical f-f transitions of trivalent europium ion, which can also be observed in the excitation spectra of Ca_2SnO_4:4% Eu^{3+} (*Figure 10.4a*) and Sr_2SnO_4:4% Eu^{3+} (*Figure 10.4b*). The excitation spectrum of Ca_2SnO_4:4% Eu^{3+} phosphor monitored at λ_{Em} 616 nm is shown in *Figure 10.4a*. Several groups of sharp lines ranging from 350 and 550 nm are assigned to the characteristic transitions of Eu^{3+} between $^7F_0$ and $^5D_4$,

^5G_J, $^5L_6$, $^5D_{3,2,1}$ levels. The broad band at 275 nm, overlapped with the $^7F_0 \rightarrow {}^5H_J$ transition, can be ascribed to the CT between Eu^{3+} ions and the surrounding oxygen anions. The emission spectra of Ca_2SnO_4:4% Eu^{3+} excited with different wavelengths, corresponding to the CT (λ_{Ex} = 275 nm) and $^7F_0 \rightarrow {}^5L_6$ (λ_{Ex} = 395 nm) transitions, are shown in *Figure 10.4a*. The emission spectrum shape and peak positions remained the same using both irradiation wavelengths. Four emission peaks at 592, 616, 655 and 706 nm correspond to intra-4f-shell transitions from the excited level $^5D_0$ to lower levels ^7F_J (J = 1, 2, 3, 4) for Eu^{3+} ions. The emission situated at 592 nm is due to $^5D_0 \rightarrow {}^7F_1$ magnetic dipole transition, which is insensitive to the site symmetry. The dominant emission peak situated at 616 nm showing a prominent and bright red light is due to $^5D_0 \rightarrow {}^7F_2$ electric dipole transition, induced by the lack of inversion symmetry at the Eu^{3+} site, and is much stronger than that of the transition of the $^7F_1$ state [150].

In Ca_2SnO_4 structure the Ca^{2+} ions are surrounded by seven oxygen ions in an arrangement of low symmetry and occupy the only one site (C_s) [151].The PL spectra (*Figure 10.4a*) confirms that Eu^{3+} ions (0.95 Å → CN = 6) do not occupy Sn^{4+} (0.69 Å → CN = 6) site with a center of symmetry but replace closer in size Ca^{2+} (1.06 Å → CN = 7). Splitting of the $^5D_0 \rightarrow {}^7F_2$ transition in Ca_2SnO_4:4% Eu^{3+} emission spectra suggests that the Eu^{3+} ions occupied two nonequivalent sites, one is the Ca^{2+} (C_s) in the structure of Ca_2SnO_4 and the other is the Ca^{2+} ions sites in the small amount of $CaSnO_3$ phase. This is in agreement with results of Yang et al. [152].

The PL spectra of Sr_2SnO_4 doped with 4 mol % of Eu^{3+} are shown in *Figure 10.4b*. The excitation spectra of Sr_2SnO_4:4% Eu^{3+} is nearly the same as for Ca_2SnO_4:4% Eu^{3+} (*Figure 10.4a*). The charge transfer band shifts towards the lower energy side and intensity of $^7F_0 \rightarrow {}^5D_2$ transition located

at 464.5 nm increases if compared to Ca_2SnO_4:4% Eu^{3+} sample. Moreover, excitation maximum of CT transition shifts towards the red spectral region when M^{2+} is changed from Ca^{2+} to Sr^{2+}.

As reported in literature, the CT transition is strongly affected by covalency between oxygen and activator ion [97, 153]. In the bond structure of Eu^{3+}–O^{2-}–M^{2+} (M = Ca, Sr and Ba), the degree of covalency of the Eu^{3+}–O^{2-} bond is the weakest in the $CaSnO_3$ structure because Ca^{2+} attracts electrons of O^{2-} most strongly due to the fact that it has the largest electronegativity and the smallest radius. Therefore, it could be easier for the electronic transition from the 2p orbital of O^{2-} to the 4f orbital of Eu^{3+} in the $BaSnO_3$ host than in the $CaSnO_3$ one, and thus the CT transition energy of Eu^{3+} decreases in the series of Ca^{2+} to Ba^{2+} stannate phosphors. This is in a good agreement with the results reported by Zhiwu et al. [154].

The emission spectra of Sr_2SnO_4:4% Eu^{3+} phosphor recorded using different excitation wavelengths (λ_{Ex} = 300 nm and λ_{Ex} = 464.5 nm) are identical. The $^5D_0 \rightarrow {}^7F_J$ transitions with $J = 0$, 1, 2, 4 are seen at about 578 nm, 593 nm, 617.5 nm and 703 nm, respectively, as shown in *Figure 10.4b*. The intense peak assigned to $^5D_0 \rightarrow {}^7F_0$ transition was observed in all europium doped Sr_2SnO_4 samples. In general, the $J = 0 \rightarrow J' = 0$ level is parity-forbidden by the selection rule of the Judd-Ofelt theory for an electric dipole transition of a rare earth ion between $4f^n$-states. The energy gap between $^7F_1$ and $^7F_0$ of the Eu^{3+} ions is so small that the $^7F_1$ character may be mixed into the $^7F_0$ level of C_{4v} symmetry which is not centrospherical. The forbidden $^5D_0 \rightarrow {}^7F_0$ transition gains intensity from the *J-J* mixing [149, 155].

Photoluminescence (PL) excitation spectrum of Ba_2SnO_4:2% Eu^{3+} monitored at λ_{Em} = 593 nm shows the strongest broad band from 250 to 340

nm due to the charge transfer band of Eu^{3+}–O^{2-} (*Figure 10.4c*). The direct f-f transitions are negligible small and almost unseen.

The emission spectrum of Ba_2SnO_4 doped with 2 mol % of Eu^{3+} is shown in *Figure 10.4c*. A strong emission peak due to the magnetic dipole transition $^5D_0 \rightarrow {}^7F_1$ was observed at 593 nm. The magnetic dipole transition is dominant when Eu^{3+} ions in the crystal lattice occupy a site with inversion symmetry [97]. Therefore, in the host material Ba_2SnO_4 crystal, the emitting center occupies the sites of Sn^{4+}.

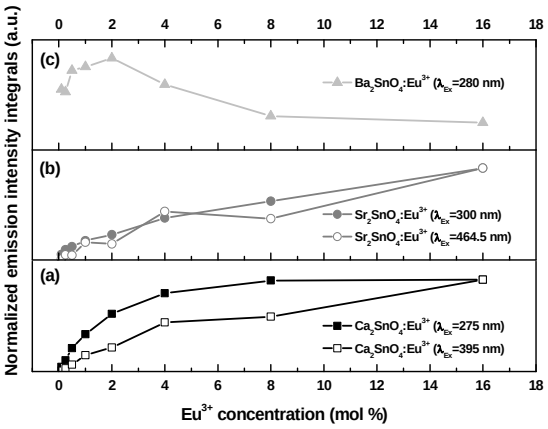

Figure 10.5 *Emission intensity integrals as a function of Eu^{3+} concentration in different alkaline earth stannate phosphors.*

The emission intensity integrals against Eu^{3+} concentration in alkaline earth ortho-stannates are plotted in *Figure 10.5*. The emission intensity of Ca_2SnO_4:Eu^{3+} (*Figure 10.5a*) excited with 275 nm monotonically increases up to 8 mol % and then remains unchanged, while excitation with 395 nm resulted in gradual increase of intensity. A sharp concentration quenching was not observed for Ca_2SnO_4:Eu^{3+} phosphor. This continuous enhancement in emission intensity can be explained by the presence of the secondary phase compound, namely $CaSnO_3$:Eu^{3+}, which was reported to be optically active [140].

The photoluminescence intensity as a function of dopant concentration in Sr_2SnO_4 phosphor is depicted in *Figure 10.5b*. The dependence is linear without obvious differences for both excitation wavelengths. Based on the XRD results (*Figure 10.2*) the formation of $Sr_3Sn_2O_7$ phase can be observed when dopant concentration is higher than 8 mol %. As far as we know only Sm^{3+} doped $Sr_3Sn_2O_7$ phosphor was reported [145]. Thus the existence of the $Sr_3Sn_2O_7$:Eu^{3+} phase may give an additional input towards the emission intensity increase.

Figure 10.5c shows the dopant concentration dependence on the emission intensity integral of Eu^{3+} doped Ba_2SnO_4 samples. The rare earth concentration had a significant influence on the PL intensity in Ba_2SnO_4 host material. In lower Eu^{3+} concentration region the integral emission intensity increased with increasing Eu^{3+} concentration. The optimal Eu^{3+} concentration, that gave the saturated PL intensity, was 2 mol %. The emission intensity diminishes quickly as Eu^{3+} concentration exceeds 2 mol % due to the concentration quenching.

The temperature dependent emission integral intensities of Ca_2SnO_4:4% Eu^{3+} sample excited at 275 and 395 nm are shown in *Figure 10.6a*. The emission intensity decreases with increasing temperature when excitation wavelength of 395 nm was used. However, the dependence of emission on temperature is quite different in the case of excitation at 275 nm. The intensity starts abruptly to increase from 250 K and reaches a maximum at 350 K.

With further increasing of temperature emission intensity decreases a little bit faster in comparison if sample was excited 395 nm. This observation indicates different emission behavior if excitation wavelength decreases from 395 to 275 nm.

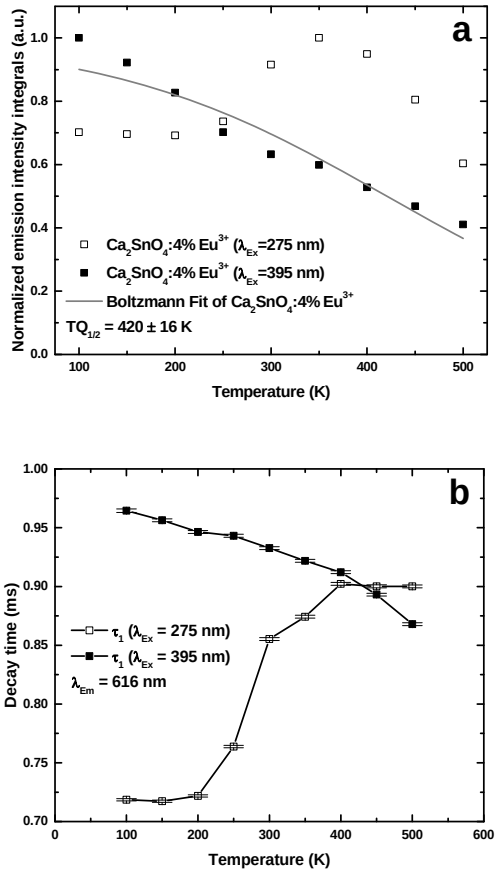

Figure 10.6 *(a) Normalized emission integrals and (b) emission decay values as a function of temperature of the Ca_2SnO_4:4% Eu^{3+} sample.*

However, a possible explanation of this phenomenon requires a more detailed study. The temperature dependent decay curves were fitted by a

mono exponential decay function. The calculated decay time values of the Ca_2SnO_4:4% Eu^{3+} phosphor as a function of temperature under excitation at 275 and 395 nm are shown in *Figure 10.6b*. Again the decay time values decreased with increasing temperature when excitation wavelength of 395 nm was used. However, the excitation at 275 nm resulted in opposite dependence.

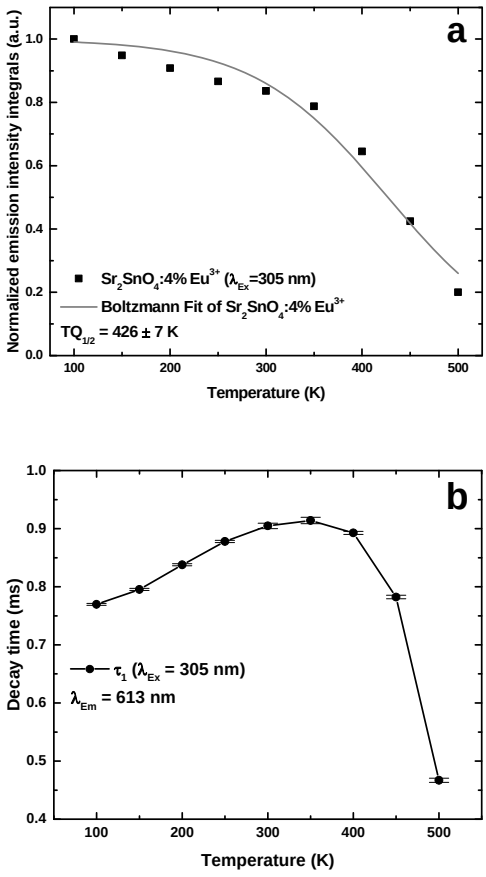

Figure 10.7 *(a) Normalized emission integrals and (b) emission decay values as a function of temperature of the Sr_2SnO_4:4% Eu^{3+} sample.*

The temperature dependent emission integral intensities of Sr_2SnO_4:4% Eu^{3+} sample excited at 305 nm is presented in *Figure 10.7a*. As seen, the emission intensity decreases with increasing temperature. A Boltzmann-sigmoidal fit was employed for calculation of $TQ_{1/2}$ (the temperature, at which the phosphor loses 50% of its efficiency). Apparently, the PL integral monotonically increases up to 350 K and abruptly decreases with further increasing of temperature. It is obvious that Sr_2SnO_4:4% Eu^{3+} phosphor possess stronger thermal quenching than Ca_2SnO_4:4% Eu^{3+} sample. It is interesting to note that temperature dependent decay curves showed mono exponential decay up to 250 K and bi-exponential behavior at elevated temperature.

Figure 10.8a displays the emission integral intensity of Ba_2SnO_4:1% Eu^{3+} phosphor excited at 280 nm as a function of temperature. Evidently, the emission integral intensity decreases with increasing temperature.

The concentration dependent decay curves of $M_2SnO_4:Eu^{3+}$ phosphors are shown in *Figure 10.9*. The decay curves or decay speed of the samples differ from each other, thus suggesting about different internal efficiency of activator ion. The results shown in *Figure 10.9* demonstrated that these phosphors had different decay times, which indicates the creation of different depth of trapping energy levels in $M_2SnO_4:Eu^{3+}$.

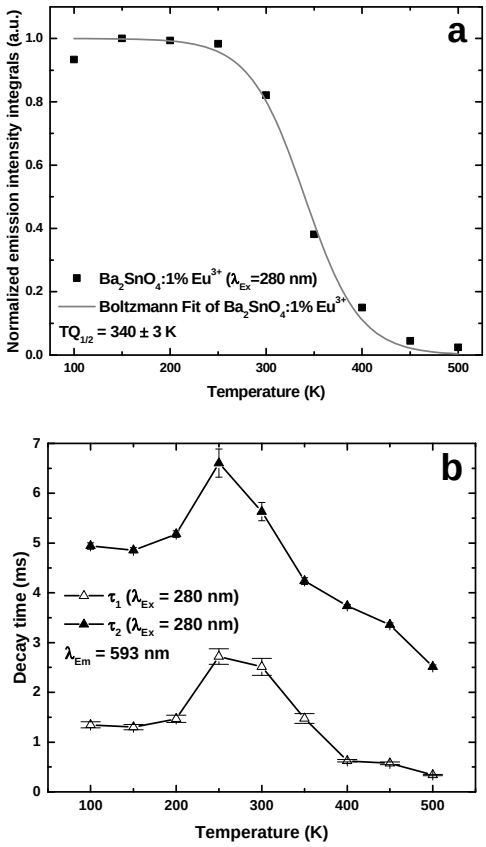

Figure 10.8 *(a) Normalized emission integrals and (b) emission decay values as a function of temperature of the Ba_2SnO_4:1% Eu^{3+} sample.*

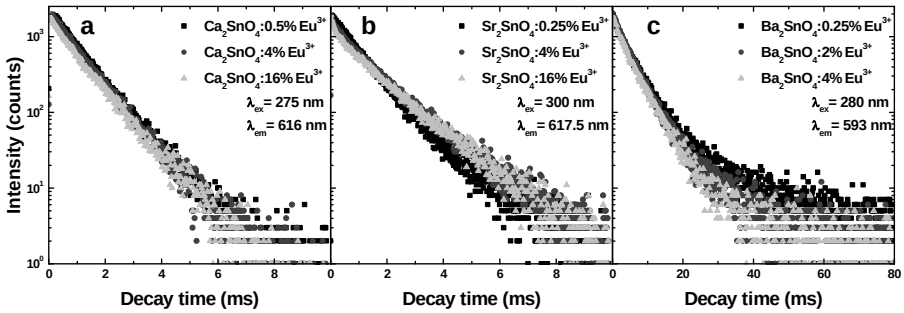

Figure 10.9 *Decay curves of $M_2SnO_4:Eu^{3+}$ as a function of Eu^{3+} concentration.*

Figure 10.10a, b and *c* show the chromaticity coordinates of $Ca_2SnO_4:Eu^{3+}$, $Sr_2SnO_4:Eu^{3+}$ and $Ba_2SnO_4:Eu^{3+}$ doped with different Eu^{3+} content, respectively. With increasing Eu^{3+} concentration, the *x* values show an increasing trend and the *y* values show a decreasing trend. However, comparing three host materials with each other, in concentration range from 1 to 16 mol % of Eu^{3+}, the color points are shifted towards lower x values (from red to orange region) in sequence Ca → Sr → Ba.

The trivalent europium ion is often used as a probe for estimation of site symmetry of metal ion, to evaluate crystal field strength and to assess crystal defects in the solid state [156, 157]. For that reason Eu^{3+} doped calcium, strontium and barium ortho-stannates were synthesized and comparatively studied in this chapter. The emission spectra of Ba_2SnO_4:1% Eu^{3+} (*Figure 10.4c*) shows dominating magnetic dipole transition $^5D_0 \rightarrow {}^7F_1$ at 593 nm, which confirms that Eu^{3+} occupies the sites of Sn^{4+}.

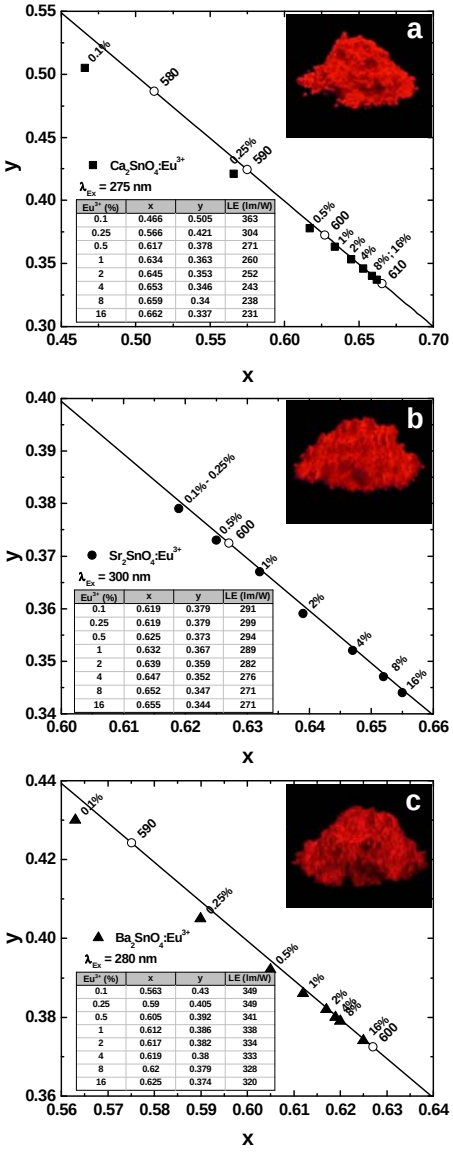

Figure 10.10 *CIE1931 color points of: (a) $Ca_2SnO_4:Eu^{3+}$, (b) $Sr_2SnO_4:Eu^{3+}$, and (c) $Ba_2SnO_4:Eu^{3+}$ with different Eu^{3+} concentrations. Exact color points and LE values for each Eu^{3+} concentration are given in inset tables. The inset pictures shows the digital pictures of the respective compounds excited at 254 nm.*

Chapter 11. Luminescence of Pr^{3+} in $CaSnO_3$, $SrSnO_3$ and Ca_2SnO_4

11.1 XRD Data Analysis

The XRD patterns of $CaSnO_3$ samples as a function of Pr^{3+} concentration together with the standard data of $CaSnO_3$ (ICDD#04-015-3326) are shown in *Figure 11.1*. The obtained results demonstrate that Pr^{3+} ions do not have significant influence on the crystal structure at low concentration. However the existence of two secondary phases, namely $Pr_2Sn_2O_7$ (ICDD#00-087-1219) and SnO_2 (ICDD#00-077-0450) was detected, when dopant concentration reached 4 mol %.

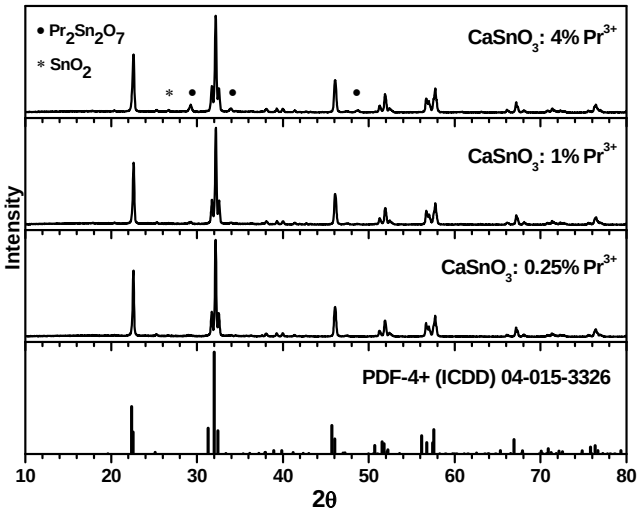

Figure 11.1 *Powder XRD patterns of $CaSnO_3$:Pr^{3+}.*

The XRD patterns of $SrSnO_3$ as a function of Pr^{3+} concentration are illustrated in *Figure 11.2*. The diffraction peaks of all samples are well consistent with the standard data of $SrSnO_3$ (ICDD#04-010-2598). The

presence of trace impurities in 4 mol % doped $SrSnO_3$ sample indicate that solubility of Pr^{3+} ions in this host material is better comparing to $CaSnO_3$.

Figure 11.3 represents the powder XRD patterns of Ca_2SnO_4:Pr^{3+} phosphors as a function of Pr^{3+} concentration. The patterns of synthesized samples match well with the reference pattern of Ca_2SnO_4 (ICDD#04-008-2918). The phase analysis revealed that the Pr^{3+} ions completely dissolved in the Ca_2SnO_4 host lattice. The unavoidable presence of calcium meta-stannate phase was detected in all samples, similar to earlier discussed Sm^{3+} and Eu^{3+} doped Ca_2SnO_4 samples

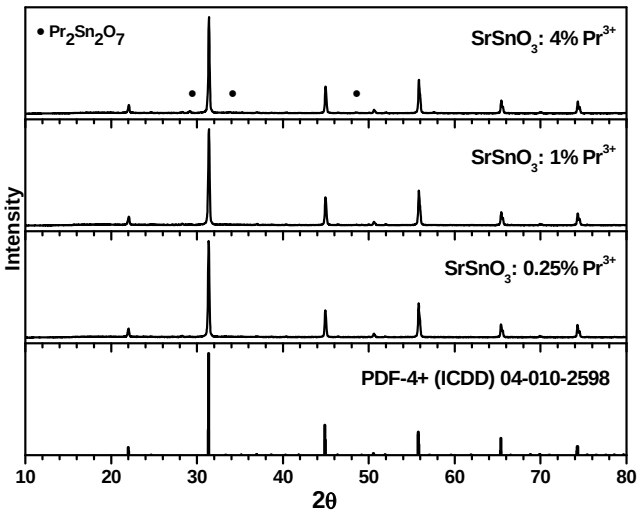

Figure 11.2 *Powder XRD patterns of $SrSnO_3$:Pr^{3+}.*

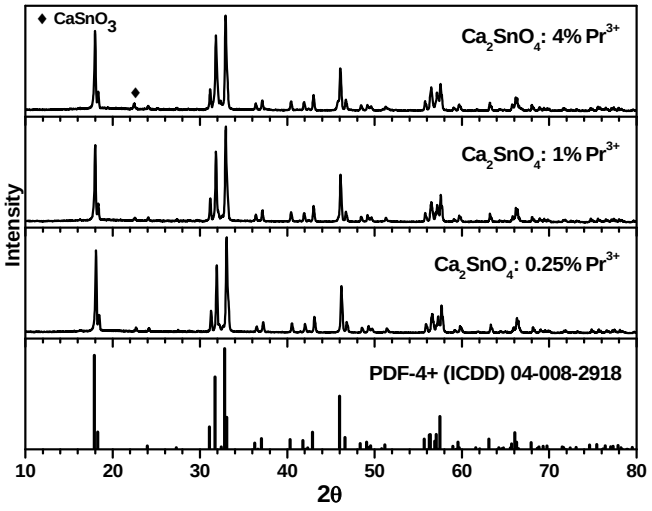

Figure 11.3 *Powder XRD patterns of $Ca_2SnO_4:Pr^{3+}$.*

11.2 Optical Properties

Figure 11.4a, b and *c* show the excitation, emission and diffuse reflectance spectra of $CaSnO_3$:1% Pr^{3+}, $SrSnO_3$:4% Pr^{3+} and Ca_2SnO_4:0.25% Pr^{3+}, respectively. The excitation spectrum of $CaSnO_3$:1% Pr^{3+} (*Figure 11.4a*) and $SrSnO_3$:4% Pr^{3+} (*Figure 11.4b*) exhibit broad bands in spectral region from 250 to 300 nm and 250 to 350 nm, respectively. These bands are attributed to the absorption of the host lattice (HL). The excitation peaks of $CaSnO_3:Pr^{3+}$ and $SrSnO_3:Pr^{3+}$ are centered at 265 and 290 nm, respectively. Unfortunately the incorporation of praseodymium ion into $BaSnO_3$ host lattice did not show any luminescence.

The emission spectrum of Pr^{3+} doped $CaSnO_3$ sample was measured under excitation of 265 nm at ambient temperature is shown in *Figure 11.4a*. It consists of five major emission lines peaking at around 488, 530, 613, 656 and 742 nm are assigned to the f-f transitions of $^3P_0 \rightarrow {}^3H_4$, $^3P_0 \rightarrow {}^3H_5$, $^1D_2 \rightarrow {}^3H_4$, $^3P_0 \rightarrow {}^3F_2$ and $^3P_0 \rightarrow {}^3F_4$ states of Pr^{3+} ions,

respectively. The emission spectra of $SrSnO_3$:4% Pr^{3+} phosphor (*Figure 11.4b*) excited at 290 nm is quite similar to $CaSnO_3$:1% Pr^{3+} sample. However, the characteristic emission lines of $SrSnO_3$:4% Pr^{3+} phosphor are slightly shifted toward higher energies. The most intensive emission peaks are located in the green (500 nm), orange (600 nm) and red (660 nm) spectral region.

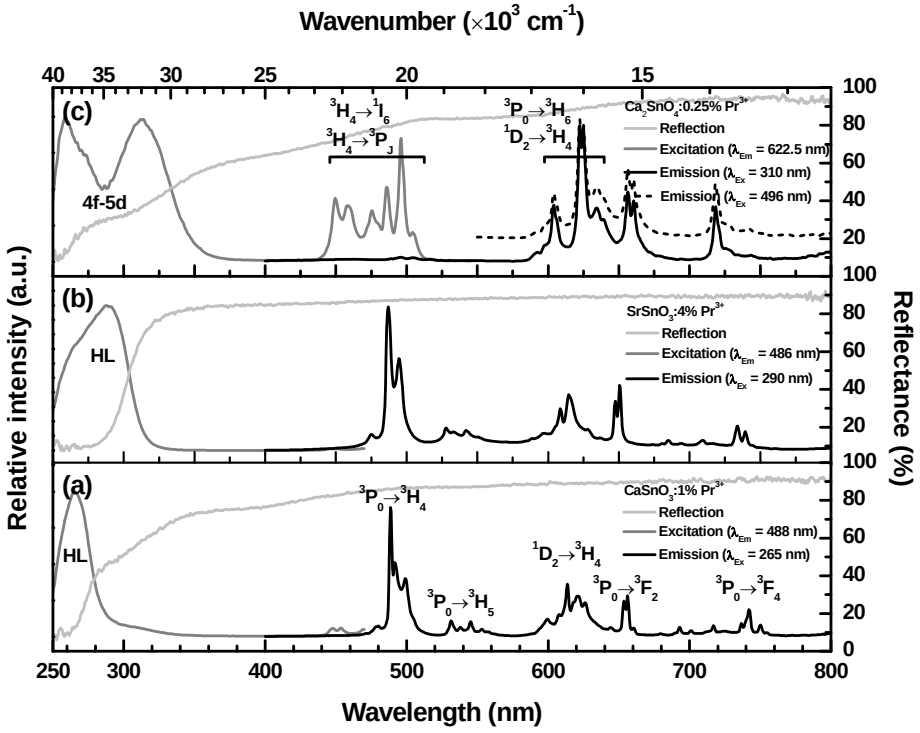

Figure 11.4 *Excitation, emission and reflection spectra of (a) $CaSnO_3$:1% Pr^{3+} (b) $SrSnO_3$:4% Pr^{3+} and (c) Ca_2SnO_4:0.25% Pr^{3+}.*

Such mixture of complementary colors caused white coloration in the Pr^{3+} doped $CaSnO_3$ and $SrSnO_3$ samples [158, 159].

The excitation spectrum of 0.25 mol % Pr^{3+} doped Ca_2SnO_4 phosphor monitored at 622.5 nm is depicted in *Figure 11.4c*. The excitation spectra

can be divided into two main parts. One is in the range of 250 – 370 nm with two strong broad bands situated at 258 and 310 nm respectively, which can be ascribed to the 4f – 5d transition of Pr^{3+} [160]. The asymmetric band shape with maximum at 258 nm is due to the fact, that it is overlapped with the absorption of host. Another part is in the spectral range from 400 to 520 nm with several sharp peaks, which are attributed to 4f – 4f transition of Pr^{3+} ions from ground state $^3H_4$ to excited ^3P_J ($J = 0, 1, 2$) and $^1I_6$ states. [161, 162].

The interconfiguration transition from ground state to 4f5d state is nearly equal in intensity to the 4f intraconfiguration $^3H_4 \rightarrow {}^3P_0$ transition at 496 nm. The emission spectra of Ca_2SnO_4:0.25% Pr^{3+} sample (*Figure 11.4c*) consists of four sharp peaks locating at 604, 622.5, 656 and 718 nm, which can be ascribed to $^1D_2 \rightarrow {}^3H_4$, $^3P_0 \rightarrow {}^3H_6$, $^3P_0 \rightarrow {}^3F_2$ and $^3P_0 \rightarrow {}^3F_4$ transition, respectively.

The emission spectra of Ca_2SnO_4:Pr^{3+} phosphor under different excitation wavelengths are illustrated in *Figure 11.5*. It can be seen that emission intensity is two times stronger when excitation of 310 nm was used. Therefore, the efficiency of UV excitation makes the phosphor more attractive for application in LED sources.

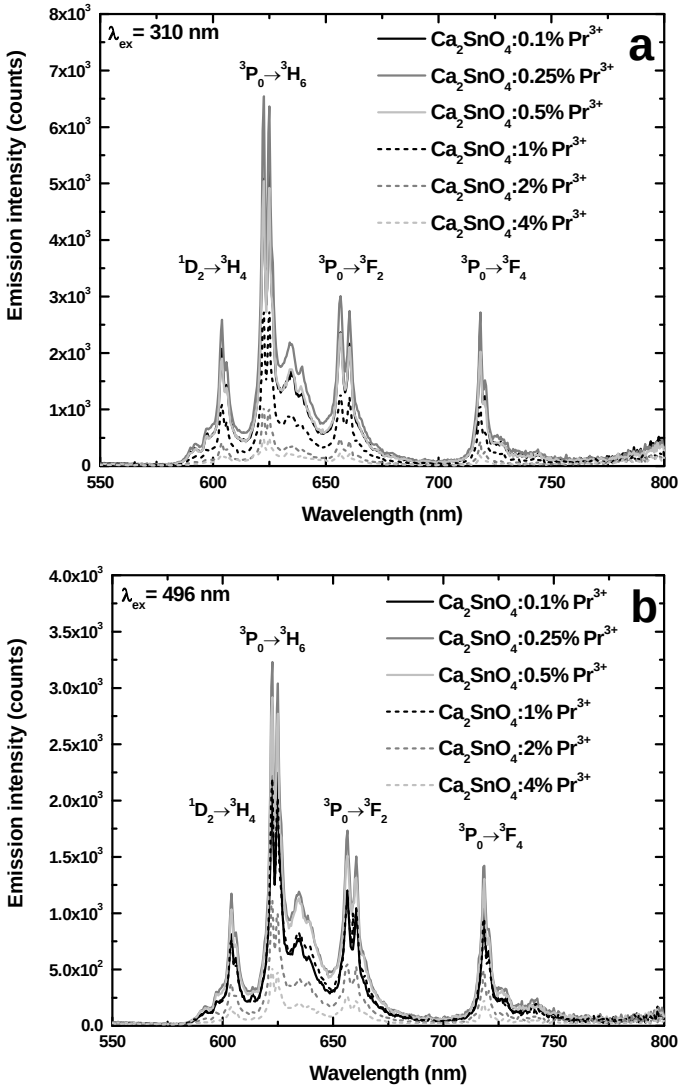

Figure 11.5 *Emission spectra of Ca_2SnO_4 as a function of Pr^{3+} concentration under different excitation wavelengths: (a) 310 nm and (b) 496 nm.*

Reflection spectra of Pr^{3+} doped $SrSnO_3$ sample (*Figure 11.4b*) exhibits a broad absorption band ranging from 250 to 350 nm, which can be attributed to the typical optical response of a wide band gap semiconductor. The band gap value of $SrSnO_3$ reported in literature is 4.1 eV [36].

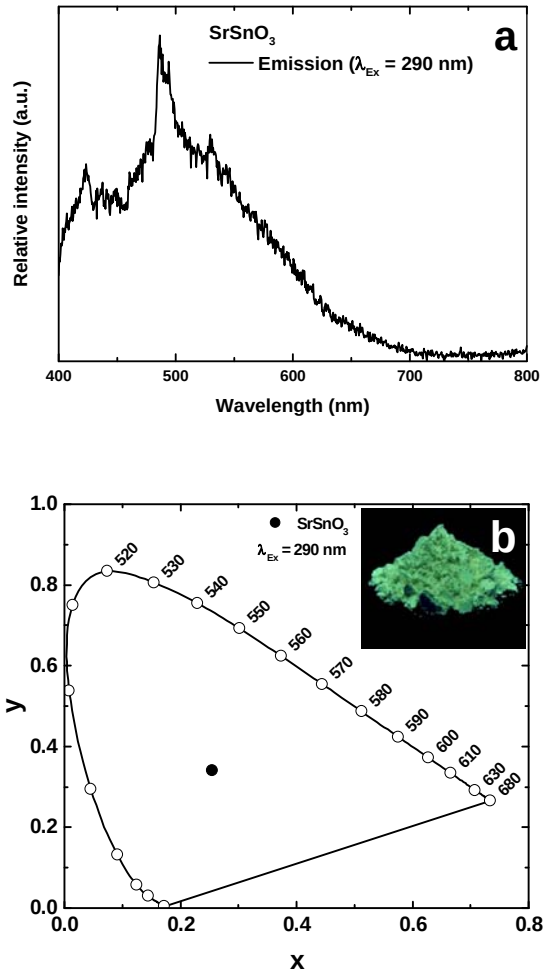

Figure 11.6 *(a) Photoluminescence emission spectra and (b) CIE1931 color diagram with color point of undoped $SrSnO_3$ (the inset picture shows the digital picture of $SrSnO_3$ excited at 254 nm).*

Generally, in polar oxides such as $SrTiO_3$, $BaTiO_3$, and anatase-type TiO_2, the strong coupling between electrons and lattice vibrations can lead to the formation of self-trapped excitons (STEs), whose recombination usually gives rise to a broad band and structureless visible emission with a large Stokes shift [163-165].

The photoluminescence emission spectra of undoped $SrSnO_3$ sample excited at 290 nm is shown in *Figure 11.6a*. It can be seen that the broad spectrum originates from a multiphotonic process, in which several STE states are formed inside the band gap, allowing numerous different energetic transitions among them. As a result, a broad band covering a large part of visible spectra can be observed in $SrSnO_3$ host material [166].

Figure 11.6b represents the CIE color diagram with color point of undoped $SrSnO_3$ under excitation of 290 nm. The calculated *x* and *y* values are 0.254 and 0.340, respectively. The color point is located at the border of green and white regions in CIE chromaticity diagram. The estimated luminous efficacy value for $SrSnO_3$ host is 275 lm/W.

Figure 11.7 shows the emission intensity integrals as a function of Pr^{3+} concentration in alkaline earth meta- and ortho-stannates. The photoluminescence intensity of $CaSnO_3$ sample under excitation of 265 nm rapidly increases up to 2 mol % and then slightly decreases when dopant concentration reaches 4 mol %. The emission intensity integral of $SrSnO_3$:Pr^{3+} phosphor increases steeply in low concentration region up to 1 mol % and then continuously increases up to 4 mol % without reaching the maximum value. The possible explanation for the absence of concentration quenching effect is that solubility limit of Pr^{3+} in $SrSnO_3$ host material was not reached. Dependencies of the emission intensity integral on Pr^{3+} ion concentration in Ca_2SnO_4 host material are following the same trend, when different excitation wavelengths are used. The luminescence intensity increases with Pr^{3+} concentration until a maximum intensity of 0.25 mol % is reached and then the emission intensity declines quickly due to the concentration quenching effect.

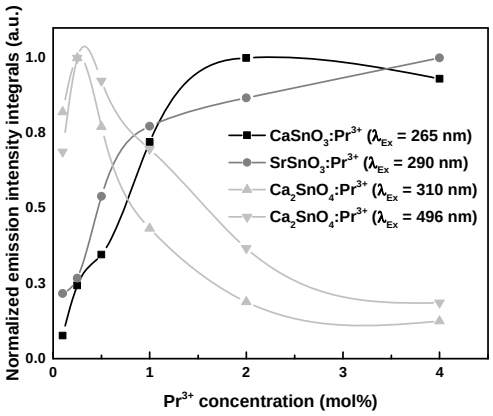

Figure 11.7 *Emission intensity integrals as a function of Pr^{3+} concentration in different alkaline earth stannate phosphors.*

Interesting behavior can be observed in concentration dependent emission spectra of $SrSnO_3:Pr^{3+}$ in 500 to 600 nm region depicted in *Figure 11.8*.

The STE emission intensity increases with increased Pr^{3+} content up to 1 mol %. At the same time the characteristic transition at 528 nm of Pr^{3+} ion starts to appear and increases in intensity. Consequently, $^3P_0 \rightarrow {}^3H_5$ transition becomes prominent while STE emission diminishes, when activator concentration reaches 4 mol %.

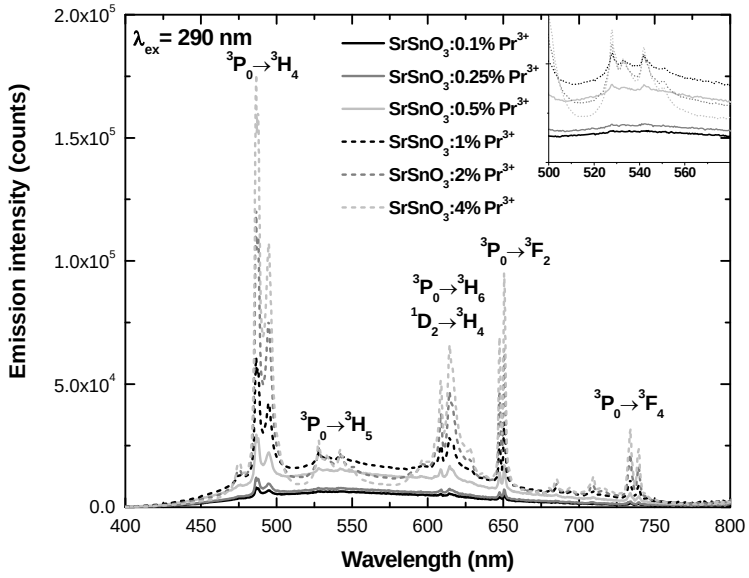

Figure 11.8 *Emission spectra of $CaSnO_3$ as a function of Pr^{3+} concentration.*

Figure 11.9a depicts the thermal quenching data of $CaSnO_3$:1% Pr^{3+} sample under excitation at 265 nm. The total light output increases by 50% in temperature range from 150 to 350 K and then starts to decrease with further temperature increase (*Figure 11.9a*).

The temperature dependent emission intensity integrals of $SrSnO_3$:4% Pr^{3+} excited at 290 nm are depicted in *Figure 11.10a*. Taking into account that integral values have shifted towards lower temperature region by ~100 K, the tendency has remained unchanged.

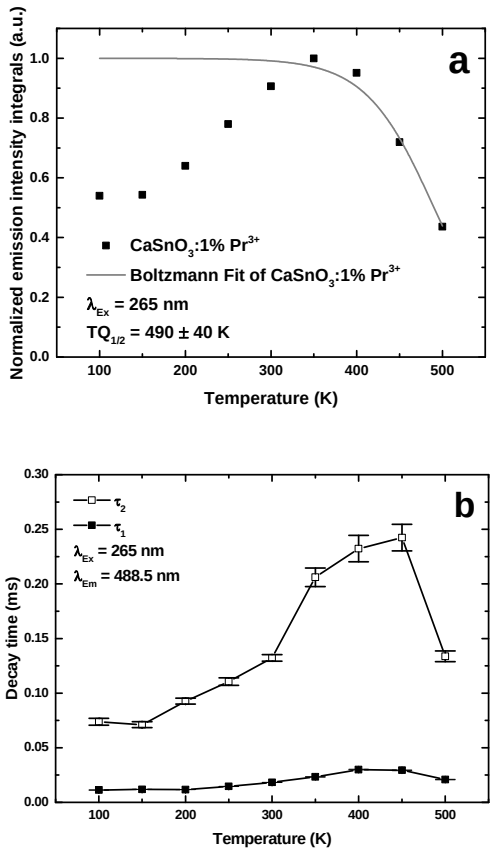

Figure 11.9 *(a) Normalized emission integrals and (b) emission decay values as a function of temperature of the $CaSnO_3$:1% Pr^{3+} sample.*

According to Clabau et al., the trap depth is proportional to the strength of the anion-cation bonds of the host lattice [167]. In $MSnO_3$ phosphors, the trap depth is determined by the strength of M–O bond. Since electronegativity increases in order of Ba < Sr < Ca the strength of M–O bond increases as well. Therefore, the depth of the hole traps should be $Ba^{2+} < Sr^{2+} < Ca^{2+}$. This effect can be observed comparing both temperature dependent emission integrals plotted in *Figure 11.9a* and *Figure 11.10a*.

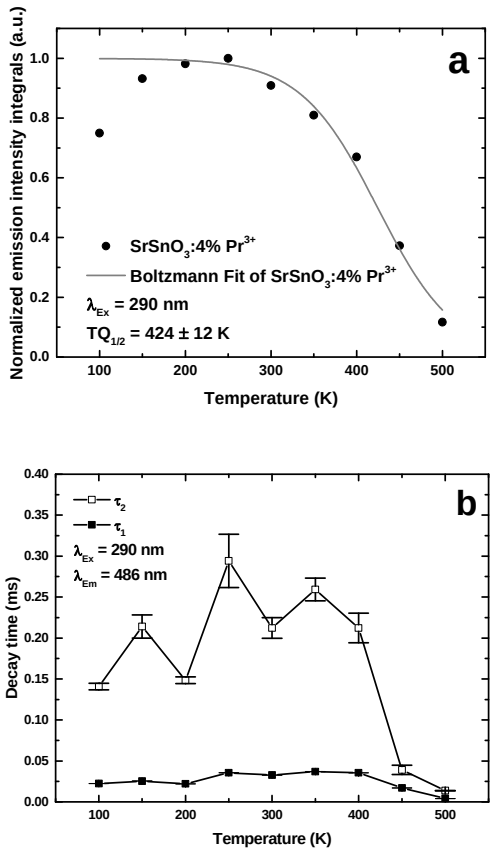

Figure 11.10 *(a) Normalized emission integrals and (b) emission decay values as a function of temperature of the $SrSnO_3$:4% Pr^{3+} sample.*

The energy stored within the host is being released most efficiently in $CaSnO_3$:1% Pr^{3+} and $SrSnO_3$:4% Pr^{3+} phosphors at 350 and 250 K, respectively. A Boltzmann fit was applied to calculate $TQ_{1/2}$ value. The fit resulted in $TQ_{1/2}$ values with greater error for $CaSnO_3$:1% Pr^{3+} sample (490±40 K) than those for $SrSnO_3$:4% Pr^{3+} (424±12 K). The temperature dependent decay curves of $CaSnO_3$:1% Pr^{3+} and $SrSnO_3$:4% Pr^{3+} phosphors were fitted by a bi-exponential decay function. The decay time value τ_2 of $CaSnO_3$:1% Pr^{3+} sample gradually increases until reaches maximum value of 0.24 ms at 450 K and then abruptly decreases upon an increase in

temperature (*Figure 11.9b*). Temperature dependent decay time values of $SrSnO_3$:4% Pr^{3+} sample are plotted in *Figure 11.10b*. If we exclude two anomaly points at 150 and 250 K then both decay time values would increase following the same trend and fall into 0.25 ms region, as in $CaSnO_3$:1% Pr^{3+} sample. Moreover, the maximum τ_2 value would be located at 350 K, which is shifted toward lower temperature region by 100 K comparing with $CaSnO_3$:1% Pr^{3+} sample. These maximum values are about 100 K higher than the ones obtained from temperature dependent emission integrals shown in *Figure 11.9a* and *Figure 11.10a*. This indicates that the internal efficiency (proportional to decay times) of Pr^{3+} ion decreases slower than its external efficiency (proportional to internal efficiency and escape efficiency). Hence, the thermal quenching is caused either by decreased escape efficiency or by an increased probability for re-absorption [91].

The enhancement of decay time values at 150 and 250 K in *Figure 11.10b* confirms the existence of structural phase transition in strontium stannate discovered by Singh et al. The transition at 160 K may be second order and is likely to be displacive due to octahedral tilting, while transition near 265 K appears to be an order–disorder one. [22]. To our knowledge only Kotan et al. have reported about anomalies in the PL spectra of $SrSnO_3$:Tb^{3+} compatible with a structural phase transition at 260 K [168].

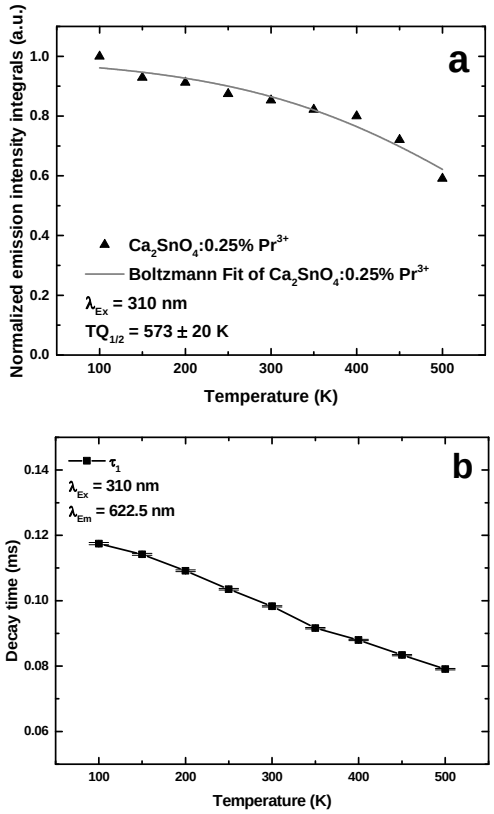

Figure 11.11 *(a) Normalized emission integrals and (b) emission decay values as a function of temperature of the Ca_2SnO_4:0.25% Pr^{3+} sample.*

The temperature dependent emission intensity integrals and lifetime values of Ca_2SnO_4:0.25% Pr^{3+} sample are shown in *Figure 11.11a* and *11.11b*, respectively. It is obvious that photoluminescence integrals decrease if temperature is increased. A Boltzmann sigmoidal fit was used for the calculation of $TQ_{1/2}$ value. The estimated $TQ_{1/2}$ value for Ca_2SnO_4:0.25% Pr^{3+} specimen with greater error (573±20) is due to the fact that emission integrals do not decrease to half of the initial value. The decay time values show analogic tendency that decreases with increasing temperature.

Pr^{3+} concentration dependent decay curves of Pr^{3+}-doped different stannate phosphors are shown in *Figure 11.12*.

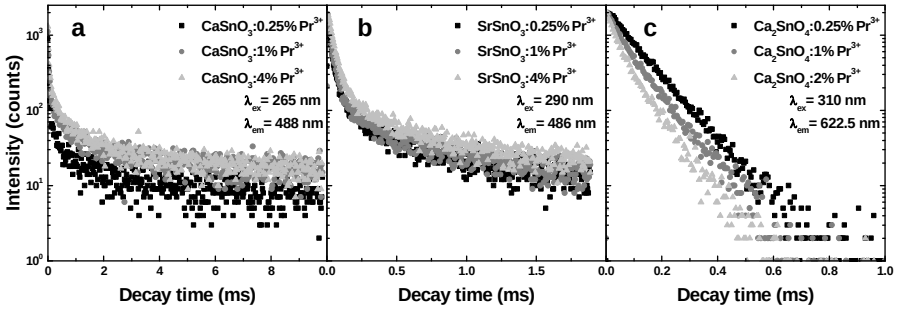

Figure 11.12 *Decay curves of (a) $CaSnO_3:Pr^{3+}$, (b) $SrSnO_3:Pr^{3+}$ and (c) $Ca_2SnO_4:Pr^{3+}$ as a function of Pr^{3+} concentration.*

As seen, the decay curves or decay speed of the samples are quite different from each other, again suggesting different internal efficiency. Especially, the original behavior of decay speed is observed for $Ca_2SnO_4:Pr^{3+}$ phosphor.

*Figure 11.13*a, b and c show the chromaticity coordinates of $CaSnO_3:Pr^{3+}$, $SrSnO_3:Pr^{3+}$ and $Ca_2SnO_4:Pr^{3+}$ samples, respectively. With increasing Pr^{3+} concentration, the *x* values show an increasing trend and the *y* values show a decreasing trend. However, comparing three host materials with each other, in concentration range from 0.1 to 4 mol % of Pr^{3+}, the color points are shifted for different matrices.

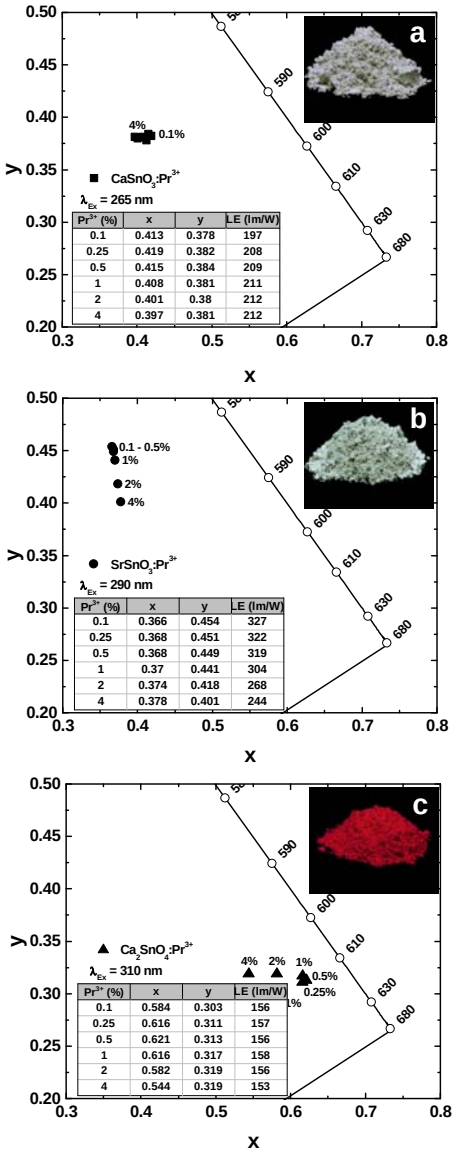

Figure 11.13 *CIE1931 color points of: (a) $CaSnO_3:Pr^{3+}$, (b) $SrSnO_3:Pr^{3+}$, and (c) $Ca_2SnO_4:Pr^{3+}$ with different Pr^{3+} concentrations. Exact color points and LE values for each Pr^{3+} concentration are given in inset tables. The inset pictures shows the digital pictures of the respective compounds excited at 254 nm.*

The enhancement of decay time values at 150 and 250 K in $SrSnO_3:Pr^{3+}$ phosphor can be attributed to the cryogenic phase transition in strontium stannate. Singh et al. proposed that such low temperature transitions were not predicted and are unexpected for this perovskite, indicating the need for further study of $SrSnO_3$ at low temperatures, by additional structural methods [22]. Therefore, temperature dependent fluorescence lifetime measurements are particularly suitable for monitoring phase transition of optically active materials.

Chapter 12. Impedance Spectroscopy of $BaSnO_3$ and Ba_2SnO_4

Impedance spectroscopy (IS) is the measurement of electrical impedance, admittance, or some other closely related quantity as a function of frequency. It is characterized by the interaction of an external field with the electric dipole moment of the sample, often expressed by permittivity. This technique is used to resolve processes of electrical polarization according to their relaxation frequencies or time constants. The technique can be used to characterize ionic or electronic conductors as well as dielectric materials. It is commonly applied to electroceramics, solid electrolytes, dielectrics, including polymers and glasses, and to integrated energy conversion devices such as batteries and fuel cells [169].

In polycrystalline solids, polarizations arise as a result of the lower electrical conductivity of the grain boundaries in comparison to the grain core. In this case, the polarizations of the two regions appear as distinct features in the impedance spectrum [169]. The brick layer model (BLM) has been used to describe the electrical properties of polycrystalline electroceramics for more than 40 years [170]. This model showed the ability to discriminate grain boundary versus grain core behavior and relative simplicity of interpretation (e.g., for extracting activation energies for grain versus grain core boundary transport). However, there are certain limitations to the BLM. It is applicable at the microscale but inappropriate for characterizing electroceramics at the nanoscale. For example, without independent knowledge of the grain boundary ‘‘width,’’ it is impossible to extract reliable grain boundary properties (conductivity, dielectric constant) from impedance spectra. Furthermore, most BLMs fail in the nanoregime, where grain boundary widths become comparable in size to the grain core.

For that reason, a new nano-grain composite model (n-GCM) was developed by Mason et al [171]. The method appears to be applicable only at nanograin sizes (10-100 nm).

The luminescent properties of Ba_2SnO_4 doped with Sm^{3+} and Eu^{3+} showed exceptional behavior at low temperature range (100-500 K). It was interesting to know, if this structure has any phase transitions at higher temperatures. For that reason dielectric and impedance spectroscopy studies of barium stannate ($BaSnO_3$) and barium ortho-stannate (Ba_2SnO_4) were performed.

As we can see from *Figure 12.1* and *Figure 12.2*, dielectric spectra of $BaSnO_3$ and Ba_2SnO_4 are dominated by conductivity in whole investigated temperature range, and no dielectric anomalies are observed.

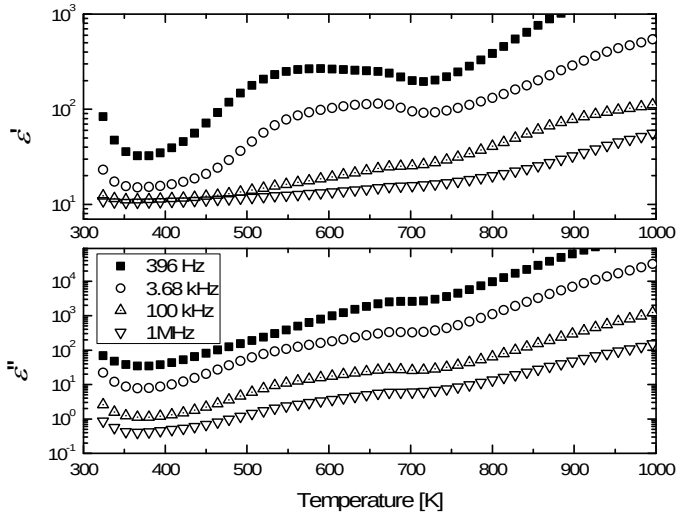

Figure 12.1 *Temperature dependence of real and imaginary parts of complex dielectric permittivity of $BaSnO_3$.*

At low temperatures an increase in conductivity is observed on cooling in 320 K – 400 K temperature range. This is most likely related to humidity-induced conductivity in the sample, as material is not hydrophobic and is highly porous due to nanostructured nature. At high temperatures humidity of air is relatively low, and dielectric losses are dominated by material's conductivity. At temperatures below 400 K humidity influences measured impedance a lot. This fact is known for $BaSnO_3$, as it is a good humidity sensor material [172]. Apparently, Ba_2SnO_4 is a good sensor material, too.

Figure 12.3 and *Figure 12.4* show frequency dependencies of specific impedance of both ceramics. The important difference between the materials is that there are two processes observable in $BaSnO_3$ at temperature below 700 K, with the high frequency process disappearing from the spectra due to frequency limitations of the experiment.

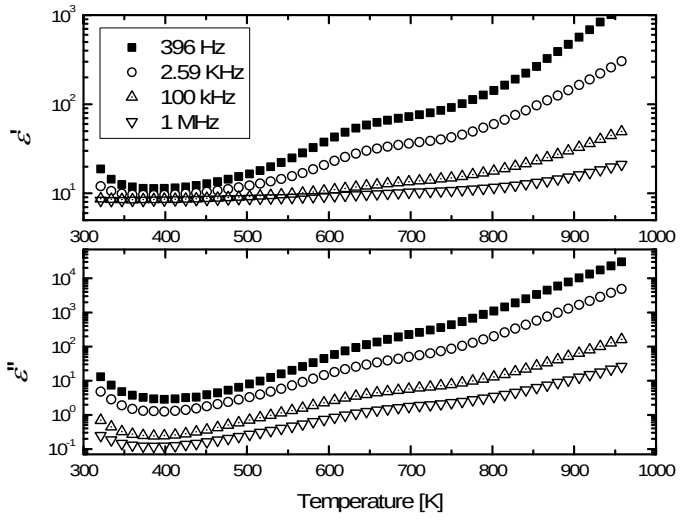

Figure 12.2 *Temperature dependence of real and imaginary parts of complex dielectric permittivity of Ba_2SnO_4.*

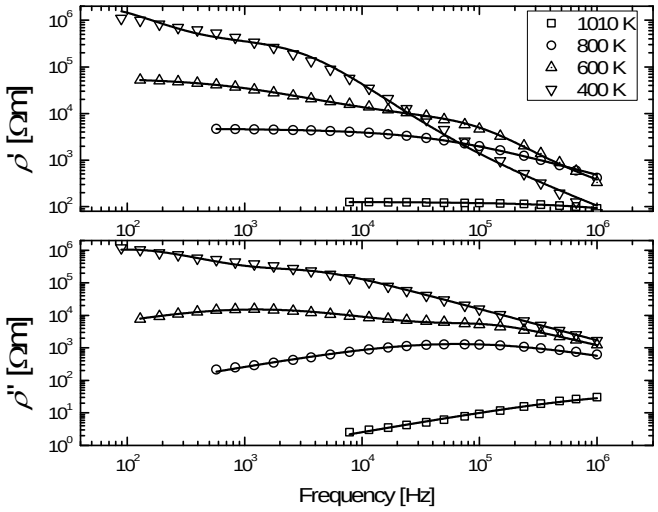

Figure 12.3 *Frequency dependence of real and imaginary parts of specific impedance of $BaSnO_3$.*

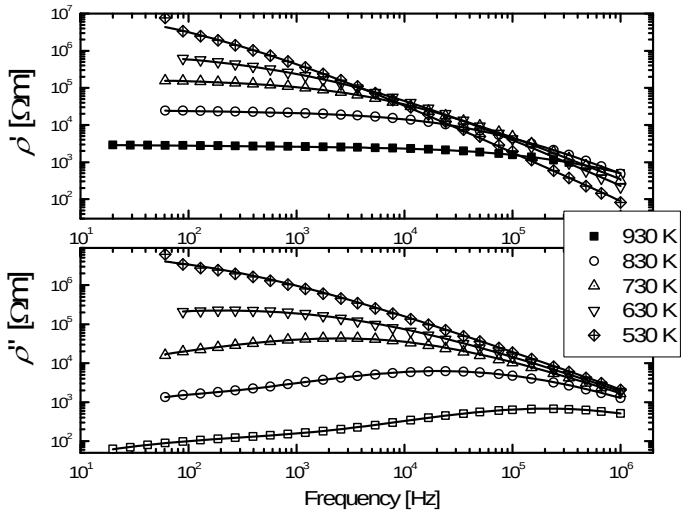

Figure 12.4 *Frequency dependence of real and imaginary parts of specific impedance of Ba_2SnO_4.*

We argue that the low-frequency process is due to inter-grain charge relaxation, while high frequency process is due to relaxation inside grains of the ceramics. On the other hand, there is only one process observed in Ba_2SnO_4 besides very high temperatures (> 800 K), when at low frequencies a second process appears.

Frequencies of maxima in imaginary part of impedances correspond to reciprocal relaxation times. We can see from frequency dependencies, that the higher the temperature, the shorter the time. This is likely related to decrease of resistivity at higher temperatures.

Chapter 13. Conclusions

The first part of this thesis is focused on synthesis of alkaline earth metal stannates applying four different synthesis routes: gel to crystallite, sol-gel, sol-gel combustion and solid state reaction. The second part of this thesis deals with luminescent properties of Sm^{3+}, Eu^{3+} and Pr^{3+} doped alkaline earth metal stannates.

Each method showed its own advantages and disadvantages. For instance, the results presented in **Chapter 6** demonstrated the potential of novel synthetic approach based on the gel to crystallite conversion (G-C) method to yield phase-pure strontium stannate ($SrSnO_3$), strontium titanate ($SrTiO_3$) and mixed strontium stannate titanate ($SrSn_{1-x}Ti_xO_3$) powders at low crystallization temperature (800 °C). Such temperature is very low as compared to the temperature required for solid state synthesis. The morphological characterization of $SrSnO_3$ by scanning electron microscopy showed the formation of nearly rod, stick or needle-type crystallites. The crystal width and length vary from 500 nm to 3 μm and from 10 to 40 μm, respectively. However, in standard synthesis procedure freshly prepared $SnO_2 \cdot xH_2O$ gel should be repeatedly washed with cold distilled water in order to eliminate chloride ions. During this step the part of the gel is washed out resulting in poor stoichiometry control of the final product. Moreover, XRD analysis revealed that elimination of remaining chloride ions lead to the reduction of tin at higher temperatures. Due to this process, tin oxide is observed as a secondary phase in the synthesis product.

For that reason a novel and inexpensive water based synthesis route for the preparation of a chloride-free citrato peroxo Sn(IV) precursor solution was developed and systematically investigated in **Chapter 7**. The gel precursor was successfully applied for the preparation of SnO_2 thin films on

a Si/SiO_2 substrate. The XRD analysis showed that all diffraction lines of sol-gel derived films obtained at 400 ^oC corresponded to monophasic cassiterite-type crystalline SnO_2. SEM micrographs clearly showed the formation of dense and uniform SnO_2 films. The citrato peroxo Sn(IV) precursor can be regarded as a reliable source for deposition of compact layers with controllable thickness of the film.

We have demonstrated, that citrato peroxo Sn(IV) precursor can be successfully applied for the preparation of ternary metal oxide powders (**Chapter 8**). A novel sol-gel (combustion) synthesis route for the preparation of monophasic alkaline earth metal stannates has been developed. Calcium, strontium and barium meta-stannates and ortho-stannates were synthesized by means of environmentally friendly an aqueous sol-gel technique. Strontium and barium stannate ($SrSnO_3$, Sr_2SnO_4, $BaSnO_3$, Ba_2SnO_4) powders were prepared under neutral conditions in the sol-gel processing. However, the successful synthesis of appropriate calcium stannates ($CaSnO_3$ and Ca_2SnO_4) could be performed only at acidic sol-gel combustion processing conditions. It was established, that monophasic alkaline earth metal meta-stannates ($MSnO_3$) could be obtained at 800 °C. On the other hand, for the preparation of monophasic alkaline earth metal ortho-stannates (M_2SnO_4) slightly higher annealing temperature (1000 °C) should be used.

The SEM characterization of synthesized powders let us to conclude, that the main morphological features of different calcium, strontium and barium stannates are dependent on the chemical composition of synthesized compounds (nature of alkaline earth metal, meta- or ortho- polymorphs).

Finally, $CaSnO_3$ and Ca_2SnO_4 are composed of continuous porous network due to the release of a large amount of gases during combustion process. Besides, $CaSnO_3$ and Ca_2SnO_4 crystallites within nanometer size range have formed during suggested sol-gel combustion route.

The photoluminescence properties of $Ca_2SnO_4:Sm^{3+}$, $Sr_2SnO_4:Sm^{3+}$ and $Ba_2SnO_4:Sm^{3+}$ samples were investigated in **Chapter 9**. For $Ca_2SnO_4:Sm^{3+}$ phosphor the strongest emission peaks were observed in the red region of the visible spectrum (616 nm and 646 nm). However, the most intensive emission band of $Sr_2SnO_4:Sm^{3+}$phosphor is located at 646 nm and corresponds to the $^4G_{5/2} \rightarrow {}^6H_{9/2}$ transition. The energy level splitting effect is observed clearly in the emission spectra of $Ba_2SnO_4:Sm^{3+}$ sample. Based on the obtained results we demonstrate that Sm^{3+} ions occupy Ca and Sr sites in the Ca_2SnO_4 and Sr_2SnO_4 ortho-stannate structures, respectively. In contrast, Sm^{3+} substitutes Sn in the barium ortho-stannate Ba_2SnO_4 structure.

The decay times for $Ca_2SnO_4:Sm^{3+}$ and $Sr_2SnO_4:Sm^{3+}$ get shorter with higher activator concentration. This can be related with faster energy transfer process between Sm^{3+} ions. However, the decay curves of $Ba_2SnO_4:Sm^{3+}$ are nearly identical, suggesting similar internal efficiency of Sm^{3+} ions at all concentrations. The color points in chromaticity diagram are shifted towards lower x values (from red to orange region) in sequence Ca → Sr → Ba.

The photoluminescence properties of $Ca_2SnO_4:Eu^{3+}$, $Sr_2SnO_4:Eu^{3+}$ and $Ba_2SnO_4:Eu^{3+}$ samples were investigated in **Chapter 10**. The diffuse reflectance spectra of each compound, recorded in the spectral region from

250 to 800 nm, exhibits a strong broad absorption band in the UV region. The dominant emission peak for $Ca_2SnO_4:Eu^{3+}$ is situated at 616 nm and shows a prominent and bright red light due to $^5D_0 \rightarrow {}^7F_2$ electric dipole transition. The intensive peak assigned to $^5D_0 \rightarrow {}^7F_0$ transition was observed in all europium doped Sr_2SnO_4 samples. A strong emission peak due to the magnetic dipole transition $^5D_0 \rightarrow {}^7F_1$ was observed at 593 nm for Ba_2SnO_4 doped with Eu^{3+}, which confirms that Eu^{3+} occupies the sites of Sn^{4+}.

The decay curves or decay speed of the $M_2SnO_4:Eu^{3+}$ samples differ from each other, thus suggesting about different internal efficiency of activator ion. The results obtained demonstrated that these phosphors had different decay times, which indicates the creation of different depth of trapping energy levels in $M_2SnO_4:Eu^{3+}$. With increasing Eu^{3+} concentration, the *x* values in chromaticity diagram show an increasing trend and the *y* values show a decreasing trend. The color points are shifted towards lower x values (from red to orange region) in sequence Ca → Sr → Ba.

The photoluminescence properties of $CaSnO_3:Pr^{3+}$, $SrSnO_3:Pr^{3+}$ and $Ca_2SnO_4:Pr^{3+}$ samples were investigated in **Chapter 11**. The emission spectrum of Pr^{3+} doped $CaSnO_3$ sample consists of five major emission lines peaking at around 488, 530, 613, 656 and 742 nm are assigned to the f-f transitions of $^3P_0 \rightarrow {}^3H_4$, $^3P_0 \rightarrow {}^3H_5$, $^1D_2 \rightarrow {}^3H_4$, $^3P_0 \rightarrow {}^3F_2$ and $^3P_0 \rightarrow {}^3F_4$ states of Pr^{3+} ions, respectively. The emission spectra of $SrSnO_3:Pr^{3+}$ phosphor was quite similar to $CaSnO_3: Pr^{3+}$ sample. The most intensive emission peaks are located in the green (500 nm), orange (600 nm) and red (660 nm) spectral region. The emission spectra of $Ca_2SnO_4:Pr^{3+}$ phosphor under different excitation wavelengths illustrated, that the efficiency of UV

excitation makes the phosphor more attractive for application in LED sources.

The decay curves or decay speed of the samples are quite different from each other, again suggesting different internal efficiency. Especially, the original behavior of decay speed is observed for $Ca_2SnO_4:Pr^{3+}$ phosphor. With increasing Pr^{3+} concentration, the *x* values in the chromaticity coordinates show an increasing trend and the *y* values show a decreasing trend. By comparing three host materials with each other, in concentration range from 0.1 to 4 mol % of Pr^{3+}, the color points are shifted for different matrices.

Dielectric and impedance spectroscopy studies of barium stannate ($BaSnO_3$) and barium ortho-stannate (Ba_2SnO_4) were performed (**Chapter 12**). The experimental results showed that both materials do not exhibit any dielectric anomalies in 300 – 1000 K temperature range. Both materials are sensitive to humidity of air. $BaSnO_3$ showed two charge transfer processes in 20 Hz–1 MHz frequency and 300 – 700 K temperature ranges.

Chapter 14. List of Publications and Conference Participation

Articles in Journals

1. A. Stanulis, A. Selskis, R. Ramanauskas, A. Beganskiene and A. Kareiva. Low temperature synthesis and characterization of strontium stannate titanate ceramics. *Mater. Chem. Phys.,* **130** (2011) 1246-1250.
2. A. Stanulis, A. Hardy, C. De Dobbelaere, J. D'Haen, M. Van Bael and A. Kareiva. SnO_2 thin films from an aqueous citrate peroxo Sn(IV) precursor. *J. Sol-Gel Sci. Technol.,* **62** (2012) 57-64.
3. A. Stanulis, S. Sakirzanovas, M. Van Bael and A. Kareiva. Sol-gel (combustion) synthesis and characterization of different alkaline earth metal (Ca, Sr, Ba) stannates. *J. Sol-Gel Sci. Technol.,* **64** (2012) 643-652.
4. A. Stanulis, A. Katelnikovas, D. Enseling, D. Dutczak, S. Šakirzanovas, M. Van Bael, A. Hardy, A. Kareiva and T. Juestel. Luminescence properties of Sm^{3+}-doped alkaline earth ortho-stannates. *Opt. Mater.,* Submitted (2013).
5. R. M. Katiliute, P. Seibutas, M. Ivanov, R. Grigalaitis, A. Stanulis, J. Banys and A. Kareiva. Dielectric and impedance spectroscopy of $BaSnO_3$ and Ba_2SnO_4. *Ferroelectrics,* Submitted (2013).

Published contributions to academic conferences

1. A. Stanulis, A. Hardy, S. Sakirzanovas, J. D'Haen, M. Van Bael and A. Kareiva. SnO_2 thin film deposition and synthesis of alkaline earth metal stannates from an aqueous citrate peroxo Sn(IV) precursor. International Conference of Young Chemists "Nanochemistry and Nanomaterials". Palanga, Lithuania, December 7-9, (2012) 45.
2. A. Stanulis, A. Hardy, J. D'Haen, M. Van Bael and A. Kareiva. Synthesis of SnO_2 thin films and $SrSnO_3$ ceramics based on aqueous citratoperoxo-Sn(IV) precursor. E-MRS 2011 Fall Meeting. Warsaw, Poland, 19-23 September, (2011) X4.
3. A. Stanulis, A. Beganskiene and A. Kareiva. Soft chemistry method for preparation of strontium titanate and stannate. 11-th International Conference-School "Advanced Materials and Technologies". Palanga, Lithuania, August 27-31, (2009) 92.
4. A. Stanulis, A. Beganskiene and A. Kareiva. Synthesis and characterization of strontium titanate and stannate. Conference "Chemistry and Technology of Inorganic Compounds". Kaunas, Lithuania, April 22, (2009) 7.
5. A. Stanulis, A. Beganskiene, A. M. Klonkowski and A. Kareiva. A chimie douce route to nanostructured $SrTiO_3$. Int. Baltic Sea Region Conf. "Functional Materials and Nanotechnologies 2009". Riga, Latvia, March 31 - April 3, (2009) 165.

Chapter 15. References

[1] T. Minami, Thin Solid Films, 516 (2008), pp. 1314-1321.
[2] S. Shanthi, C. Subramanian, P. Ramasamy, J. Cryst. Growth, 197 (1999), pp. 858-864.
[3] A.L. Santos, D. Profeti, P. Olivi, Electrochim Acta, 50 (2005), pp. 2615-2621.
[4] P. Montmeat, C. Pijolat, G. Tournier, J.P. Viricelle, Sens. Actuator B-Chem., 84 (2002), pp. 148-159.
[5] M. Batzill, U. Diebold, Prog Surf Sci, 79 (2005), pp. 47-154.
[6] D.M. Mukhamedshina, N.B. Beisenkhanov, Advances in Crystallization Processes, Dr. Yitzhak Mastai (Ed.), (2012).
[7] L.M. Li, X.M. Yin, S.A. Liu, Y.G. Wang, L.B. Chen, T.H. Wang, Electrochem Commun, 12 (2010), pp. 1383-1386.
[8] J. Jeong, S.P. Choi, C.I. Chang, D.C. Shin, J.S. Park, B.T. Lee, Y.J. Park, H.J. Song, Solid State Commun, 127 (2003), pp. 595-597.
[9] G. Sberveglieri, G. Faglia, S. Groppelli, P. Nelli, Sensor Actuat B-Chem, 8 (1992), pp. 79-88.
[10] B. Thangaraju, Thin Solid Films, 402 (2002), pp. 71-78.
[11] C. Terrier, J.P. Chatelon, J.A. Roger, Thin Solid Films, 295 (1997), pp. 95-100.
[12] J.P. Chatelon, C. Terrier, E. Bernstein, R. Berjoan, J.A. Roger, Thin Solid Films, 247 (1994), pp. 162-168.
[13] J. Heo, A.S. Hock, R.G. Gordon, Chem Mater, 22 (2010), pp. 4964-4973.
[14] M.A. Dal Santos, A.C. Antunes, C. Ribeiro, C.P.F. Borges, S.R.M. Antunes, A.J. Zara, S.A. Pianaro, Mater Lett, 57 (2003), pp. 4378-4381.
[15] C.J. Brinker, G.W. Scherer, Sol-gel science : the physics and chemistry of sol-gel processing, Academic Press, Boston, 1990.
[16] R.W. Schwartz, T. Schneller, R. Waser, Cr Chim, 7 (2004), pp. 433-461.
[17] G. Gordillo, L.C. Moreno, W. de la Cruz, P. Teheran, Thin Solid Films, 252 (1994), pp. 61-66.
[18] B. Benrabah, A. Bouaza, A. Kadari, M.A. Maaref, Superlattices and Microstructures, 50 (2011), pp. 591-600.
[19] M. Epifani, M. Alvisi, L. Mirenghi, G. Leo, P. Siciliano, L. Vasanelli, J Am Ceram Soc, 84 (2001), pp. 48-54.
[20] T.J. Liu, Z.G. Jin, L.R. Feng, T. Wang, Applied Surface Science, 254 (2008), pp. 6547-6553.
[21] J.R. Zhang, L. Gao, J Solid State Chem, 177 (2004), pp. 1425-1430.
[22] M.K. Singh, J.W. Hong, N.K. Karan, H.M. Jang, R.S. Katiyar, S.A.T. Redfern, J.F. Scott, J Phys-Condens Mat, 22 (2010).
[23] P. Singh, B.J. Brandenburg, C.P. Sebastian, S. Singh, D. Kumar, O. Parkash, Jpn. J. Appl. Phys., 47 (2008), pp. 3540-3545.
[24] S.W. Tao, F. Gao, X.Q. Liu, O.T. Sorensen, Sens. Actuator B-Chem., 71 (2000), pp. 223-227.

[25] J. Cerda, J. Arbiol, G. Dezanneau, R. Diaz, J.R. Morante, Sens. Actuator B-Chem., 84 (2002), pp. 21-25.
[26] H. Cheng, Z.G. Lu, Solid State Sci, 10 (2008), pp. 1042-1048.
[27] N. Sharma, K.M. Shaju, G.V.S. Rao, B.V.R. Chowdari, J Power Sources, 139 (2005), pp. 250-260.
[28] Y. Sharma, N. Sharma, G.V.S. Rao, B.V.R. Chowdari, Chem Mater, 20 (2008), pp. 6829-6839.
[29] S. Zhao, Y. Bai, W.F. Zhang, Electrochim Acta, 55 (2010), pp. 3891-3896.
[30] C. Li, Y.Q. Zhu, S.M. Fang, H.X. Wang, Y.H. Gui, L. Bi, R.F. Chen, J Phys Chem Solids, 72 (2011), pp. 869-874.
[31] M. Mouyane, M. Womes, J.C. Jumas, J. Olivier-Fourcade, P.E. Lippens, J Solid State Chem, 184 (2011), pp. 2877-2886.
[32] P.H. Borse, J.S. Lee, H.G. Kim, J Appl Phys, 100 (2006).
[33] P.H. Borse, U.A. Joshi, S.M. Ji, J.S. Jang, J.S. Lee, E.D. Jeong, H.G. Kim, Appl Phys Lett, 90 (2007).
[34] Y.P. Yuan, J. Lv, X.J. Jiang, Z.S. Li, T. Yu, Z.G. Zou, J.H. Ye, Appl Phys Lett, 91 (2007).
[35] C.W. Lee, D.W. Kim, I.S. Cho, S. Park, S.S. Shin, S.W. Seo, K.S. Hong, Int J Hydr Energy, (2012).
[36] W.F. Zhang, J.W. Tang, J.H. Ye, Chem Phys Lett, 418 (2006), pp. 174-178.
[37] D. Chen, J.H. Ye, Chem Mater, 19 (2007), pp. 4585-4591.
[38] B. Bellal, B. Hadjarab, A. Bouguelia, M. Trari, Theor Exp Chem+, 45 (2009), pp. 172-179.
[39] V. Thangadurai, P.S. Beurmann, W. Weppner, Mat Sci Eng B-Solid, 100 (2003), pp. 18-22.
[40] S. Misra, K.I. Gnanasekar, R.V.S. Rao, V. Jayaraman, T. Gnanasekaran, J Alloys Compd, 506 (2010), pp. 285-292.
[41] Y. Li, H. Zhang, B. Guo, M. Wei, Electrochim Acta, 70 (2012), pp. 313-317.
[42] W.T. Fu, D. Visser, D.J.W. Ijdo, J Solid State Chem, 169 (2002), pp. 208-213.
[43] A. Novinrooz, P. Sarabadani, Y. Rezainik, Iran J Chem Chem Eng, 28 (2009), pp. 113-119.
[44] A.M. Azad, M. Hashim, S. Baptist, A. Badri, A.U. Haq, J Mater Sci, 35 (2000), pp. 5475-5483.
[45] Z.G. Lu, J.F. Liu, Y. Tang, Y.D. Li, Inorg Chem Commun, 7 (2004), pp. 731-733.
[46] W.S. Lu, H. Schmidt, J Eur Ceram Soc, 25 (2005), pp. 919-925.
[47] W.S. Lu, H. Schmidt, Adv Powder Technol, 19 (2008), pp. 1-12.
[48] A.S. Deepa, S. Vidya, P.C. Manu, S. Solomon, A. John, J.K. Thomas, J Alloys Compd, 509 (2011), pp. 1830-1835.
[49] S.M. Wang, M.K. Lu, G.J. Zhou, Y.Y. Zhou, A.Y. Zhang, Z.S. Yang, J Alloys Compd, 432 (2007), pp. 265-268.
[50] M.C.F. Alves, S.C. Souza, S.J.G. Lima, E. Longo, A.G. Souza, I.M.G. Santos, J Therm Anal Calorim, 87 (2007), pp. 763-766.

[51] C.P. Udawatte, M. Kakihana, M. Yoshimura, Solid State Ionics, 128 (2000), pp. 217-226.
[52] W.S. Lu, H. Schmidt, Ceram Int, 34 (2008), pp. 645-649.
[53] H. Jena, K.V.G. Kutty, T.R.N. Kutty, Mater Chem Phys, 88 (2004), pp. 167-179.
[54] J. Cerda, J. Arbiol, R. Diaz, G. Dezanneau, J.R. Morante, Mater Lett, 56 (2002), pp. 131-136.
[55] G. Pfaff, Mat Sci Eng B-Solid, 33 (1995), pp. 156-161.
[56] G. Pfaff, J Mater Sci, 35 (2000), pp. 3017-3021.
[57] J. Ahmed, C.K. Blakely, S.R. Bruno, V.V. Poltavets, Mater Res Bull, (2012).
[58] B.L. Cushing, V.L. Kolesnichenko, C.J. O'Connor, Chem Rev, 104 (2004), pp. 3893-3946.
[59] J.D. Mackenzie, E.P. Bescher, Accounts Chem Res, 40 (2007), pp. 810-818.
[60] A. Kareiva, Mater Sci-Medzg, 17 (2011), pp. 428-437.
[61] C.J. Brinker, G.W. Scherer, Sol-gel science: the physics and chemistry of sol-gel processing, Academic Press1990.
[62] K.N. Kim, H.-K. Jung, H.D. Park, D. Kim, J Lumin, 99 (2002), pp. 169-173.
[63] Q.Y. Zhang, K. Pita, W. Ye, W.X. Que, Chem Phys Lett, 351 (2002), pp. 163-170.
[64] R.C. Ropp, Luminescence and the Solid State, Elsevier Science2004.
[65] H.M. Yang, J.X. Shi, M.L. Gong, J Solid State Chem, 178 (2005), pp. 917-920.
[66] T. Yamashita, K. Ueda, J Solid State Chem, 180 (2007), pp. 1410-1413.
[67] H.M. Yang, J.X. Shi, M.L. Gong, J Alloys Compd, 415 (2006), pp. 213-215.
[68] Y. Jin, Y. Hu, L. Chen, X. Wang, G. Ju, Z. Mu, J Lumin, 138 (2013), pp. 83-88.
[69] B. Lei, H. Zhang, W. Mai, S. Yue, Y. Liu, S.-q. Man, Solid State Sci, 13 (2011), pp. 525-528.
[70] X. Yu, X.H. Xu, J.B. Qiu, Mater Res Bull, 46 (2011), pp. 627-629.
[71] Y. Lin, Z. Tang, Z. Zhang, Mater Lett, 51 (2001), pp. 14-18.
[72] T. Matsuzawa, Y. Aoki, N. Takeuchi, Y. Murayama, Journal of The Electrochemical Society, 143 (1996), pp. 2670-2673.
[73] L. Bing-Fu, Y. Song, Z. Yong-Zhe, L. Ying-Liang, Chinese Physics Letters, 27 (2010), p. 037201.
[74] Y. Li, Y. Wang, Y. Gong, X. Xu, Journal of The Electrochemical Society, 156 (2009), pp. J77-J80.
[75] A.R. West, Solid State Chemistry and Its Applications, Wiley1985.
[76] A.C. Pierre, Introduction to Sol-Gel Processing, Springer US1998.
[77] L.C. Klein, Sol-Gel technology for thin films, fibers, preforms, electronics, and specialty shapes, Noyes Publications1988.
[78] A.J. Burggraaf, L. Cot, Fundamentals of inorganic membrane science and technology [electronic resource], Elsevier Science & Technology Books1996.
[79] M. Airimioaei, C.E. Ciomaga, N. Apostolescu, L. Leontie, A.R. Iordan, L. Mitoseriu, M.N. Palamaru, J Alloys Compd, 509 (2011), pp. 8065-8072.

[80] A. Hardy, M.K. Van Bael, Nature materials, 10 (2011), pp. 340-341.
[81] A. Sutka, G. Mezinskis, Front. Mater. Sci., 6 (2012), pp. 128-141.
[82] B.G. Wybourne, Spectroscopic Properties of Rare Earths, Interscience Publishers1965.
[83] L. van Pieterson, Charge Transfer and 4fn ... 4fn-15d Luminescence of Lanthanide Ions, Ph.D. Thesis, Universiteit Utrecht, Faculteit Scheikunde, Debye Instituut2001.
[84] F. Szabadvary, Chapter 73 The history of the discovery and separation of the rare earths, in: Karl A. Gschneidner, Jr., E. LeRoy (Eds.) Handbook on the Physics and Chemistry of Rare Earths, Elsevier1988, pp. 33-80.
[85] P.S. Peijzel, Probing High Energy Levels of Lanthanide Ions: Experiment and Theory, 2004.
[86] G. Bizarri, B. Moine, J Appl Phys, 98 (2005), pp. 113528-113528-113529.
[87] M. Haase, H. Schäfer, Angewandte Chemie International Edition, 50 (2011), pp. 5808-5829.
[88] A.A. Kaminskii, Laser crystals: their physics and properties, Springer1990.
[89] A.A. Kaminskii, Laser & Photonics Reviews, 1 (2007), pp. 93-177.
[90] J.M. Ogieglo, Luminescence and Energy Transfer in Garnet Scintillators, Ph.D. Thesis, University of Utrecht, Utrecht, The Netherlands, 2012.
[91] A. Katelnikovas, Synthesis and Characterization of Luminescent Materials for Solid State Light Sources, Ph.D. Thesis, Vilnius University, Vilnius, Lithuania, 2012.
[92] S. Sakirzanovas, Novel Sm2+/3+ Phosphors as Luminescence Converter for Near UV Radiation, Ph.D. Thesis, Vilnius University, Vilnius, Lithuania, 2011.
[93] B.G. Wybourne, L. Smentek, Optical Spectroscopy of Lanthanides: Magnetic and Hyperfine Interactions, Taylor & Francis2007.
[94] B. Henderson, G.F. Imbusch, Optical Spectroscopy for Inorganic Solids, Oxford University Press, Incorporated1989.
[95] J. Solé, L. Bausa, D. Jaque, An Introduction to the Optical Spectroscopy of Inorganic Solids, Wiley2005.
[96] R. Jaaniso, H. Bill, Physical Review B, 44 (1991), pp. 2389-2392.
[97] G. Blasse, B.C. Grabmaier, Luminescent materials, Springer-Verlag1994.
[98] V.M. Bachmann, Studies on Luminescence and Quenching Mechanisms in Phosphors for Light Emitting Diodes, Ph.D. Thesis, Utrech University, Utrecht, Netherlands, 2007.
[99] D. Dutczak, Eu2+ Activated Persistent Luminescent Materials, Ph.D. Thesis, Debye Institute, University of Utrecht, The Netherlands, 2013.
[100] A.J. Smith, A.J.E. Welch, Acta Crystallographica, 13 (1960), pp. 653-656.
[101] H. Mizoguchi, H.W. Eng, P.M. Woodward, Inorganic chemistry, 43 (2004), pp. 1667-1680.
[102] D.M. Helen, Proceedings of the Physical Society, 58 (1946), p. 133.
[103] A. Vegas, M. Vallet-Regi, J.M. Gonzalez-Calbet, M.A. Alario-Franco, Acta Crystallographica Section B, 42 (1986), pp. 167-172.
[104] T.J. Zhang W., Ye J., J Mater Res, 22 (2007), pp. 1859-1871.

[105] M. Trömel, Z Anorg Allg Chem, 371 (1969), pp. 237-247.
[106] H. Yamane, Y. Kaminaga, S. Abe, T. Yamada, J Solid State Chem, 181 (2008), pp. 2559-2564.
[107] M.A. Green, K. Prassides, P. Day, J.K. Stalick, Journal of the Chemical Society, Faraday Transactions, 92 (1996), pp. 2155-2159.
[108] X. Xu, Y. Wang, W. Zeng, Y. Gong, Journal of The Electrochemical Society, 158 (2011), pp. J305-J309.
[109] Y. Liu, J. Kuang, B. Lei, C. Shi, J Mater Chem, 15 (2005), pp. 4025-4031.
[110] R. Shannon, Acta Crystallographica Section A, 32 (1976), pp. 751-767.
[111] A. Vegas, D.J.M. Bevan, Inorganic 3D Structures, Springer2011.
[112] Y.Z. Wang, E. Bevillon, A. Chesnaud, G. Geneste, G. Dezanneau, The Journal of Physical Chemistry C, 113 (2009), pp. 20486-20492.
[113] Z.-H. Ju, S.-H. Zhang, X.-P. Gao, X.-L. Tang, W.-S. Liu, J Alloys Compd, 509 (2011), pp. 8082-8087.
[114] S. Ahuja, T.R.N. Kutty, Journal of Photochemistry and Photobiology A: Chemistry, 97 (1996), pp. 99-107.
[115] L.C. Bichara, M.V. Fiori Bimbi, C.A. Gervasi, P.E. Alvarez, S.A. Brandán, Journal of Molecular Structure, 1008 (2012), pp. 95-101.
[116] J. Pagnaer, D. Nelis, D. Mondelaers, G. Vanhoyland, J. D'Haen, M.K. Van Bael, H. Van den Rul, J. Mullens, L.C. Van Poucke, J Eur Ceram Soc, 24 (2004), pp. 919-923.
[117] M.K. Van Bael, D. Nelis, A. Hardy, D. Mondelaers, K. Van Werde, J. D'Haen, G. Vanhoyland, H. Van den Rul, J. Mullens, L.C. Van Poucke, F. Frederix, D.J. Wouters, Integr Ferroelectr, 45 (2002), pp. 113-122.
[118] P.F. Smet, A.B. Parmentier, D. Poelman, Journal of The Electrochemical Society, 158 (2011), pp. R37-R54.
[119] A. Katelnikovas, J. Plewa, S. Sakirzanovas, D. Dutczak, D. Enseling, F. Baur, H. Winkler, A. Kareiva, T. Justel, J Mater Chem, 22 (2012), pp. 22126-22134.
[120] S. Marković, M. Mitrić, N. Cvjetićanin, D. Uskoković, J Eur Ceram Soc, 27 (2007), pp. 505-509.
[121] A. Podhorodecki, N. Gaponenko, M. Bański, T. Kim, J. Misiewicz, ECS Transactions, 28 (2010), pp. 81-88.
[122] X. Wei, X. Yao, Materials Science and Engineering: B, 137 (2007), pp. 184-188.
[123] T. Liu, Z. Jin, J. Yang, L. Feng, J Am Ceram Soc, 91 (2008), pp. 1939-1944.
[124] R. Alcantara, F.J.F. Madrigal, P. Lavela, C. Perez-Vicente, J.L. Tirado, J Solid State Electr, 6 (2001), pp. 55-62.
[125] J.C. Mailen, O.K. Tallent, P.C. Arwood, ORNL/TM-7474 (1981).
[126] D.Y. Chung, E.H. Kim, Y.J. Shin, J.H. Yoo, C.S. Choi, J.D. Kim, J Radioanal Nucl Chem Lett, 201 (1995), pp. 495-507.
[127] E.H. Kim, D.K. Chung, J.H. Park, J.H. Yoo, J Nucl Sci Technol, 37 (2000), pp. 601-607.

[128] S. Sladkevich, A.A. Mikhaylov, P.V. Prikhodchenko, T.A. Tripol'skaya, O. Lev, Inorg Chem, 49 (2010), pp. 9110-9112.
[129] A.V. Churakov, S. Sladkevich, O. Lev, T.A. Tripol'skaya, P.V. Prikhodchenko, Inorg Chem, 49 (2010), pp. 4762-4764.
[130] A.V. Kostrikin, F.M. Spiridonov, I.V. Lin'ko, O.V. Kosenkova, R.V. Kuznetsova, L.N. Komissarova, Russ J Inorg Chem+, 52 (2007), pp. 1098-1104.
[131] K. Van Werde, D. Mondelaers, G. Vanhoyland, D. Nelis, M.K. Van Bael, J. Mullens, L.C. Van Poucke, B. Van der Veken, H.O. Desseyn, J Mater Sci, 37 (2002), pp. 81-88.
[132] A. Hardy, K. Van Werde, G. Vanhoyland, M.K. Van Bael, J. Mullens, L.C. Van Poucke, Thermochim Acta, 397 (2003), pp. 143-153.
[133] K. Nakamoto, Infrared and Raman spectra of inorganic and coordination compounds, 4th ed., Wiley, New York, 1986.
[134] A. Wladimirsky, D. Palacios, M.C. D'Antonio, A.C. Gonzalez-Baro, E.J. Baran, Spectrochim Acta A, 77 (2010), pp. 334-335.
[135] T. Becker, S. Ahlers, C. Bosch-v.Braunmühl, G. Müller, O. Kiesewetter, Sensors and Actuators B: Chemical, 77 (2001), pp. 55-61.
[136] N. Barsan, M. Schweizer-Berberich, W. Gopel, Fresenius J. Anal. Chem., 365 (1999), pp. 287-304.
[137] Y.Y. Li, L.H. Xue, L.F. Fan, Y.W. Yan, J Alloys Compd, 478 (2009), pp. 493-497.
[138] A.J. Nathanael, D. Mangalaraj, S.I. Hong, Y. Masuda, Materials Characterization, 62 (2011), pp. 1109-1115.
[139] L. Jiang, W. Liu, A. Wu, J. Xu, Q. Liu, L. Luo, H. Zhang, J Sol-Gel Sci Techn, 61 (2012), pp. 527-533.
[140] Z. Lu, L. Chen, Y. Tang, Y. Li, ChemInform, 36 (2005).
[141] N. Sharma, K.M. Shaju, G.V. Subba Rao, B.V.R. Chowdari, Electrochemistry Communications, 4 (2002), pp. 947-952.
[142] B.F. Lei, H.R. Zhang, W.J. Mai, S. Yue, Y.L. Liu, S.Q. Man, Solid State Sci, 13 (2011), pp. 525-528.
[143] S.L. Fu, T. Yin, F. Chai, Chinese Phys, 16 (2007), pp. 3129-3133.
[144] S. Sakirzanovas, A. Katelnikovas, D. Dutczak, A. Kareiva, T. Jüstel, J Lumin, 131 (2011), pp. 2255-2262.
[145] B. Lei, S.-Q. Man, Y. Liu, S. Yue, Mater Chem Phys, 124 (2010), pp. 912-915.
[146] K. Riwotzki, H. Meyssamy, H. Schnablegger, A. Kornowski, M. Haase, Angewandte Chemie International Edition, 40 (2001), pp. 573-576.
[147] K. Riwotzki, H. Meyssamy, A. Kornowski, M. Haase, The Journal of Physical Chemistry B, 104 (2000), pp. 2824-2828.
[148] V. Pankratov, A.I. Popov, S.A. Chernov, A. Zharkouskaya, C. Feldmann, physica status solidi (b), 247 (2010), pp. 2252-2257.
[149] Y.-C. Chen, Y.-H. Chang, B.-S. Tsai, J Alloys Compd, 398 (2005), pp. 256-260.
[150] P.R. Society, Phosphor Handbook, CRC Press1999.

[151] A.H. Johnstone, Journal of Chemical Technology & Biotechnology, 50 (1991), pp. 294-295.
[152] H.M. Yang, J. Shi, M.L. Gong, J Solid State Chem, 178 (2005), pp. 917-920.
[153] T. Igarashi, M. Ihara, T. Kusunoki, K. Ohno, T. Isobe, M. Senna, Appl Phys Lett, 76 (2000), pp. 1549-1551.
[154] Z. Pei, Q. Su, S. Li, J Lumin, 50 (1991), pp. 123-126.
[155] P. Chau, K. Ryu, C. Yo, J Mater Sci, 33 (1998), pp. 1299-1302.
[156] R. Reisfeld * †, E. Zigansky, M. Gaft, Molecular Physics, 102 (2004), pp. 1319-1330.
[157] J.C.G. Buenzli, D. Plancherel, G.O. Pradervand, The Journal of Physical Chemistry, 93 (1989), pp. 980-984.
[158] K. Goto, Y. Nakachi, K. Ueda, Thin Solid Films, 516 (2008), pp. 5885-5889.
[159] T. Nakamura, M. Shima, M. Yasukawa, K. Ueda, J Sol-Gel Sci Techn, 61 (2012), pp. 362-366.
[160] W. Jia, A. Pérez-Andújar, I. Rivera Journal of The Electrochemical Society, 150 (2003), pp. H161-H164.
[161] Y. Jin, Y. Hu, L. Chen, X. Wang, G. Ju, Opt Mater, 35 (2013), pp. 1378-1384.
[162] X. Yu, X.H. Xu, S.Y. Xin, J.B. Qiu, J Am Ceram Soc, 94 (2011), pp. 985-987.
[163] R. Leonelli, J.L. Brebner, Physical Review B, 33 (1986), pp. 8649-8656.
[164] N. Hosaka, T. Sekiya, S. Kurita, J Lumin, 72–74 (1997), pp. 874-875.
[165] K. Wakabayashi, Y. Yamaguchi, T. Sekiya, S. Kurita, J Lumin, 112 (2005), pp. 50-53.
[166] J. Bohnemann, R. Libanori, M.L. Moreira, E. Longo, Chemical Engineering Journal, 155 (2009), pp. 905-909.
[167] F. Clabau, X. Rocquefelte, T. Le Mercier, P. Deniard, S. Jobic, M.H. Whangbo, Chem Mater, 18 (2006), pp. 3212-3220.
[168] Z. Kotan, M. Ayvacikli, Y. Karabulut, J. Garcia-Guinea, L. Tormo, A. Canimoglu, T. Karali, N. Can, J Alloys Compd, 581 (2013), pp. 101-108.
[169] N. Bonanos, P. Pissis, J.R. Macdonald, Impedance Spectroscopy of Dielectrics and Electronic Conductors, Characterization of Materials, John Wiley & Sons, Inc.2002.
[170] J.E. Bauerle, J Phys Chem Solids, 30 (1969), pp. 2657-2670.
[171] N.J. Kidner, N.H. Perry, T.O. Mason, E.J. Garboczi, J Am Ceram Soc, 91 (2008), pp. 1733-1746.
[172] B. Ostrick, M. Fleischer, U. Lampe, H. Meixner, Sensors and Actuators B: Chemical, 44 (1997), pp. 601-606.

Acknowledgements

I came to the part where I can say thanks to a number of people who contributed to accomplishing the work presented in this thesis.

I would like to express my deepest gratitude to my promoters Prof. Dr. Marlies Van Bael, Prof. Dr. An Hardy and Prof. Habil. Dr. Aivaras Kareiva for their guidance, numerous discussions and support during this long scientific journey.

I am thankful to bilateral agreement between Hasselt University (Belgium) and Vilnius University (Lithuania) for granting me with a possibility to conduct my PhD studies abroad.

I would like to express my thanks to Prof. Dr. Thomas Jüstel for giving me the opportunity to work in his group of tailored optical materials at Münster University of Applied Sciences. I would also like to thank Dr. Artūras Katelnikovas who showed me how to operate with all spectrometers and for his valuable discussion concerning luminescence.

I wish also to acknowledge all members of “Sol-Gel Chemistry Group” from Vilnius University and “Inorganic and Physical Chemistry Group” from Hasselt University, past and present, for their support and friendship over the last years.

Special thanks to the colleagues from Department of Radiophysics of Vilnius University for performing dielectric measurements.

I am grateful for my lovely girlfriend Justyna Zandał for encouraging me to pursue my PhD and always being next to me.

Finally, I want to express my deepest love and thanks to my family for allowing me to realize my own potential and unfailing support they have provided me through this long and complex period.